

AD-A172 481

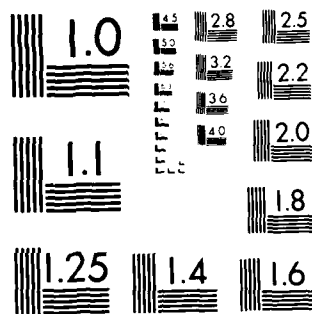
TOPICS IN GEODETIC ALGORITHM RESEARCH(U) ANALYTIC
SCIENCES CORP READING RM R P COMER ET AL. 15 AUG 86
TASC-IR-5186-1 N00014-83-C-0134

1/2

UNCLASSIFIED

F/G 8/3

NL



XEROCOPY RESOLUTION TEST CHART
NATIONAL BUREAU OF STANDARDS-1963-A

AD-A172 481

FILE COPY

TR-5186-1

TOPICS IN GEODETIC ALGORITHM RESEARCH

15 August 1986

DISTRIBUTION STATEMENT A

Approved for public release
Distribution Unlimited

TASC
THE ANALYTIC SCIENCES CORPORATION

86 10 2 201

12

OCT 03 1986

404505
67m

12

TR-5186-1

TOPICS IN GEODETIC ALGORITHM RESEARCH

15 August 1986

DTIC
ELECTE
OCT 03 1986
S D

Prepared for:

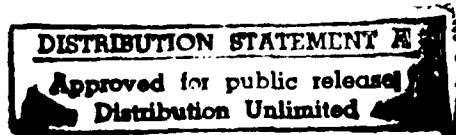
OFFICE OF NAVAL RESEARCH
800 North Quincy Street
Arlington, Virginia 22217

for:

Contract No. N00014-85-C-0134

Prepared by:

Robert P. Comer
A. Richard LeSchack
Karen M. Marks
Kevin S. Tait



Approved by:

Warren G. Heller
Richard V. Sailor

THE ANALYTIC SCIENCES CORPORATION
One Jacob Way
Reading, Massachusetts 01867

UNCLASSIFIED

SECURITY CLASSIFICATION OF THIS PAGE

REPORT DOCUMENTATION PAGE

Form Approved
OMB No. 0704-0188
Exp. Date: Jun 30, 1986

1a. REPORT SECURITY CLASSIFICATION UNCLASSIFIED			1b. RESTRICTIVE MARKINGS None		
2a. SECURITY CLASSIFICATION AUTHORITY			3. DISTRIBUTION/AVAILABILITY OF REPORT Approved for Public Release; Distribution Unlimited		
2b. DECLASSIFICATION/DOWNGRADING SCHEDULE					
4. PERFORMING ORGANIZATION REPORT NUMBER(S) TR-5186-1			5. MONITORING ORGANIZATION REPORT NUMBER(S)		
6a. NAME OF PERFORMING ORGANIZATION The Analytic Sciences Corporation	6b. OFFICE SYMBOL (If applicable)	7a. NAME OF MONITORING ORGANIZATION Office of Naval Research			
6c. ADDRESS (City, State, and ZIP Code) One Jacob Way Reading, MA 01867		7b. ADDRESS (City, State, and ZIP Code) 800 North Quincy Street Arlington, VA 22217			
8a. NAME OF FUNDING/SPONSORING ORGANIZATION Office of Naval Research	8b. OFFICE SYMBOL (If applicable)	9. PROCUREMENT INSTRUMENT IDENTIFICATION NUMBER N00014-85-C-0134			
8c. ADDRESS (City, State, and ZIP Code) 800 North Quincy Street Arlington, VA 22217		10. SOURCE OF FUNDING NUMBERS			
		PROGRAM ELEMENT NO.	PROJECT NO.	TASK NO.	WORK UNIT ACCESSION NO.
11. TITLE (Include Security Classification) Topics In Geodetic Algorithm Research					
12. PERSONAL AUTHOR(S) Comer, R.P., LeSchack, A.R., Marks, K.M., Tait, K.S.					
13a. TYPE OF REPORT Final	13b. TIME COVERED FROM 1/85 TO 12/85	14. DATE OF REPORT (Year, Month, Day) 1986 April 30		15. PAGE COUNT	
16. SUPPLEMENTARY NOTATION					
17. COSATI CODES			18. SUBJECT TERMS (Continue on reverse if necessary and identify by block number)		
FIELD	GROUP	SUB-GROUP			
			Geodesy, gravity anomaly, deflection of the vertical, geodetic algorithm, collocation, terrain reduction, GEOFAST.		
19. ABSTRACT (Continue on reverse if necessary and identify by block number)					
<p>The concept of <u>geodetic algorithm</u> is defined in the context of estimating and computing gravity field quantities of interest from available measured data. Examples of major categories of geodetic algorithms are given. These include classical integral evaluation methods, least-squares collocation, TASC's GEOFAST technique, and Fourier transform methods. Also summarized and reviewed are algorithms and techniques considered in investigations by an International Association of Geodesy (IAG) Special Study Group.</p> <p>Detailed results are presented for numerical experiments with the GEOFAST algorithm applied to synthetic data, demonstrating the high accuracy and computational efficiency of this method. Various aspects of the treatment of terrain effects are considered, including relevant efforts and results of the IAG Special Study Group as well as new theoretical and experimental contributions by TASC.</p>					
20. DISTRIBUTION/AVAILABILITY OF ABSTRACT <input checked="" type="checkbox"/> UNCLASSIFIED/UNLIMITED <input type="checkbox"/> SAME AS RPT. <input type="checkbox"/> DTIC USERS			21. ABSTRACT SECURITY CLASSIFICATION UNCLASSIFIED		
22a. NAME OF RESPONSIBLE INDIVIDUAL Mr. John G. Heacock			22b. TELEPHONE (Include Area Code) (202) 696-4122	22c. OFFICE SYMBOL	

TABLE OF CONTENTS

	<u>Page</u>
List of Figures	v
List of Tables	vii
1. INTRODUCTION	1-1
2. OVERVIEW OF GEODETIC ALGORITHMS	2-1
2.1 Geodetic Algorithms	2-1
2.2 Introduction to Specific Algorithms	2-7
3. SUMMARY AND REVIEW OF IAG STUDY GROUP METHODS	3-1
3.1 White Sands Data	3-1
3.2 Gravity Anomaly Prediction	3-3
3.3 Prediction of Deflection of the Vertical	3-4
4. OVERVIEW OF TERRAIN EFFECTS STUDIES BASED ON WHITE SANDS DATA	4-1
4.1 Overview	4-1
4.2 Data Used in these Investigations	4-3
4.3 Spectral Analysis of Gravity Data and Topographic Effect	4-3
4.4 Predicting Deflections of the Vertical from Local Topography	4-8
4.5 Summary of Results and Conclusions	4-9
5. NEW DERIVATION OF THE FFT TERRAIN CORRECTION ALGORITHM	5-1
6. NUMERICAL EXPERIMENTS WITH GEOFAST ALGORITHM	6-1
6.1 Summary of Approach	6-1
6.2 Synthetic Marine Gravity Data Set	6-3
6.3 Results with Synthetic Marine Data	6-5
6.3.1 Description of Test Cases	6-5
6.3.2 Results for Noise-Free Estimation	6-7
6.3.3 Effect of Noisy Observations on Estimation Results	6-11
6.4 Synthetic Local Gravity Data Set	6-13
6.5 Results with Synthetic Local Data	6-14
6.6 Summary of Results	6-18
7. SUMMARY AND CONCLUSIONS	7-1
7.1 Summary of Key Contributions	7-2
7.2 Conclusions	7-3
7.3 Recommendations and Suggestions for Further Work	7-4

THE ANALYTIC SCIENCES CORPORATION

TABLE OF CONTENTS (Continued)

	<u>Page</u>
APPENDIX A GEODETIC ALGORITHMS	A-1
APPENDIX B FFT TERRAIN CORRECTION ALGORITHM: DETAILS OF NEW DERIVATION	B-1
APPENDIX C ANALYSIS OF TERRAIN EFFECTS USING WHITE SANDS DATA	C-1
REFERENCES	R-1



Accession For	
NTIS CRA&I	<input checked="checked" type="checkbox"/>
DTIC TAB	<input type="checkbox"/>
Unannounced	<input type="checkbox"/>
Justification	
By	
Distribution /	
Availability Codes	
Dist	Avail and/or Special
A-1	

LIST OF FIGURES

<u>Figure</u>		<u>Page</u>
1-1	Operation of Geodetic Algorithms	1-3
1-2	Research on Geodetic Algorithms	1-4
2.1-1	Relationships Among Geodetic Quantities	2-4
4.1-1	Overview of Terrain Effects Analyses	4-2
4.3-1	Profile EW-3	4-6
4.3-2	East-West Mountainous Terrain	4-7
4.4-1	Observed and Predicted Deflections of the Vertical	4-10
4.4-2	Scatter Diagram of East Vertical Deflection Component	4-11
5-1	Terrain Correction	5-2
5-2	White Sands Terrain Example	5-4
6.1-1	GEOFAST Computer Time for N = 1024	6-2
6.2-1	Synthetic Marine Gravity Anomalies (Rapp Model to Degree 180 Contoured at 20 mgal)	6-3
6.2-2	High-Frequency Synthetic Marine Gravity Anomalies (Rapp Model Degrees 91-180 Contoured at 20 mgal)	6-4
6.3-1	Synthetic Gravity Anomaly Data (Rapp Model Degrees 91-180 at 0.5 deg Spacing)	6-5
6.3-2	Synthetic East Deflection Data (Rapp Model Degrees 91-180 at 0.5 deg Spacing)	6-6
6.3-3	Synthetic East Deflection Data (Rapp Model Degrees 91-180 at 0.25 deg Spacing)	6-6
6.3-4	East Deflection Estimation Error (GEOFAST Algorithm with Gridding at 0.5 deg and 0.25 deg and Bandwidths of 0 and 4)	6-9
6-4.1	Along-Track Vertical Disturbance Spectra	6-14

LIST OF FIGURES (Continued)

<u>Figure</u>		<u>Page</u>
6.4-2	East Gravity Disturbance Surface Plot	6-15
6.4-3	East Gravity Disturbance Contour Plot (mgal)	6-15
6.5-1	East Gravity Disturbance Estimation Error (mgal)	6-17

LIST OF TABLES

<u>Table</u>		<u>Page</u>
3.1-1	White Sands Data Sets	3-2
3.2-1	Methods for Computing Gravity Anomaly	3-3
3.3-1	Methods for Computing Deflection of the Vertical	3-4
3.3-2	Summary of Methods (1985 Report Only)	3-6
3.3-3	Statistics for Comparisons	3-9
6.3-1	GEOFAST Estimation Accuracy	6-8
6.3-2	Effect of High-Order Reference Field	6-11
6.3-3	Effect of Measurement Error	6-12
6.4-1	AWN Statistical Gravity Model	6-13
6.5-1	GEOFAST Estimation Accuracy	6-16

1.

INTRODUCTION

The U.S. Navy needs accurate gravity field data for navigation and missile guidance applications. The scientific community also uses marine gravity data in studies of lithospheric structure and global tectonics. Most of the necessary gravity field information cannot be measured directly and must be derived computationally from large volumes of existing measurement data. Such data may come from diverse sources -- for example, satellite altimeter measurements as well as conventional ship survey gravity data.

Existing data bases of measured gravity field data are expected to expand considerably in the next few years as, for example, data from the gravity gradiometer survey system become available. Large quantities of data continue to be received from the GEOSAT radar altimeter mission. Emphasis must be placed now on the development and evaluation of computational techniques to estimate geodetic quantities of interest to the Navy and the scientific community. These techniques will have to exploit, in an accurate and computationally efficient manner, an ever expanding data base including many types of measurements, each with its own noise and spatial distribution characteristics. The necessary computational techniques must also provide realistic accuracy estimates for the gravity quantities being determined.

The International Association of Geodesy (IAG) has recently established a Special Study Group to investigate algorithms for local gravity field determination. This group has been examining the accuracy and computational efficiency of a number of geodetic algorithms, using a standard set of gravity

field data. Algorithms are being examined and evaluated for efficiency, stability, accuracy, and applicability, as well as their limitations. Study group participants have conducted numerical tests of the computation of gravity anomalies, deflections of the vertical, geoid undulations, and gravity gradients. The group has also considered issues of error estimation and incorporation of topographic, geophysical, and geological information into the estimation. TASC has participated in the work of this group, primarily in the area of applying the GEOFAST algorithm as a tool for the efficient determination of gravity field quantities.

The concept of geodetic algorithm, illustrated in Fig. 1-1, is central to the work described in this report. This term includes methods for estimating and computing gravity field quantities of interest on the basis of available measured data. The gravity field quantities of interest (geoid undulation, gravity anomaly, deflection of the vertical, gravity gradients, etc) may not be directly measurable or not measurable conveniently and economically. This definition of geodetic algorithm is presented in more detail in Section 2.1 of the report; an introduction to the major categories of geodetic algorithms is given in Section 2.2. Appendix A is a detailed review of these algorithms.

The objective of this report is to present the results of a study to determine the most appropriate techniques and algorithms for estimating geodetic quantities from a variety of observation types. The investigations reported here have included both theoretical and computational studies. Figure 1-2 summarizes these investigations.

This report includes seven chapters. Chapter 2 is devoted to an examination of geodetic algorithms. In addition to an overview of the concept of a geodetic algorithm, the

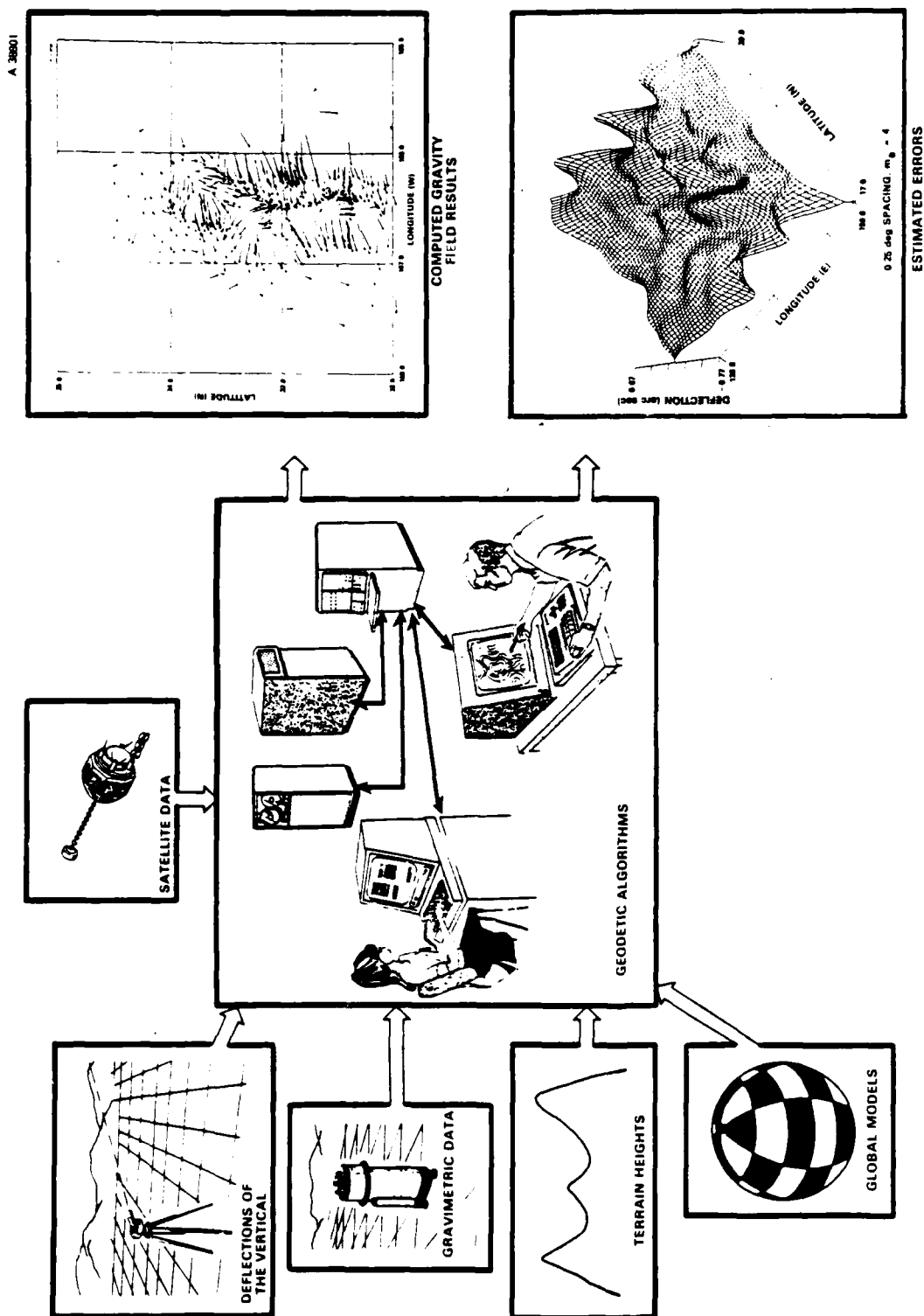


Figure 1-1 Operation of Geodetic Algorithms

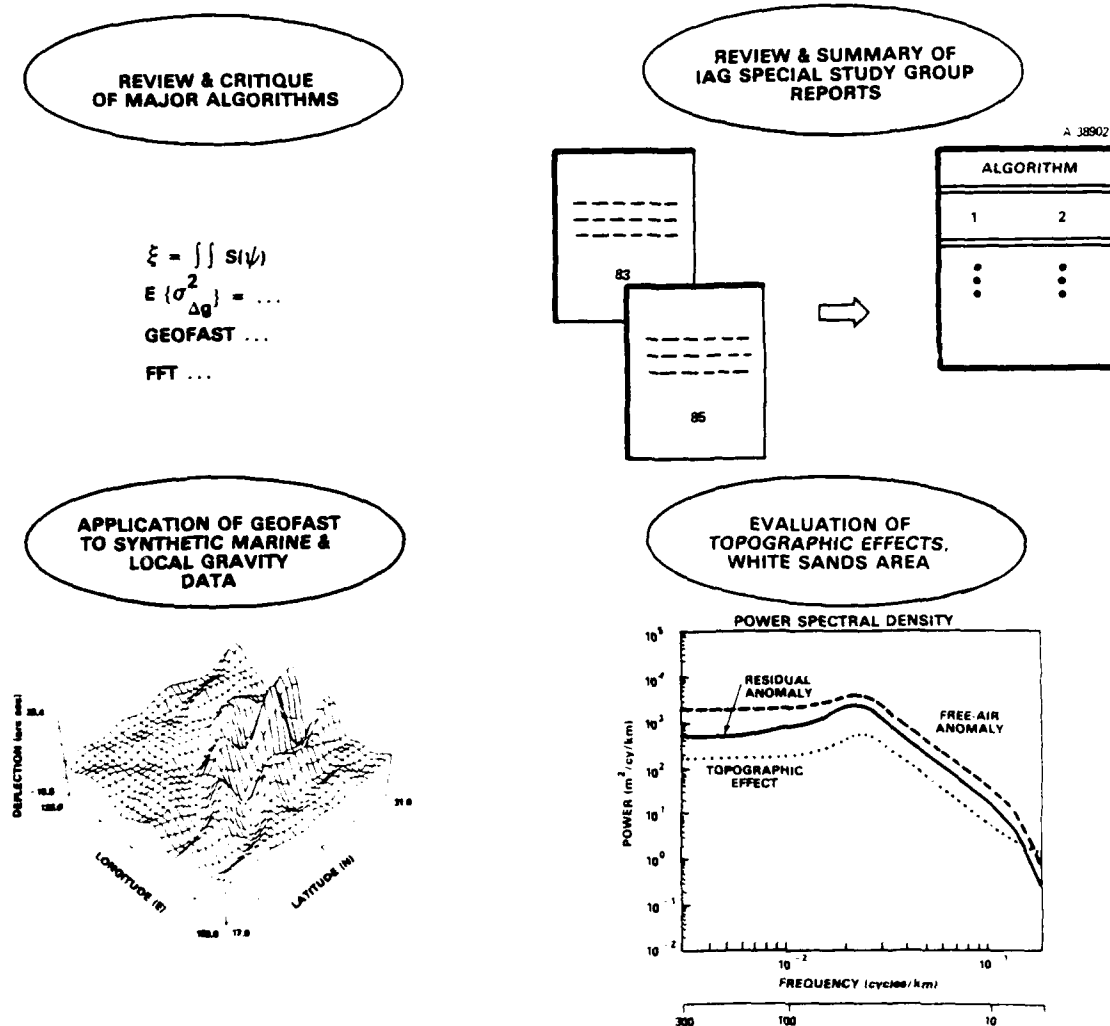


Figure 1-2 Research on Geodetic Algorithms

chapter introduces the classical integral evaluation methods, as well as least-squares collocation, GEOFAST, and Fourier transform methods. Details of all of these techniques are reviewed in Appendix A.

Chapter 3 presents a summary of the methods considered in the IAG Study Group investigations. Comparative features

of various algorithms and techniques are presented in text and tabular form. This chapter summarizes the key results on the relative accuracy and efficiency of the methods considered by the IAG Study Group.

Chapter 4 summarizes various aspects of the treatment of topographic or terrain effects, especially important in regions of high relief such as the White Sands study area. In addition to reviewing the relevant efforts and results of the IAG Study Group, Chapter 4 includes an overview of original investigations conducted by TASC, with a more detailed discussion in Appendix C.

Chapter 5 describes the essentials of a new derivation, developed by TASC, of a Fast Fourier Transform (FFT) algorithm for implementing terrain correction. The detailed derivation of this approach is documented in Appendix B.

In Chapter 6, results are presented for a series of numerical experiments involving applications of the GEOFAST algorithm. The two major phases of this study involved computations using:

- Synthetic marine gravity data derived from the high-degree-and-order part of a global geopotential model
- A set of synthetic high-frequency local gravity data constructed on the basis of the statistical characteristics of local gravity truth data.

The principal conclusion of this study is that modern geodetic algorithms can, with appropriate data input, resolve deflections of the vertical to 0.2 arc sec for the marine data and to 0.5 arc sec for the local gravity data.

Chapter 7 presents TASC's conclusions and recommendations resulting from the study effort.

In addition to the summaries, discussions, and evaluations of the work of the IAG Study Group, and the presentation of appropriate supporting material from other relevant published scientific literature, this report documents several original contributions by TASC to the geodetic algorithm study effort. These contributions include:

- Analysis of GEOFAST algorithm performance (Chapter 6)
- New and improved derivations of FFT terrain correction algorithms (Chapter 5 and Appendix B)
- Studies of the prediction of local deflections of the vertical from terrain height data alone (Chapter 4 and Appendix C).

2. OVERVIEW OF GEODETIC ALGORITHMS

This chapter introduces the concept of geodetic algorithm and includes technical discussions of several main categories of such algorithms. Section 2.1 defines geodetic algorithms and suggests a variety of classifications based on criteria which include type and distribution of available measurement data, quantities to be computed, and the statistical or deterministic orientation of the computational approach. Section 2.2 introduces a number of specific algorithms which are presented in more detail in Appendix A. These include classical integral evaluation methods, least-squares collocation, TASC's GEOFAST algorithm, and other Fourier transform and frequency domain approaches.

2.1 GEODETIC ALGORITHMS

The term geodetic algorithm is used extensively throughout this report to refer to methods of computing geodetic quantities of interest from available measured data. These algorithms can be classified and categorized in a number of ways:

- The specific geodetic quantity to be computed or estimated
- The general approach (deterministic or statistical)
- The type or types of measurement data to be used

- The geographical distribution of the points at which the quantities are to be computed -- for example, a small number of irregularly spaced points as opposed to a large number of points forming a regular grid
- The distribution of the points at which data measurements are assumed to be available.

In addition, algorithms can be distinguished on the basis of specific techniques used for the numerical evaluation (exact or approximate) of the underlying theoretical formulations.

A brief discussion of the various bases of classification follows. It is intended to be an introduction to the large variety of specific algorithms that are treated in the rest of this report.

Geodetic quantity to be computed - Historically, the earliest examples of geodetic algorithms were developed to compute the undulation of the geoid or the components of the deflection of the vertical at a specified location. In the first case, the undulation is a geodetic quantity that cannot be measured directly, even if the specified location is easily accessible. In the second case, while the deflection of the vertical can be measured directly at an accessible point using astrogeodetic techniques, there are substantial economic and logistical considerations that may make indirect determination more attractive. Also, many locations are inaccessible in a practical sense to the equipment required for direct astrometric measurement of the deflection.

Other geodetic data types which have become important through more recent applications include:

- Components of the gravity disturbance vector at altitude
- Components of the gravity gradient tensor
- Mean values of the gravity anomaly, typically for regions within which direct gravity measurements are scarce or unavailable.

There is a general unifying concept that facilitates the consideration of the numerous geodetic quantities that may be the subject of computation or estimation algorithms. This point of view regards the disturbing potential as the fundamental geodetic quantity to be determined from whatever combination of observational data may be available; other geodetic quantities are computed, in principle, by applying linear operators of various kinds to the disturbing potential (Fig. 2.1-1). Thus, for example, Bruns's formula:

$$N = T/\gamma \quad (2.1-1)$$

where

N is the undulation of the geoid

γ is the normal gravity

T is the disturbing potential

is the simplest example of this concept. Similarly, the gravity disturbance vector is expressed as:

$$\underline{\delta} = \text{grad } T \quad (2.1-2)$$

the scalar gravity disturbance as:

$$\delta g = - \frac{\partial T}{\partial n} \quad (2.1-3)$$

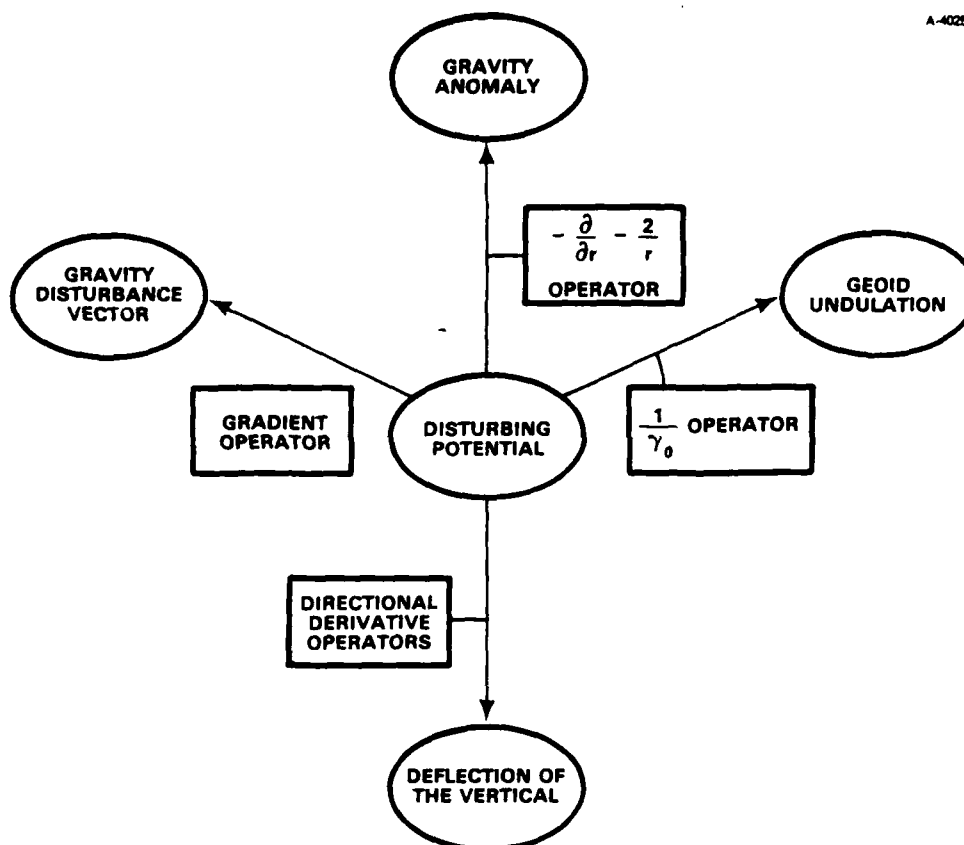


Figure 2.1-1 Relationships Among Geodetic Quantities

where the partial derivative is taken along the normal to the geoid (plumb line); and the gravity anomaly as (exact form):

$$\Delta g = - \frac{\partial T}{\partial n} + \frac{1}{\gamma} \frac{\partial \gamma}{\partial n} T \quad (2.1-4)$$

or, in the usual spherical approximation:

$$\Delta g = - \frac{\partial T}{\partial r} - \frac{2}{R} T \quad (2.1-5)$$

where the partial derivative is taken in the radial direction, and R is a mean radius of the earth. This concept is treated in more detail in Appendix A.2.3, where such operators, illustrated in Fig. 2.1-1, are summarized in Table A.2-1.

Deterministic and statistical approaches - Classical geodetic algorithms assume that the measured quantity is known without error everywhere on the globe. For example, the Stokes integral for determining undulation or the Vening Meinesz integral for deflections of the vertical both require, in theory, error-free knowledge of the gravity anomaly everywhere. Actual evaluations of these algorithms involve finite approximations to infinite processes like integration, as well as estimation (interpolation or extrapolation) of unmeasured gravity anomaly data in terms of available measurements.

Modern statistical approaches to the formulation of geodetic algorithms attempt to deal directly with issues involving:

- The discrete and finite nature of the measured data
- The statistical nature of measurement error in the data
- The formulation of best methods based on global statistical properties of measured data
- The development of methods using a combination of data types in an optimal manner.

Collocation methods, discussed in Appendix A.2, are an example of statistically oriented geodetic algorithms.

Measurement data types - Classical geodetic algorithms are based on the use of point gravity anomaly data, since this is the type of geodetic measurement that can most readily be made directly and reasonably economically. Modern algorithm development is marked by the availability of a wide variety of other data types, such as:

- Geopotential field coefficients recovered from satellite orbit studies
- Satellite altimeter estimates of undulation over the oceans
- Astronomic measurements of deflection of the vertical
- Mean gravity anomaly data of specified block size
- Direct measurements of components of the gravity gradient tensor
- Gravity field quantities recovered from other high-accuracy position-determination technologies, such as inertial and GPS.

Algorithm development is also influenced by the desirability of using mixed data types as input for the determination of other geodetic quantities of interest.

Distribution of computation points - Classical algorithms were designed to produce results for a single point at a time, with the bulk of the computations having to be redone entirely to obtain a result for another point, even if it is nearby. (However, some exceptions, such as the method of astrogravimetric interpolation, can be noted.) A characteristic of many modern algorithms is the ability to produce results essentially simultaneously for a number of points, which may be distributed irregularly or located on a uniform rectangular grid.

Distribution of data points - Classical algorithms assume, at least in principle, the availability of data everywhere on the surface of the earth. Modern algorithms relax this unrealistic assumption in various ways. Collocation methods (see Appendix A.2), for example, are based on the optimal use of a finite number of irregularly distributed observations of various kinds, corresponding closely and without idealization to the realities of data measurements in the field. The GEOFAST algorithm (see Appendix A.3), on the other hand, operates on a regular rectangular grid of data points and outputs values on a regular grid.

2.2 INTRODUCTION TO SPECIFIC ALGORITHMS

The algorithms documented in detail in Appendix A include classical integral evaluation methods, least-squares collocation, TASC's GEOFAST algorithm, and other Fourier transform and frequency domain approaches. A brief overview and discussion of each of these methods is given in the present section.

Integral evaluation methods - The classical integral evaluation methods of Stokes and Vening Meinesz determine the undulation of the geoid and the deflection of the vertical at a specific point from global free-air gravity anomaly data. More recent modifications of these methods, due to Molodenskii and Pellinen, make explicit use of terrain height data and refer to the physical surface of the earth rather than to the geoid. Both the classical methods and more recent developments are discussed in Appendix A.1.

The classical methods may eventually be supplanted by modern approaches based on the use of gravity disturbances

rather than gravity anomalies, associated with precise local positioning techniques such as the use of the Global Positioning System (GPS). In addition, the computational approach of numerical evaluation of integrals taken over the earth's surface may largely give way in practice to the collocation and frequency-domain techniques outlined below. Nonetheless, the classical integral evaluation methods are important for at least three reasons:

- They are the theoretical basis for more recent developments
- They are still widely used in practice in a number of areas (e.g., Ref. 6; see also Ref. 49)
- They were considered to be competitive in the White Sands Study (Ref. 21).

Least-squares collocation - This modern technique for estimating geodetic quantities from observed data is discussed in Appendix A.2. Among the advantages it offers, as compared with classical integral evaluation methods, are the following:

- The use of a variety of measured data types as input, and the simultaneous estimation of several gravity field quantities
- The use of irregularly spaced observation points
- The incorporation of statistical information about errors in the input data, with corresponding results for the quality of the estimated geodetic quantities
- The estimation or improvement of model parameters along with the determination of the geodetic quantities to be estimated.

An important characteristic of the collocation approach is that least-squares estimation is applied to data from which systematic and long-wavelength components have been removed. These residual data and the quantities estimated from them correspond, therefore, to a more nearly stationary and isotropic residual gravity field. As a final step, the appropriate systematic and long-wavelength components are restored.

The GEOFAST algorithm - TASC's GEOFAST algorithm (Ref. 16) was developed as a computationally efficient method for solving the minimum-variance estimation equations that arise from the application of least-squares collocation to the determination of geodetic quantities. It replaces the direct matrix solution of the estimation equations, a process whose computational cost is of the order of N^3 (where N represents the number of data points), by a sequence of operations for which the overall computational effort is of order $N \log_2 N$. The GEOFAST algorithm is described in Appendix A.3; Chapter 6 of this report presents the results of two sets of numerical experiments -- one using marine gravity data in an ocean trench area, the other using land gravity data in the White Sands area.

Other Fourier Transform Methods - Methods based on a two-dimensional Fourier transform lead to efficient computational algorithms that estimate geodetic quantities in a variety of ways. Examples include the evaluation of the Stokes integral for undulation of the geoid, the Vening Meinesz integral for deflection of the vertical, the Poisson integral for upward continuation, and the convolution integrals defining terrain corrections. Appendix A.4 presents the theory of Fourier transform methods and describes specific applications to convolutions and to the evaluation of Stokes and Vening Meinesz integrals.

3.

SUMMARY AND REVIEW OF IAG
STUDY GROUP METHODS

This chapter concerns two reports on the application of geodetic algorithms in mountainous terrain. The first (Ref. 20; also to be referred to as the "1983 Report") was produced by members of the IAG Special Study Group 4.70 on "Gravity Field Approximation Techniques." Several sets of investigators contributed descriptions of the application of a variety of algorithms. Two main tasks were undertaken: the prediction of gravity anomalies and the prediction of deflections of the vertical from gravimetry and gridded topographic heights in the White Sands, NM area. The second report (Ref. 21; "1985 Report") was written jointly by a group of five investigators gathered at the University of Calgary and concentrates solely on the prediction of deflections of the vertical. Four techniques are described and compared in detail.

The chapter is organized into three sections. Section 3.1 describes briefly the White Sands data sets; illustrations and more complete descriptions are included in Chapter 4 and Appendix C, which describe TASC's further analysis of these data. The gravity anomaly prediction algorithms from the 1983 Report are summarized in Section 3.2. The prediction of deflections of the vertical is described in Section 3.3; it incorporates material from both reports.

3.1 WHITE SANDS DATA

The IAG study group used four main sets of data from the White Sands area. A brief description of each, along with

its geographic location and number of data values, is given in Table 3.1-1. The gravity anomaly data are divided into two groups to facilitate the evaluation of algorithms for predicting gravity anomalies; the second set contains truth data. The locations of the points in data sets 1 and 2 that fall within the 3 deg by 3 deg region between 32 and 35 deg North and 105 and 108 deg West are shown in Fig. C.2-1. Their values were gridded to form the color image in Fig. C.2-2. The gridded heights (data set 3) are illustrated as a color image in Fig. C.2-3, for the region between 32 and 35 deg North and 105 and 108 deg West. The vector plot of Fig. C.5-1 shows the locations and values of the astrogeodetic deflections of data set 4. Note that in the plots of these data shown in Fig. 4 (p. 7) of the 1983 Report and Fig. 1.6 (p. 11) of the 1985 Report the sign of the east deflection η is reversed from the usual convention (e.g., Ref. 1).

TABLE 3.1-1
WHITE SANDS DATA SETS

NO.	TYPE	LOCATION	NUMBER OF DATA
1	Point free-air gravity anomaly (with height and location)	31-36.4 deg N 104-109.4 deg W	11,277
2	Point free-air gravity anomaly (with height and location)	33-34 deg N 106-107 deg W	102
3	Point heights on a regular grid, 30 arc sec spacing	31-35 deg N 105-108 deg W	172,320
4	Pairs of astrogeodetic deflections of the vertical	mainly 32-34 deg N 106-107 deg W	441

3.2 GRAVITY ANOMALY PREDICTION

The study group's strategy to evaluate algorithms for predicting gravity anomalies was to use data set 1 (free-air gravity) supplemented by data set 3 (topographic heights) to predict values of additional measured gravity anomalies in data set 2. The 1983 Report describes the work of three sets of investigators, each of whom used some variation of least-squares collocation. Their methods and results are summarized briefly in Table 3.2-1, which is adapted from Table 2, p. 92 of the 1983 Report. The standard deviations in the table refer to the difference between the predicted anomalies and the actual

TABLE 3.2-1
METHODS FOR COMPUTING GRAVITY ANOMALY

METHOD	AUTHORS	STANDARD DEVIATION (mgal)
<u>Least-squares collocation using</u>		
Free-air anomalies	Merry	17.8
	Schwarz, Lachapelle, & Mainville	17.5
	Tscherning & Forsberg	17.9
Incomplete Bouguer anomalies	Merry	7.4
	Schwarz, Lachapelle, & Mainville	7.9
Incomplete Bouguer anomalies plus trend surface	Merry	6.6
Refined Bouguer anomalies	Tscherning & Forsberg	6.5
<u>Trend surface for incomplete Bouguer anomalies</u>	Merry	13.9

values in data set 2. These results show that least-squares collocation (interpolation) using only free-air anomalies is less accurate than interpolation based on Bouguer anomalies.

3.3 PREDICTION OF DEFLECTION OF THE VERTICAL

The IAG study group evaluated algorithms for the prediction of deflection of the vertical by making predictions based on free-air gravity in data sets 1 and 2, supplemented by the gridded topographic heights of data set 3. The results were compared to the astrogeodetic deflections of data set 4.

Table 3.3-1 lists six algorithms. The first four are described in the 1983 Report and summarized in Ref. 46. The last four are described and systematically compared in the 1985 Report. The middle two overlap; they are mentioned in both reports.

TABLE 3.3-1
METHODS FOR COMPUTING DEFLECTION OF THE VERTICAL

METHOD	AUTHORS
Topographic/Isostatic Reduction	Schwarz, Lachapelle, & Mainville (1983 Report)
Local Collocation	Hein & Landau (1983 Report)
Combined Collocation & Integration	Schwarz, Lachapelle, & Mainville (1983 Report); Krynski (1985 Report)
Terrain Effect Integration & Collocation	Tscherning & Forsberg (1983, 1985 Reports)
Rice Rings Integration	Kearsley (1985 Report)
Fast Fourier Transform	Sideris (1985 Report)

The first method, Topographic/Isostatic Reduction, is the only one in which the gravity data are not used. It uses only topography and the low-degree geopotential model GEM10B (Ref. 36). An Airy-Heiskanen model of isostatic compensation with a crustal thickness of 30 km is applied and the effects of the topography, isostatic reduction potential, and GEM10B are combined to predict deflection of the vertical. The difference between the result and the astrogeodetic truth data has a standard deviation ranging from 2 to 2.5 arc sec (depending on which component and geographical area is considered).

The next method, Hein and Landau's pointwise Local Collocation, is applied directly to the free-air gravity anomaly data. Values within a radius of 35 km of the prediction point are used, along with Reilly's covariance model (e.g., Section 2.3.3) fitted to the data. The standard deviations relative to the truth data are slightly less than 2 arc sec.

The last four methods, compared in detail in the 1985 Report, are summarized in Table 3.3-2, which includes a brief discussion of each method and an indication of whether deflection values are computed separately for each point or are computed simultaneously (i.e., from the same subset of the gravity data) for more than one point. In addition, the format and spatial extent of the input gravity data and the treatment of local topographic effects and global effects (from long-wavelength geopotential models) are indicated.

Combined Collocation and Integration is a pointwise method which uses (mean) gravity anomalies within a 3 deg radius of the computation point. Least-squares collocation would be inefficient over so large an area (too much data), so it is applied only to data within an inner zone of 0.65 deg radius, after removal of the long-wavelength contribution from GEM10B.

TABLE 3.3-2
SUMMARY OF METHODS (1985 REPORT ONLY)

METHOD	COMBINED COLLOCATION & INTEGRATION	TERRAIN EFFECT INTEGRATION & COLLOCATION	RICE RINGS INTEGRATION	FAST FOURIER TRANSFORM
SUMMARY:				
POINTWISE/SIMULTANEOUS COMPUTATION	Least-squares collocation applied in inner zone; Venign Meinesz integral applied to residual in outer zone	RTH remove/restore and least-squares collocation	Vening Meinesz integral via a computer adaptation of Rice's system	Flat-earth Vening Meinesz integral evaluated in transform domain
GRAVITY DATA: EXTENT	Pointwise Inner zone radius = 0.65 deg Outer zone radius = 3 deg	Simultaneous two 1.4 by 1.4 deg blocks	Pointwise up to radius = 1.2 deg	Simultaneous 6 by 6 deg block
POINT/MEAN	5 arc min means in inner zone; 15 arc min and 1 deg means in outer zone	1 point selected per 3 by 3 arc min block	Windowed point gravity data	5 arc min means
TOPOGRAPHIC EFFECTS: MODEL/COMPUTATION	Approximate RTH/Prism integration	RTH/Prism integration	--	Complete Bouguer/FFT
REMOVED FROM GRAVITY DATA	No	Yes	No	Yes
ADDED TO DEFLECTIONS	Yes	Yes	No (Height data used only to compute free-air anomaly after interpolation of incomplete Bouguer anomaly)	Yes
GLOBAL EFFECTS: MODEL	GEM10B	OSU79	GEM10B	GEM10B
REMOVED FROM GRAVITY DATA	Yes	Yes	No	Yes
ADDED TO DEFLECTIONS	Yes	Yes	Yes	Yes

The Tscherning and Rapp covariance model (Ref. 23; Section 2.3.3), with appropriate parameters, is used in the collocation. Then, in the outer annulus, the Vening Meinesz integral is applied to the difference between the free-air anomaly data and the values extrapolated from the inner zone by collocation. The resulting correction is applied to the deflection of the vertical predicted by collocation, and the effect of GEM10B is restored. Finally, an additional correction is applied from an approximate Residual Terrain Model (see Ref. 34 and the following paragraph).

Terrain Effect Integration and Collocation is also based on least-squares collocation, but it is applied over a larger area, and deflections of the vertical within a 1 by 1 deg block are computed simultaneously (i.e., from the same set of gravity anomalies) rather than pointwise. This would require excessive computation if applied to the raw data; however, prior to collocation, the effect of a Residual Terrain Model (RTM) is removed from the free-air anomaly. That is, the effect of topography relative to a smooth reference surface is subtracted, resulting in a smooth residual field. Also removed is the effect of OSU79 (Ref. 37), a detailed global geopotential model extending to spherical harmonic degree and order 180. Because the residual field is smooth, only one data value from each 3 by 3 arc min block is used and collocation becomes practical. The covariance function used in the collocation is based on the Tscherning and Rapp covariance model, with parameters suitable to the residual field. After collocation, the RTM and OSU79 effects are restored to the predicted deflections.

In Rice Rings Integration the Vening Meinesz integral is evaluated by means of a computer adaptation of Rice's (Ref. 5) system of concentric rings divided into compartments (see Appendix A.1). The deflection of the vertical at the center point

of the template of rings is computed directly from the free-air anomaly at the center of each compartment. In turn, the free-air anomaly at the center of a compartment is estimated by computing the incomplete Bouguer anomaly at nearby points, applying linear interpolation, then using the height at the central point of the compartment to convert back from Bouguer to free-air anomaly. (This is the only way in which the gridded height data are utilized.) Finally, the deflection predicted from GEM10B is added to account for remote zone effects.

The Fast Fourier Transform method is an application of the FFT approach to the Vening Meinesz integral, as described in Appendix A.4. This method requires gridded data; 5 by 5 arc min means within a 6 by 6 deg block are used. The large block (the deflections are required only within a 1 by 2 deg area) minimizes edge effects. The complete Bouguer correction (computed via the FFT terrain correction algorithm described in Appendix B) and the effects of GEM10B are removed from the input free-air anomalies and restored to the predicted deflections. The FFT method results in the simultaneous computation of deflections on a regular grid, which must be interpolated to the points of interest.

The relative performance of these four methods is indicated by Table 3.3-3 (abstracted from Table 4.5, p. 92, 1985 Report). The statistics in the second column from the left indicate the magnitude and mean of the truth data (ξ and η), while the last four columns show statistics for errors ($\Delta\xi$ and $\Delta\eta$) in the prediction of each algorithm. The statistics include all results from the one by two degree area between 32 and 34 deg North and 106 and 107 deg West. Except for 1.4 arc sec in the case of $\Delta\eta$, Rice's Rings Integration, the mean errors are less than 1 arc sec in absolute value, indicating that there is little systematic bias. The standard deviations of

TABLE 3.3-3
STATISTICS FOR COMPARISONS

STATISTICS (arc sec)	OBSERVED (Astrogeodetic)		OBSERVED MINUS PREDICTED							
			COMBINED COLLOCATION & INTEGRATION		TERRAIN EFFECT INTEGRATION & COLLOCATION		RICE RINGS INTEGRATION		FAST FOURIER TRANSFORM	
	ξ	η	$\Delta\xi$	$\Delta\eta$	$\Delta\xi$	$\Delta\eta$	$\Delta\xi$	$\Delta\eta$	$\Delta\xi$	$\Delta\eta$
MEAN	-2.4	-4.3	-0.1	0.8	-0.2	0.6	-0.1	1.4	-0.1	0.7
STANDARD DEVIATION	2.7	6.2	0.9	1.2	0.9	1.0	0.9	1.1	1.0	1.0
RMS	3.6	7.5	0.9	1.4	0.9	1.1	0.9	1.8	1.0	1.2

the errors, including both deflection components and all four methods, are essentially equal, at about 1 arc sec. Quite possibly, this represents a natural limit, imposed by the spacing and quality of the data, which has been reached by all four algorithms.

This section concludes with a comment on relative efficiency and required computer time. While the authors of the 1985 Report attempted a quantitative comparison, the result is not straightforward. This is because the data preprocessing requirements differ among the algorithms, and the relative efficiency varies with the number of computation points. The methods which involve simultaneous computations (Terrain Effect Integration And Collocation; Fast Fourier Transform) incur comparatively less computational cost for generating additional results than the other approaches. Also, the terrain correction computations are time consuming and tend to dilute other differences. However, in general, the Fast Fourier Transform method tends to be fastest in terms of computation time per estimated deflection point and the other three algorithms are roughly comparable to one another in speed.

4. OVERVIEW OF TERRAIN EFFECTS STUDIES
BASED ON WHITE SANDS DATA

This chapter summarizes TASC's investigation of the significance of terrain effects in the computation of gravity disturbance and deflections of the vertical, complementing the work of the IAG Study Group (Refs. 20, 21). A more detailed description of this study is found in Appendix C.

4.1 OVERVIEW

Terrain effects need to be included in computations that predict various gravity field quantities from observed gravity anomaly data, particularly in regions of rugged terrain like the White Sands study area. TASC's investigation of the quantitative significance of these effects is outlined in Fig. 4.1-1, where reference is made to the sections of Appendix C in which detailed technical discussions are found, and to the figures in this appendix which present specific results.

Our investigation includes two distinct studies. One of these, shown in the upper half of Fig. 4.1-1, makes use of spectral techniques to examine and compare observed free-air gravity anomalies and computed topographic effects for two types of terrain -- mountain and plateau -- and for two profile orientations -- east-west and north-south. The methodology and conclusions of this study are summarized below (Section 4.3) and presented in detail in Sections C.2, C.3, and C.4 of Appendix C.

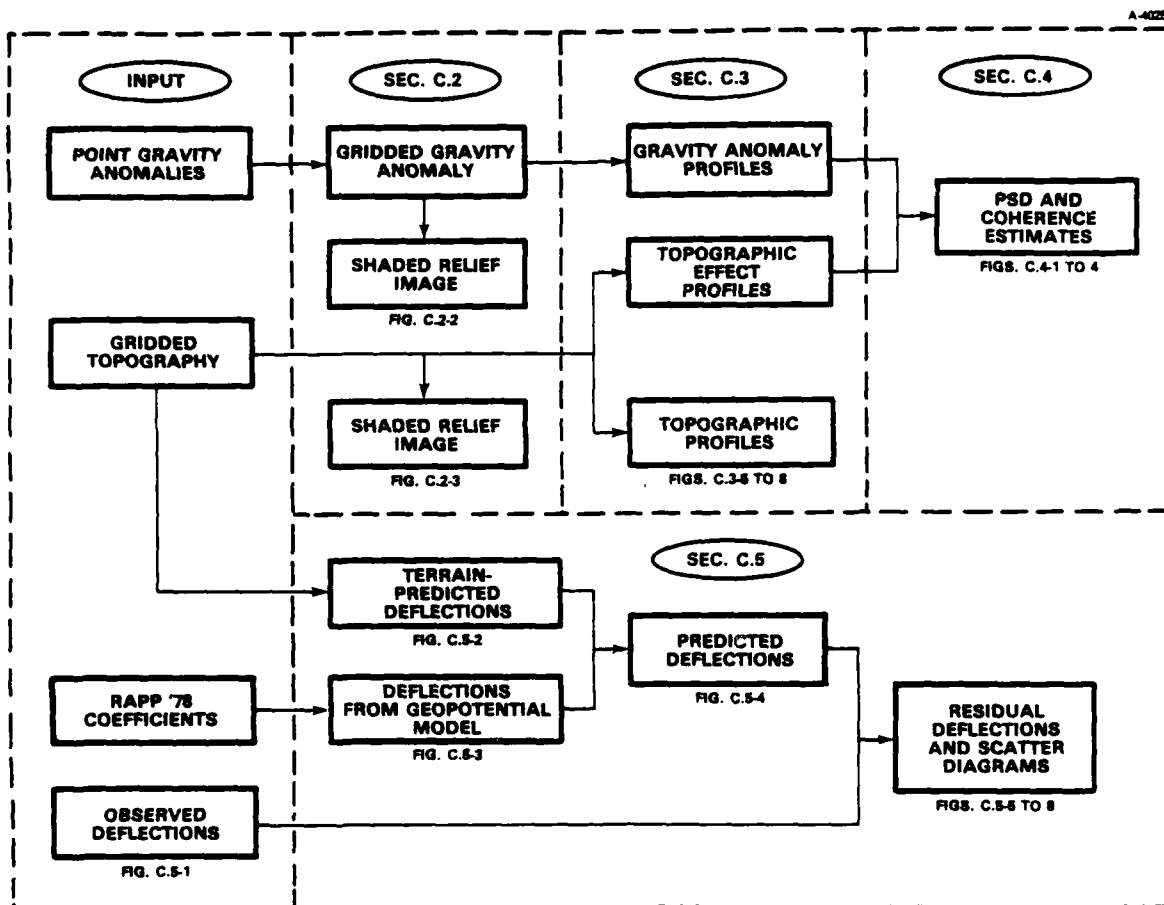


Figure 4.1-1 Overview of Terrain Effects Analyses

The second study, outlined in the lower half of Fig. 4.1-1, examines how well deflections of the vertical can be predicted from local topographic data supplemented by a long-wavelength component derived from a global geopotential model. This study is also summarized below (Section 4.4) and is documented in detail in Section C.5 of Appendix C.

The results and conclusions for each of the studies are summarized in Section 4.5. More detail will be found in Appendix C (Sections C.4.1, C.4.2, and C.5.2).

4.2 DATA USED IN THESE INVESTIGATIONS

The data used in these investigations are summarized in the left-hand column of Fig. 4.1-1:

- A set of 3855 point free-air gravity anomaly measurements, covering the region from 32 to 35 deg North and 105 to 108 deg West (White Sands study area)
- Gridded topographic data covering the same area, sampled at a density of 120 samples per degree
- A set of geopotential coefficients (Ref. 37) used to characterize long-wavelength features of the gravity field
- A set of 441 deflections of the vertical within the study area, observed by classical astrogeodetic techniques, used as truth data to evaluate the quality of prediction methods.

The free-air gravity anomaly and topographic data sets are described more fully in Section C.2 of Appendix C; Fig. C.2-1 maps the locations of the free-air gravity anomaly data points, while Figs. C.2-2 and C.2-3 are shaded relief maps, in color, of the gravity anomalies and terrain heights, respectively. The observed deflection data are described in Section C.5 of Appendix C and in Ref. 20. They are shown graphically in Fig. C.5-1.

4.3 SPECTRAL ANALYSIS OF GRAVITY DATA AND TOPOGRAPHIC EFFECT

There are three principal steps in the spectral analysis of free-air gravity anomaly data and computed topographic effects:

- Gridding the gravity anomaly data
- Selecting profiles and computing topographic effects for each profile
- Carrying out spectral analysis to estimate:
 - power spectral density (PSD) of the gravity anomalies for selected profiles
 - power spectral density (PSD) of the topographic effect for selected profiles
 - coherence between gravity anomalies and topographic effect for selected subsets of the profiles.

Gridding the data - Since the free-air gravity anomalies are measured at points unevenly distributed over the study area, it is necessary to grid the data before the spectral estimation algorithms can be applied. The gridding algorithm is described in Section C.2 of Appendix C. The resulting 121 by 121 grid includes 40 data points per degree. Note that the topographic data are already supplied in regularly gridded form. Shaded relief maps, in color, have been prepared from the gridded anomaly and topography data (Figs. C.2-2 and C.2-3, Appendix C.)

Selecting profiles - Six profiles of free-air gravity anomaly data are chosen from either rows or columns of the gravity anomaly grid described above, corresponding to east-west and north-south orientations. The locations of the three north-south and three east-west profiles, selected to include mountain and plateau terrain, are shown in Fig. C.3-2 of Appendix C.

Computing topographic effect - Topographic effects are estimated by computing the vertical component of the gravity disturbance, treating terrain-height data as a grid of vertically oriented rectangular prisms extending upward from a sea-level datum. This algorithm is described in Section C.3 of Appendix C. The computed disturbances are related to the complete Bouguer correction (Ref. 1).

With free-air gravity anomaly and topographic effect computed for each point on a given profile, it is possible to define a residual anomaly as the difference between the two. An example is given in Fig. 4.3-1 for one of the east-west profiles, designated as EW-3. This figure shows the variation of terrain elevation along the profile, the observed free-air gravity anomalies, the computed topographic effect, and the residual anomaly. It is evident from the figure that, for this profile, the observed free-air gravity anomalies are well correlated with topography, but that the residual anomaly has nearly as much variability as the observed anomaly. Similar figures for all six profiles are found in Appendix C.

Estimating PSD and coherence - The purpose of the power spectral density computations, described in detail in Section C.4 of Appendix C, is to investigate differences between types of terrain (mountainous and plateau) and to examine the significance of directional anisotropy (east-west compared with north-south). In order to make spectral comparisons, the data segments are pooled into four groups:

- Plateau, oriented east-west
- Plateau, oriented north-south
- Mountain, oriented east-west
- Mountain, oriented north-south

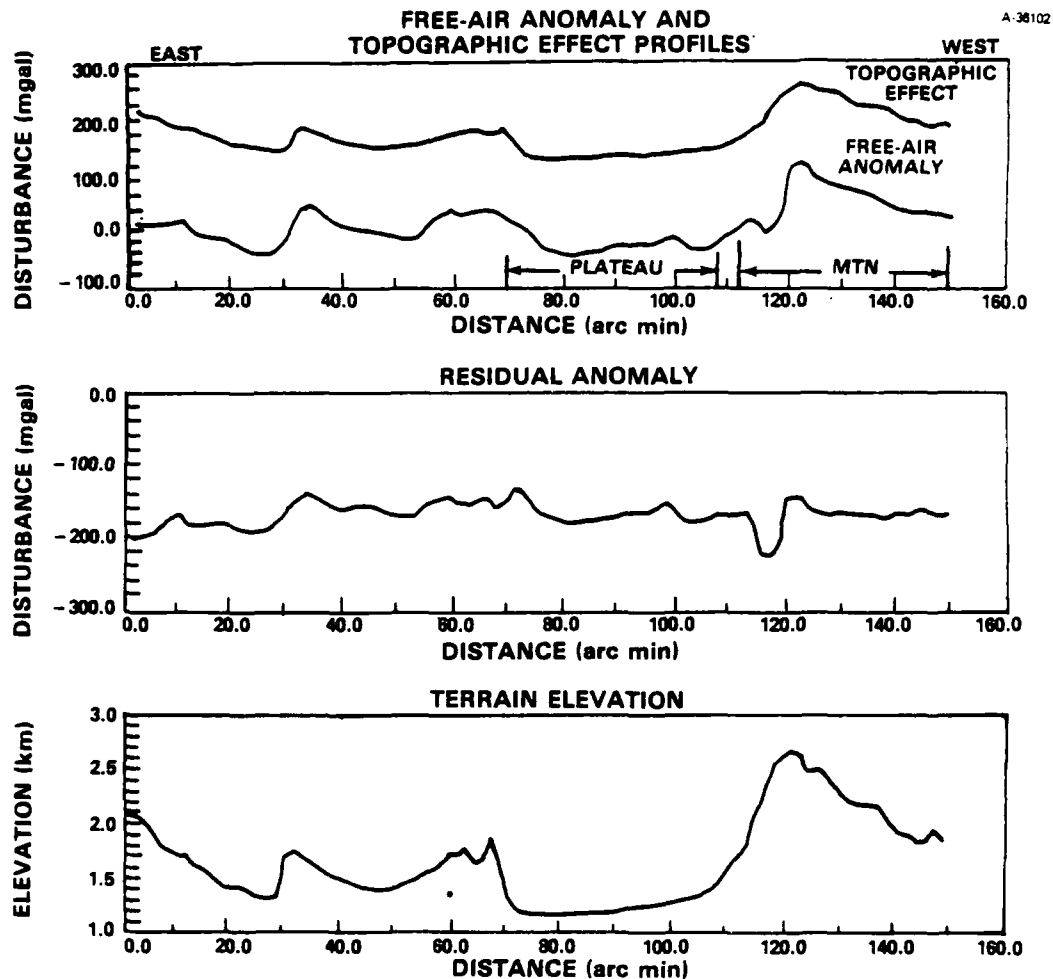


Figure 4.3-1 Profile EW-3

Power spectra for each of the four groups are computed by state-space modeling (Ref. 44), as described in Appendix C. In addition, the relation between the gravity anomaly and topographic effect data series is summarized in a coherence plot, which shows the degree of correlation as a function of spatial frequency. PSD and coherence plots for all four groups are presented and discussed in Section C.4 of Appendix C; one example is shown here as Fig. 4.3-2.

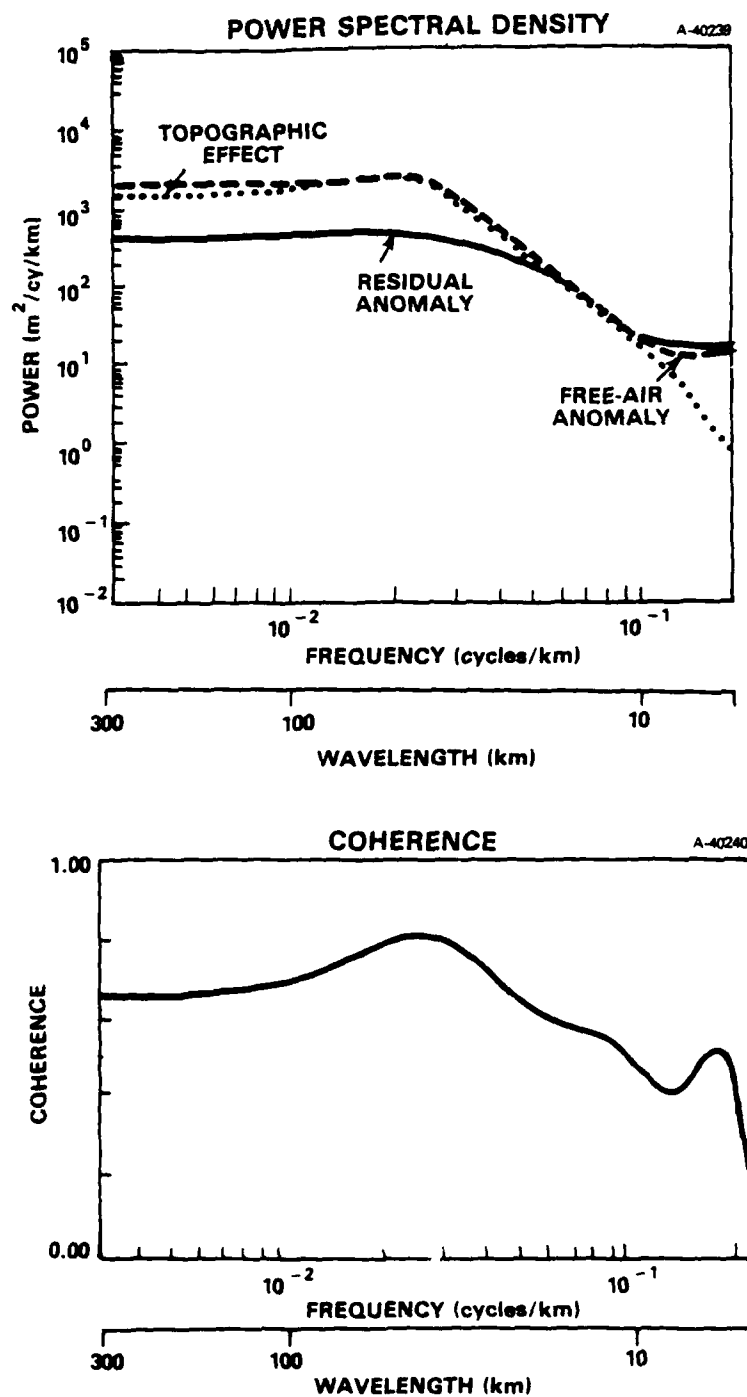


Figure 4.3-2 East-West Mountainous Terrain

In this example of mountainous terrain (east-west orientation), the free-air anomaly and topographic effect have similar spectra (upper plot of Fig. 4.3-2). The spectra are nearly flat down to wavelengths of about 45 km. The coherence is significant over a broad range of wavelengths, showing a peak value of 0.8 at a wavelength of about 40 km. These plots are typical of east-west profiles (but not north-south), as discussed in Section C.4.1 of Appendix C. A brief summary and interpretation of the results of profile spectral analysis is provided in Section 4.5.

4.4 PREDICTING DEFLECTIONS OF THE VERTICAL FROM LOCAL TOPOGRAPHY

There have been a number of investigations (Refs. 20 and 21, for example) of the contribution of terrain or topographic effects in the computation of deflections of the vertical from gravity anomaly data. This phase of TASC's study, documented in Section C.5 of Appendix C, examines the significance of topographic effects in mountainous areas from a complementary point of view. Deflections of the vertical are computed directly for 441 locations within the study area at which observed astrogeodetic deflections are available, using:

- Terrain height data to supply local or short-wavelength information
- A global geopotential model to supply long-wavelength information.

Gravity anomaly data are not used. The deflections predicted by this simple method are then compared with the astrogeodetic truth data. The results are discussed in Section C.5.1 of Appendix C.

A graphical overview of the relative quality of this simple prediction method is given in Fig. 4.4-1, which shows the observed (left-hand map) and predicted (right-hand map) deflections in vector-arrow form. The length and direction of an arrow indicate magnitude and direction of the deflection of the vertical; the tail of the arrow is at the location of the deflection station. It is readily observed that the predicted deflections correlate well with the direction of the observed deflections, but the predicted magnitudes tend to be smaller.

Another view of the correlation between observed and predicted deflections of the vertical is given by scatter diagrams like the one shown, as an example, in Fig. 4.4-2. In this diagram the predicted value of the east-west component of the deflection of the vertical is shown as the x-component, and the corresponding true value is shown as the y-component. Two conclusions may be drawn from Fig. 4.4-2:

- The tight clustering of the points expresses a high coefficient of correlation (approximately equal to 0.9)
- The slope of the least-squares regression line differs from one, reflecting a systematic under-estimation of the east-west component of the deflection.

Further discussion is found in Appendix C.

4.5 SUMMARY OF RESULTS AND CONCLUSIONS

For the first investigation reported in this chapter, the spectral analysis of gravity data and topographic effect, the results are presented and interpreted in Sections C.4.1 and C.4.2 of Appendix C. An example of the graphical output

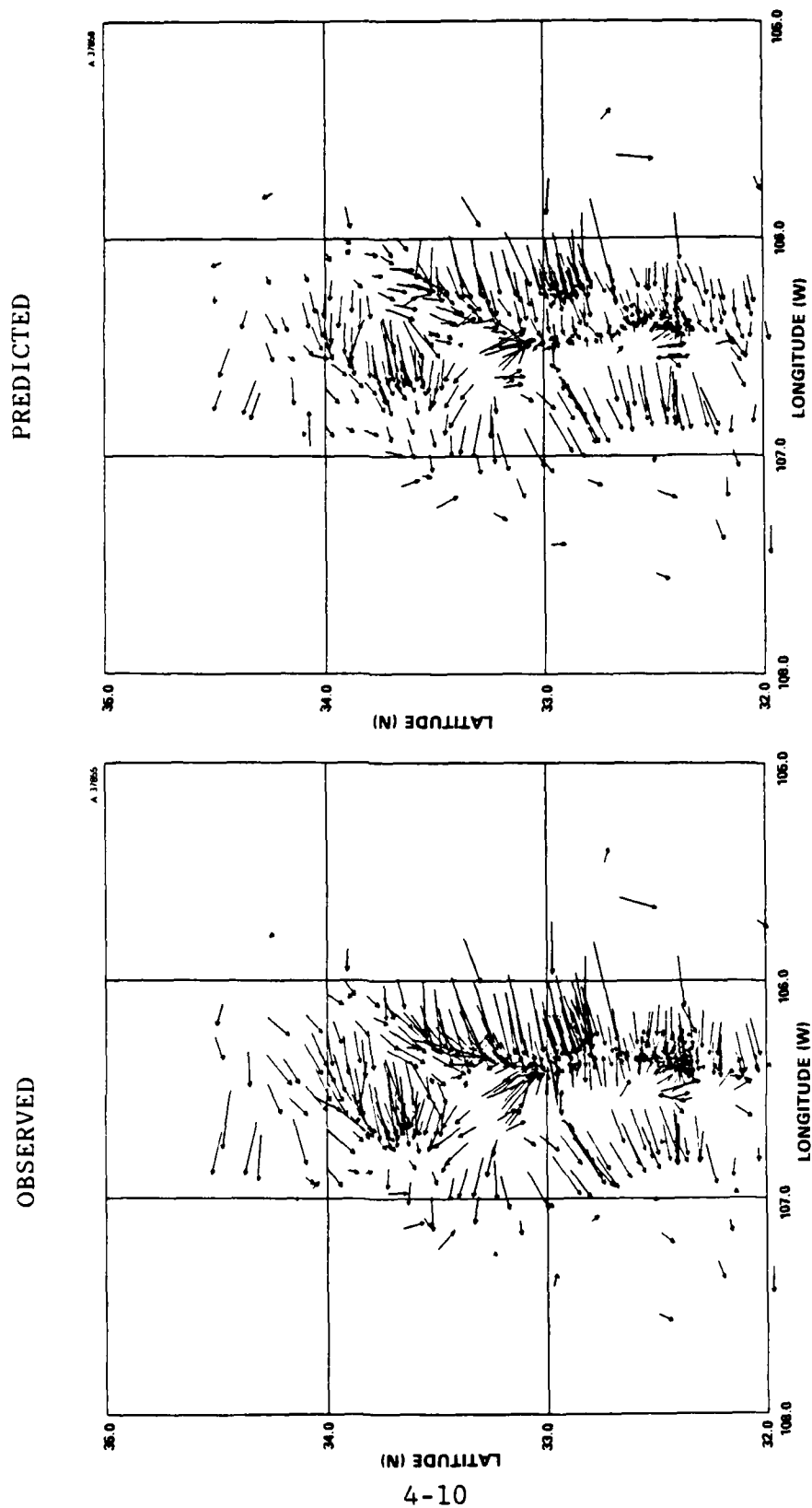


Figure 4.4-1 Observed and Predicted Deflections of the Vertical

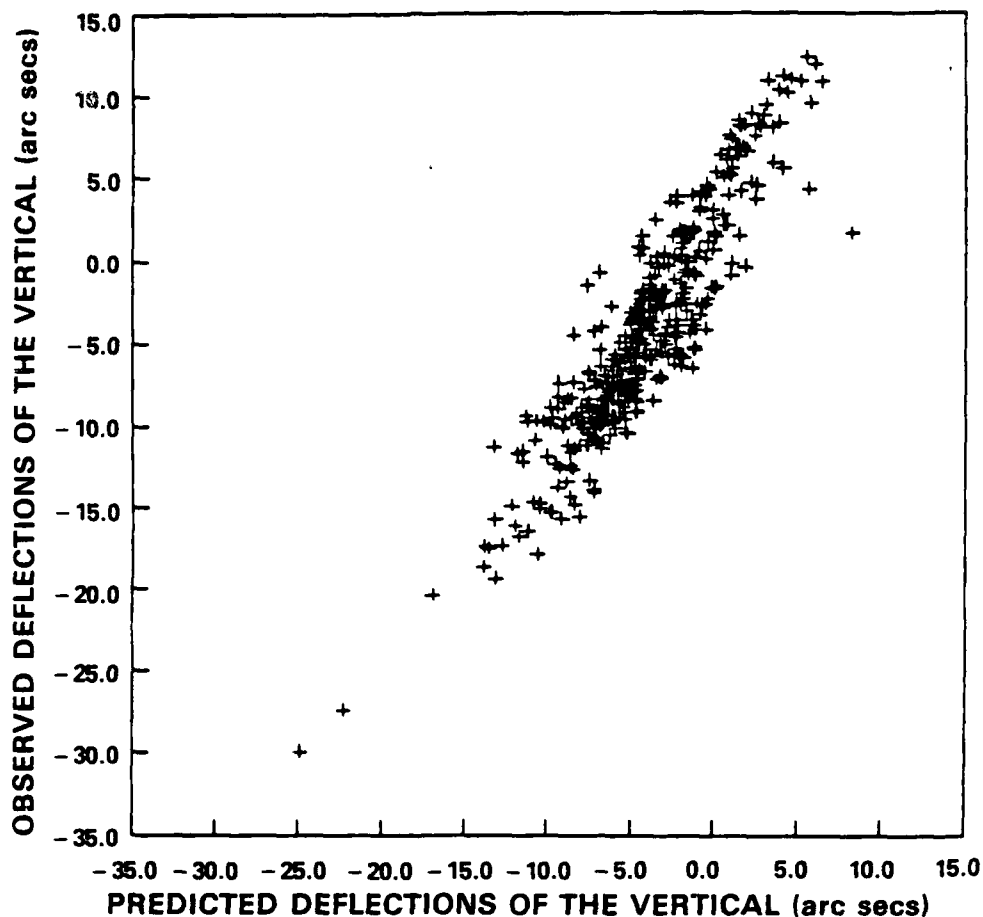


Figure 4.4-2 Scatter Diagram of East Vertical Deflection Component

has been shown in Section 4.3 (Fig. 4.3-2). The principal conclusions are:

- Anisotropy (associated with the regular north-south strike of geologic and terrain features in the White Sands study area) is indicated by significant differences between north-south and east-west data groups. For example, there is a local peak in the PSDs and coherences in the east-west groups, but not in the north-south groups.

- Mountain and plateau areas differ in several ways, among which are:
 - Coherence between topographic effects and free-air gravity anomalies is low at long wavelengths for plateau areas, but high at long wavelengths in the mountains
 - In plateau areas the power in the topographic effect is lower than the power in the free-air and residual anomalies, while for mountain areas the residual anomaly has the lowest power at long wavelengths.

All of these differences are consistent with the anisotropic and nonstationary nature of the terrain and gravity anomalies in the White Sands region.

The results of the second phase of TASC's investigation, the prediction of deflections of the vertical from local topographic data, are summarized and discussed in Section C.5.1 of Appendix C. Examples of the results, in graphical form, have been shown in Section 4.4 (Figs. 4.4-1 and 4.4-2). The major conclusion is a confirmation of the importance of accounting for local topographic effects in the computation of deflections of the vertical, since -- in this predominantly mountainous region -- the topographic effect by itself accounts for most of the deflection signal.

5. NEW DERIVATION OF THE FFT TERRAIN
CORRECTION ALGORITHM

The gravimetric terrain correction is important in mountainous areas, but is very time consuming to compute in its exact form, since it is a nonlinear function of the terrain elevation $h(x,y)$. Recently, an approximate form of the terrain correction, in terms of two-dimensional linear convolution integrals involving h and h^2 , has been derived (Refs. 33 and 34). The convolutions may be performed efficiently using gridded terrain data and the Fast Fourier Transform (FFT), by virtue of the convolution theorem (e.g., Appendix A.4). This approach has been successfully applied to compute the complete Bouguer anomaly in the White Sands area (Ref. 21), for example. However, the published derivations include ad hoc steps that, apparently, are required to ensure good numerical behavior.

This chapter, in contrast, describes the essentials of a new derivation (Ref. 35) of the approximate terrain correction that avoids such ad hoc steps. It shows a more rigorous and direct route to the same final result and clarifies the physical meaning and optimum choice for a length parameter that was introduced arbitrarily in Refs. 33 and 34. The presentation here is brief and descriptive; further details are given in Appendix B.

The terrain correction is to be added to the gravity anomaly following subtraction of the simple Bouguer (slab) correction. At a point P , it corresponds to the effect of the true topography minus a slab of height h_p , where $h_p = h(X_p, Y_p)$

is the elevation of P. This is shown schematically in Fig. 5-1. Above the computation point P there are hills of excess mass and below P there are valleys of (effectively) negative mass. Both have the effect of decreasing the observed gravity anomaly; the terrain correction is always positive. Assuming a constant density ρ for the topography and denoting the gravitational constant by G, the exact (flat-earth) terrain correction is

$$c(x_p, y_p) = G\rho \iint dx dy \int_{h_p}^{h(x,y)} \frac{(z - h_p) dz}{[(x_p - x)^2 + (y_p - y)^2 + (h_p - z)^2]^{3/2}} \quad (5-1)$$

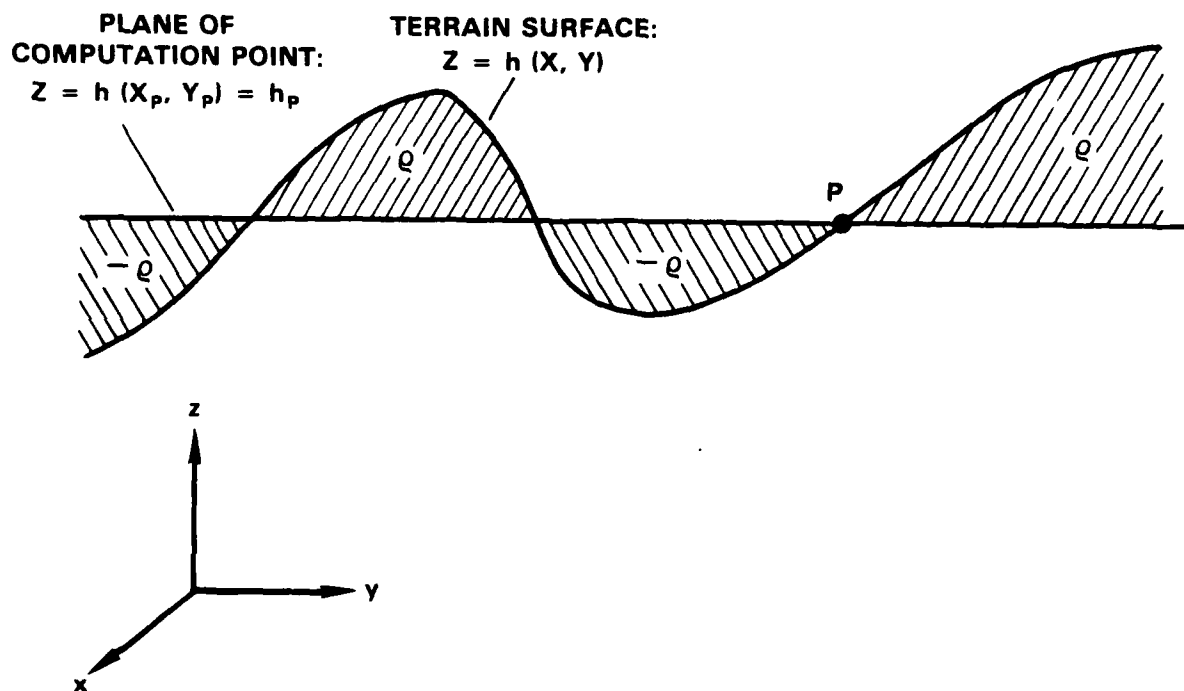


Figure 5-1 Terrain Correction

Starting from Eq. 5-1, previous derivations (Refs. 33 and 34) of the FFT terrain correction algorithm have consisted of:

1. An approximation leading to convolutions of h and h^2 with the singular kernel

$$(x^2 + y^2)^{-3/2}$$

which is not integrable over the x - y plane and whose Fourier transform is nonexistent

2. Replacement of the singular kernel by

$$(x^2 + y^2 + a^2)^{-3/2}$$

which has the Fourier transform

$$\frac{2\pi}{a} \exp(-2\pi a \sqrt{u^2 + v^2})$$

(following the convention of Appendix A.4 and Ref. 32).

(In Ref. 33 an alternate but equally arbitrary version of step 2 is also applied.)

In fact, however, convolution of $h(x,y)$ and its square with the modified kernel is not only more tractable numerically, but also more accurate than convolution with $(x^2+y^2)^{-3/2}$, for a range of nonzero values of a . This result follows directly from the exact formula (Eq. 5-1) by means of a single approximation in which $(h_p - z)^2$ is replaced by a constant a^2 ,

$$c(x_p, y_p) \cong G_0 \iint dx dy \int_{h_p}^{h(x,y)} \frac{(z - h_p) dz}{[(x_p - x)^2 + (y_p - y)^2 + a^2]^{3/2}}$$

(5-2)

Starting from Eq. 5-2, integration over z and expansion of the numerator lead directly to convolution of h and h^2 with $(x^2 + y^2 + a^2)^{-3/2}$ (for details, see Appendix B). This yields the same result as steps 1 and 2 above, but now it is clear that a^2 represents an average value of $(h_p - z)^2$ and that its optimal value always exceeds zero. The two steps of approximation applied in Refs. 33 and 34 are unnecessary and partially cancel one another.

As a demonstration that the best value of a is indeed nonzero, Fig. 5-2 shows a plot of rms error in the terrain correction vs the value of a for a sample of 100 points in a

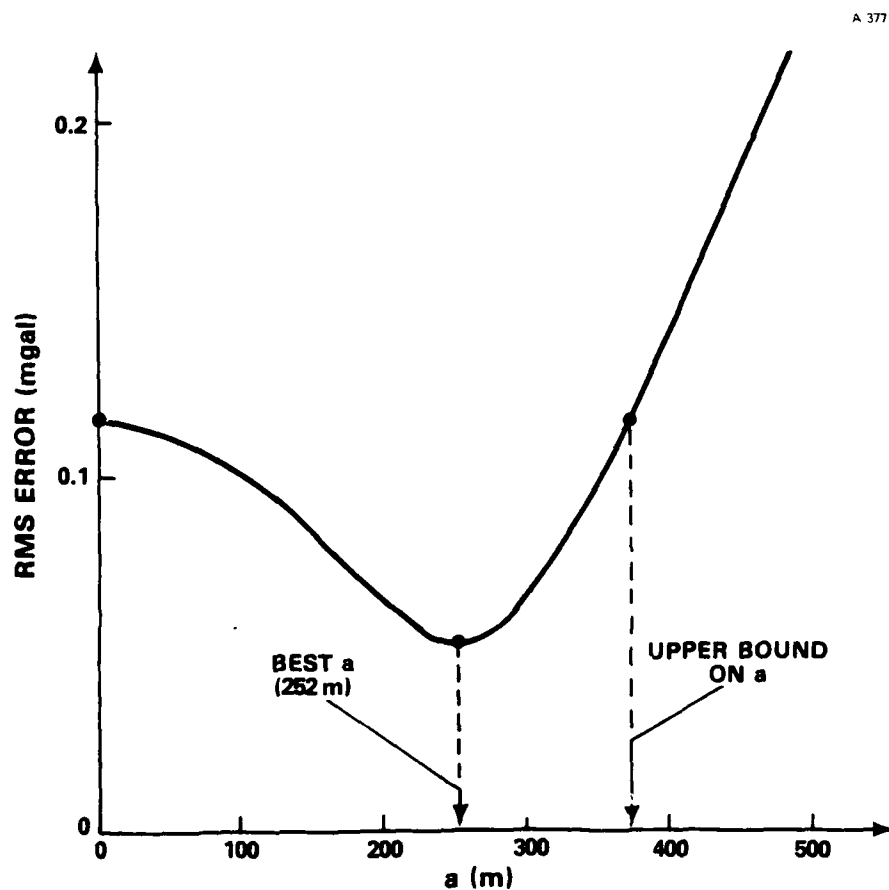


Figure 5-2 White Sands Terrain Example

rugged portion of the White Sands area 33.1 to 33.5 deg North and 105.5 to 105.9 deg West. The error was computed by subtracting the approximate terrain correction (Eq. 5-2), computed in terms of convolutions, from the result of evaluating the exact formula (Eq. 5-1) by numerical (bicubic spline) integration. It is clear that the best value of a for the study case is about 250 m, and that any choice of a up to an upper-bound of about 375 m will yield a lower rms error than $a = 0$. The rms errors shown are quite small, but the maximum absolute errors are larger; 0.84 mgal for $a = 0$ vs. 0.28 mgal for $a = 250$ m. (The appropriate choice of a leads to a factor-of-3 improvement.)

In summary, this chapter and the more detailed derivation and discussion in Appendix B show that the FFT terrain correction algorithm is, in fact, more rigorous than indicated by its proponents in Refs. 33 and 34, and that the optimal value of the parameter a always exceeds zero.

6. NUMERICAL EXPERIMENTS WITH GEOFAST ALGORITHM

6.1 SUMMARY OF APPROACH

The GEOFAST Algorithm is described in Appendix A.3. This technique computes minimum-variance estimates of geodetic quantities (equivalent to least-squares collocation) in a highly efficient manner. The algorithm accepts two-dimensional gridded data, and takes advantage of the structure of stationary statistical gravity models. High computational efficiency is achieved by frequency-domain techniques based on the Fast Fourier Transform (FFT). This approach yields a computational load proportional to $N \log N$, where N is the number of data points, as compared to N^3 for the matrix inversion used in standard collocation. Appendix A.3 describes how the covariance matrices of the collocation method are transformed into the frequency domain by a two-dimensional windowed FFT. The resulting frequency-domain covariance matrices are approximately block-banded, in the sense that the out-of-band elements are below a threshold, ϵ . There is a tradeoff between the number of bands retained, m_B , and the accuracy of the approximation, ϵ . The computer load for the GEOFAST solution is asymptotically proportional to m_B^2 as illustrated in Fig. 6.1-1 for a 32 by 32 grid ($N = 1024$) using the VAX 11/780 computer. For the case shown, a standard collocation solution would require more than two hours (vs 15 min for GEOFAST with $m_B = 8$).

Two sets of numerical experiments were conducted with the GEOFAST algorithm. The first set used synthetic marine gravity data in an ocean trench area. This data set was generated using the Rapp 1981 spherical harmonic expansion to

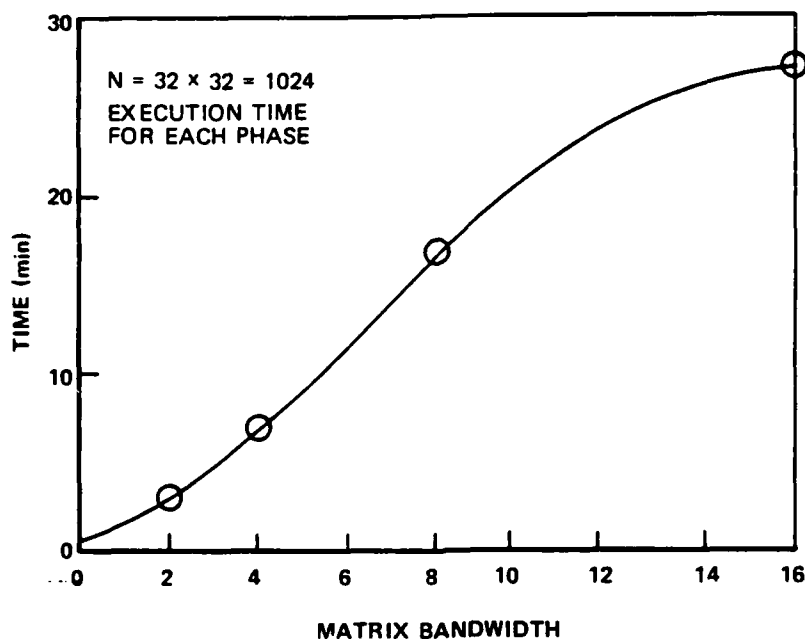


Figure 6.1-1 GEOFAST Computer Time for $N = 1024$

degree and order 180 (Ref. 38). Such a model resolves wavelengths down to about 200 km. The second set of experiments used a higher frequency local model developed by TASC and NSWC for gravity gradiometer evaluation (Ref. 39). This data set is based on a mass dipole realization and contains wavelengths as short as 5 km.

The experiments consisted of using the GEOFAST algorithm to compute deflections of the vertical from gravity anomalies for each of the two data sets. Parameters which were explored include the data extent, grid spacing, GEOFAST bandwidth, covariance models, and measurement noise level. A description of the two data sets and the results of the experiments are given in the following sections.

6.2 SYNTHETIC MARINE GRAVITY DATA SET

This data set was generated from the Rapp 1981 world-wide spherical harmonic expansion to degree and order 180 (Ref. 38). The test area selected is a 36 deg square in the Western Pacific which includes a significant ocean trench (Fig. 6.2-1). This model expansion is capable of resolving only wavelengths longer than about 200 km. Both gravity anomalies and deflections of the vertical are generated for grid spacings of 0.5 deg and 0.25 deg. The smaller spacing represents "oversampling" but is included to study algorithm dependence on the number of datapoints. The data sets obtained constitute the "truth data" for the experiments described below.

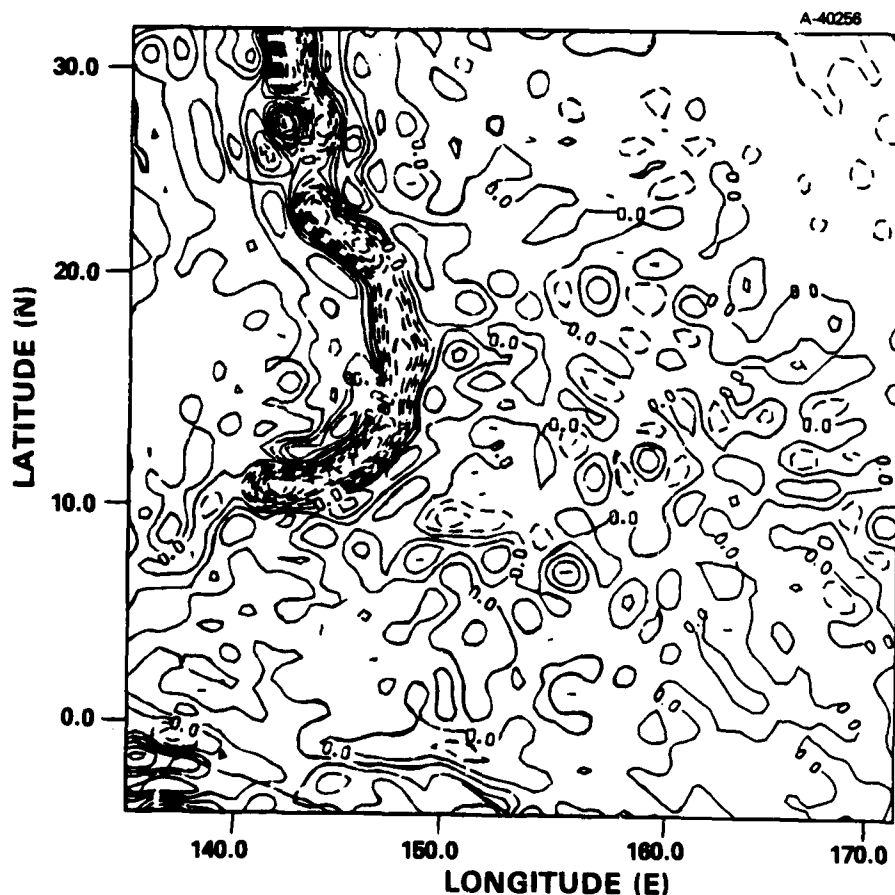


Figure 6.2-1 Synthetic Marine Gravity Anomalies (Rapp Model to Degree 180 Contoured at 20 mgal)

To study the effect of high-order reference fields on gravity estimation techniques, the Rapp model is also used to generate anomalies and deflections for spherical harmonic degrees and orders 91 through 180. These data (Fig. 6.2-2) correspond to subtracting a degree 90 reference field from the data prior to GEOFAST processing. The resulting data set contains only the high-frequency portion of the field (in this case, wavelengths between 200 and 400 km). The removal of the reference field increases the accuracy of the estimates. It is compensated for by restoring the reference field to the estimated quantities.

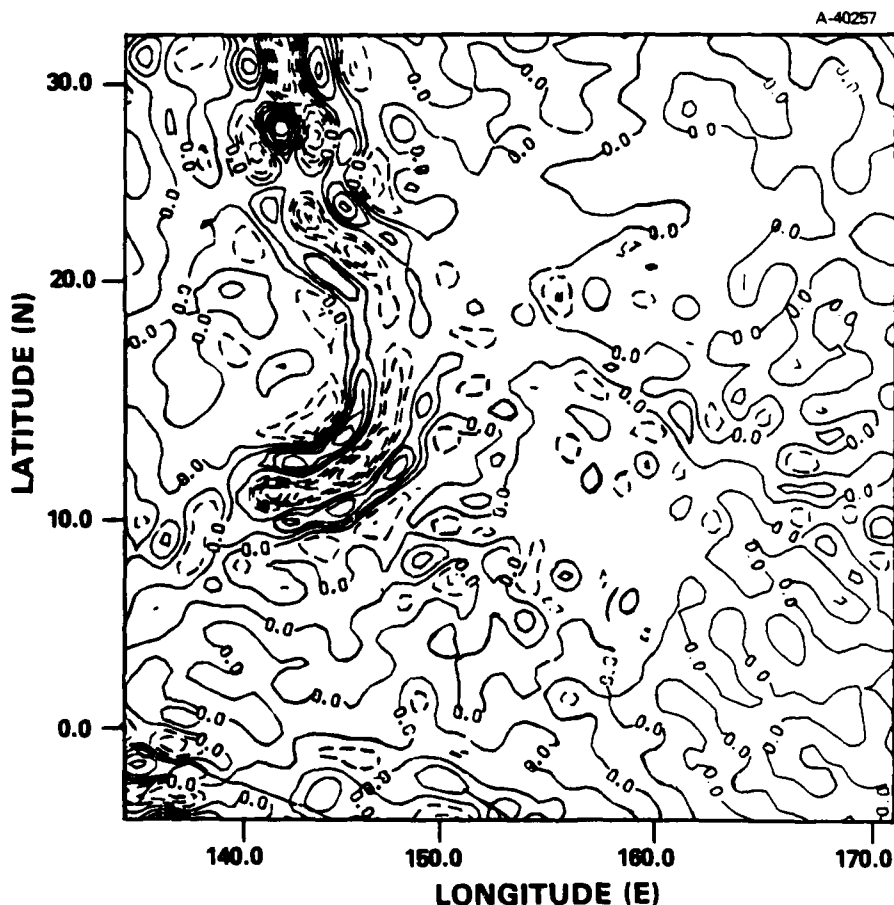


Figure 6.2-2 High-Frequency Synthetic Marine Gravity Anomalies (Rapp Model Degrees 91-180 Contoured at 20 mgal)

6.3 RESULTS WITH SYNTHETIC MARINE DATA

6.3.1 Description of Test Cases

The first three test cases use truth data from the high-frequency Rapp model (degrees 91 through 180). The extent of the data is reduced to the northwest 15 deg square in Fig. 6.2-2 (latitude 17 deg to 32 deg North, and longitude 135 deg to 150 deg East). Since the trench runs north-south, east deflections of the vertical were estimated from gravity anomalies. The truth data (both anomalies and deflections) were gridded at 0.5 deg (Figs. 6.3-1 and 6.3-2) and at 0.25 deg (Fig. 6.3-3). The resulting data sets contain 900 points (30 by 30) and 3600 points (60 by 60), respectively. The gravity anomaly in this region varies from -109 mgal to 137 mgal, while the east deflection varies from -19 arc sec to 25 arc sec. The rms value for the east deflection is 6 arc sec.

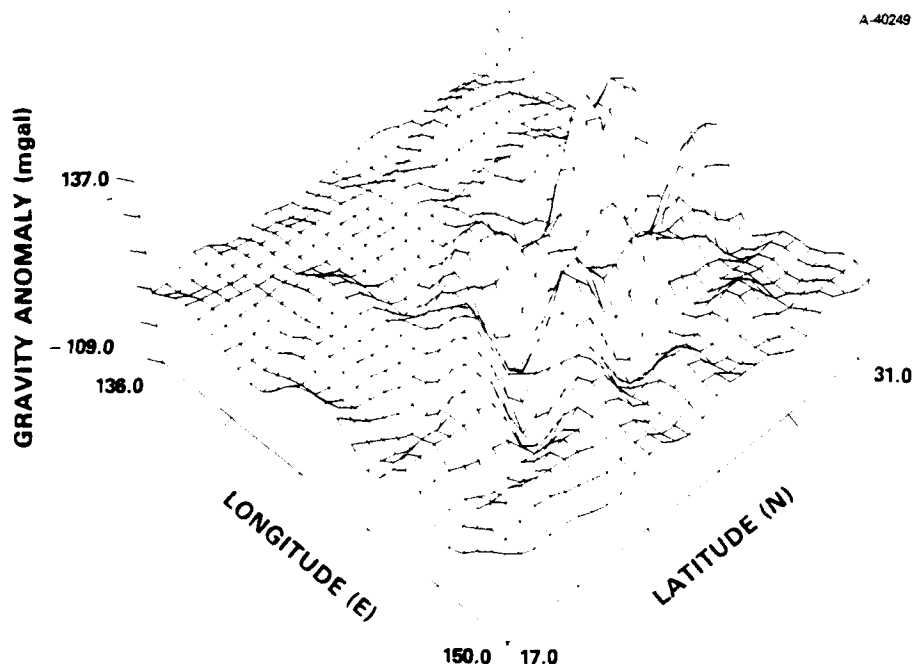


Figure 6.3-1 Synthetic Gravity Anomaly Data (Rapp Model Degrees 91-180 at 0.5 deg Spacing)

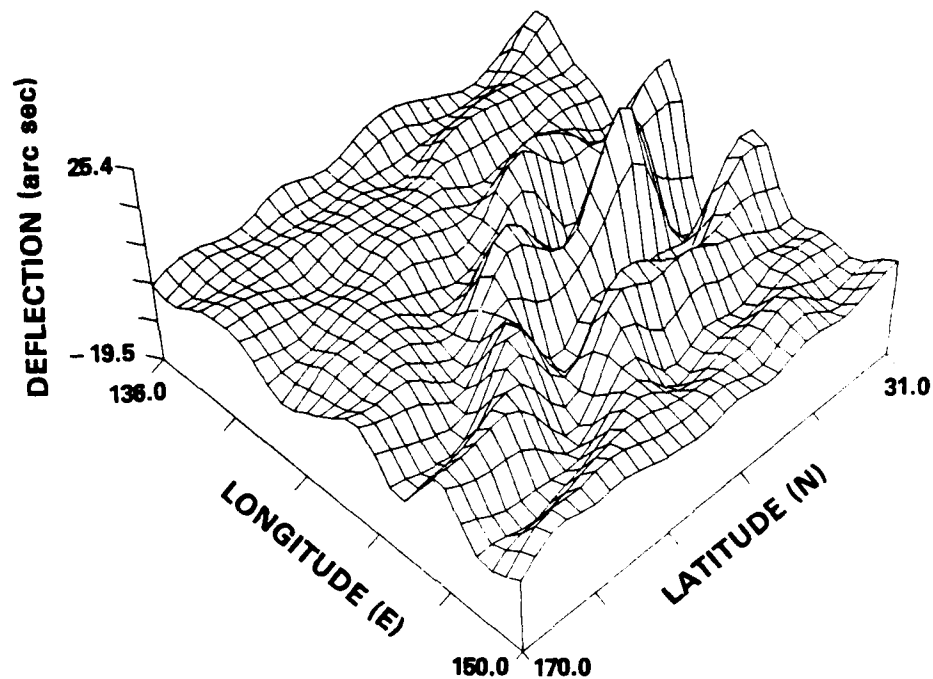


Figure 6.3-2 Synthetic East Deflection Data (Rapp Model
Degrees 91-180 at 0.5 deg Spacing)

A-40245

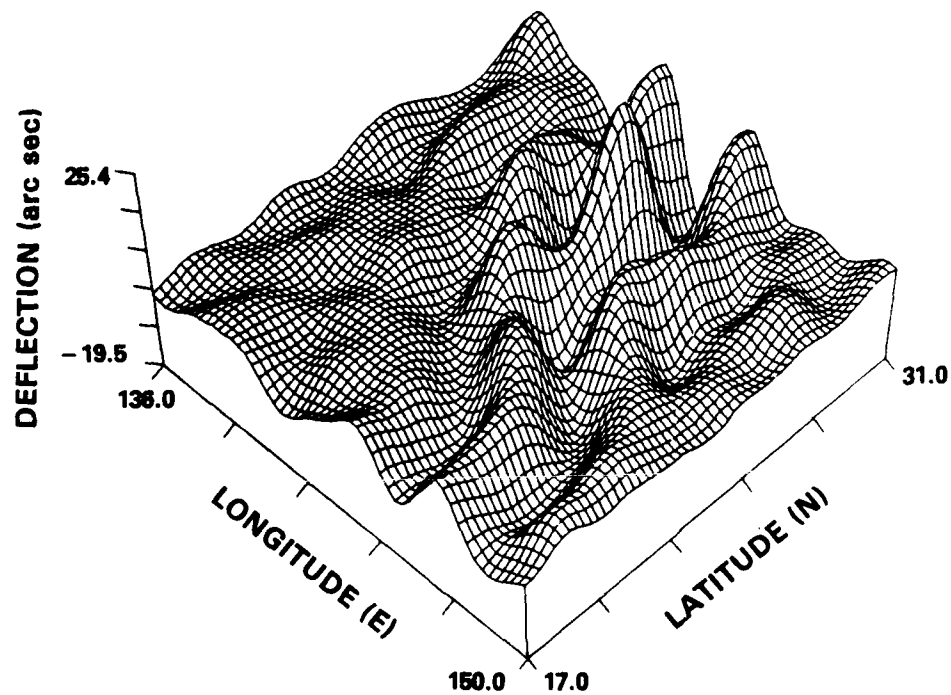


Figure 6.3-3 Synthetic East Deflection Data (Rapp Model
Degrees 91-180 at 0.25 deg Spacing)

The covariance model for the GEOFAST estimation was the Attenuated White Noise (AWN) model developed at TASC (Ref. 24). This model has several desirable properties, especially the availability of closed-form expressions for all related gravity quantities, and the ability to closely fit empirical covariance data (see Appendix A.2.3). For this test, a single-shell AWN model was chosen with a correlation distance of 0.5 deg. It is not necessary to specify the gravity model field strength (variance) since this scale factor cancels out in the estimation gains. For the initial test cases the effect of measurement noise (uncertainty in the anomaly data) was ignored and the exact Rapp model data were used for estimation. Degradation in the estimates due to measurement noise is analyzed separately by a perturbation approach and is discussed in Section 6.3.3.

6.3.2 Results for Noise-Free Estimation

Table 6.3-1 displays the results of three test cases:

- 0.25 deg grid with $m_B = 0$
- 0.25 deg grid with $m_B = 4$
- 0.50 deg grid with $m_B = 0$.

Estimation error is given in units of arc sec for the central 12 deg square (within the 15 deg square of data). This restriction reduces the influence of edge error due to data truncation, which is common to all estimation methods. The deflection estimates are within 0.2 arc sec (standard deviation) for all cases and within 0.7 arc sec (absolute maximum).

TABLE 6.3-1
GEOFAST ESTIMATION ACCURACY

RESOLUTION		EFFICIENCY		ESTIMATION ERROR (arc sec)**		
GRID (deg)	POINTS	m _B	TIME (min)*	MEAN	SIGMA	MAXIMUM
0.25	3600	0	4	0.001	0.15	0.70
0.25	3600	4	30	0.003	0.09	0.31
0.50	900	0	1	0.003	0.17	0.59

*Computer time for VAX 11/780

**Central 12 deg square

As expected, results are best at the finest grid and largest bandwidth -- the rms and maximum errors are reduced by a factor of two (0.09 arc sec and 0.31 arc sec, respectively) compared to the coarse grid and zero bandwidth. However, the effect of reducing the grid spacing alone (at zero bandwidth) is only a modest improvement in accuracy. This result is due to the oversampling (0.25 deg is about 28 km) when the data wavelengths are greater than 200 km. The mean error is small (less than 0.003 arc sec) in all cases because of removal of the high order reference field (Rapp model to degree 90).

Figure 6.3-4 gives a detailed plot of the estimation error at each grid point for two of the cases. In general, the error is largest near the edges or where the field is largest, and varies from -0.77 arc sec to 0.67 arc sec for the best case.

The efficiency of the GEOFAST algorithm is also evident from Table 6.3-1. Deflections accurate to 0.2 arc sec rms are obtained in 1 min of VAX 11/780 computer time. The table also

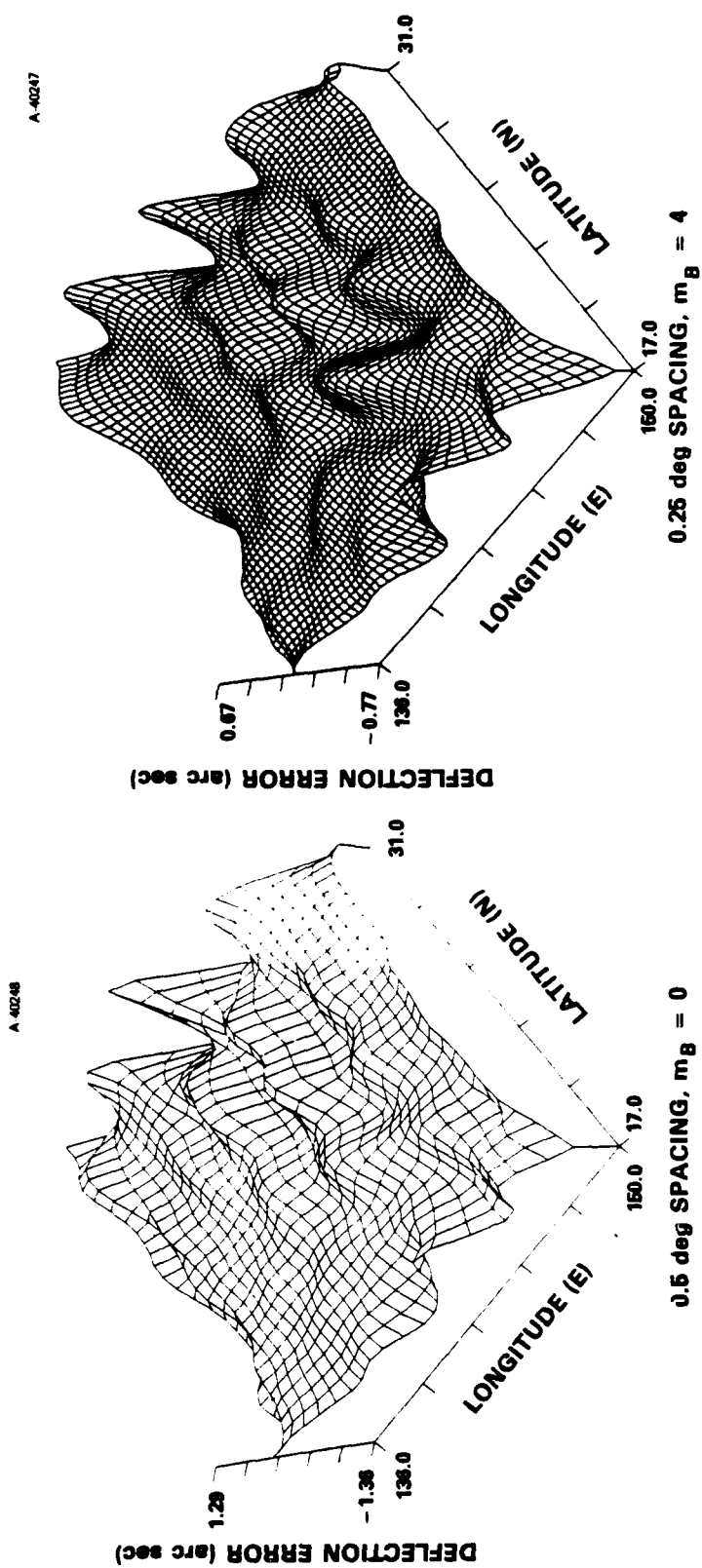


Figure 6.3-4 East Deflection Estimation Error (GEOFAST Algorithm with Gridding at 0.5 deg and 0.25 deg and Bandwidths of 0 and 4)

shows the increase in computer time to four minutes when the grid density is doubled. Increasing the bandwidth has the largest influence on computer loading, raising computing time for 3600 data to 30 minutes when $M_B = 4$. These results demonstrate the tradeoff available through choice of the bandwidth to achieve a desired accuracy level commensurate with the inherent data quality. In the standard collocation approach, the user is forced to accept (and pay for) full numerical accuracy which substantially exceeds the confidence limits set by measurement, gridding, and truncation errors. Note that the computer time required for standard collocation using 3600 data would be greater than GEOFAST by at least two orders of magnitude. (An exact determination of this is not practical as collocation runs using more than 500 data at once are prohibitively expensive.)

Effect of Reference Field Removal -- To quantify the benefits of removing a high order reference field from the data (as was done in the three cases discussed above), the first test case (0.25 deg grid and $m_B = 0$) was repeated using data from the full Rapp model (through degree and order 180). The results are shown in Table 6.3-2. Note that removal of the reference field reduces the rms field strength from 9.2 arc sec to 6.1 arc sec. The results show a sizeable mean error (-1.5 arc sec) when no reference field is removed. This effect results from the lack of low-frequency (long wavelength) information in local data and could have been reduced substantially by removing a low-order reference field (e.g., to degree and order 12). However, when no reference field is removed, the degradation in standard deviation (by a factor of 5) and maximum error (by a factor of nearly 10) are quite dramatic and justify the use of the high-order reference field.

TABLE 6.3-2
EFFECT OF HIGH-ORDER REFERENCE FIELD

REFERENCE FIELD REMOVED	REMAINING FIELD rms (arc sec)	ESTIMATION ERROR [*] (arc sec)		
		MEAN	SIGMA	MAXIMUM
None	9.16	-1.520	0.690	2.960
Degree 90	6.14	0.001	0.120	0.310

*Central 5 degree square

For any geodetic algorithm, estimation errors due to finite extent of data decrease towards the center of the estimation region. Thus, the estimation errors shown in the second row of Table 6.3-2 (based on the 5 deg square) are slightly smaller than the results in the first row of Table 6.3-1 (based on the 12 deg central square of the same GEOFAST output).

6.3.3 Effect of Noisy Observations on Estimation Results

The results in Table 6.3-1 and Table 6.3-2 are based on perfect (error-free) anomaly data, and thus are only a lower bound on attainable accuracy. The effect of measurement errors on these results was assessed analytically, since the data errors are normally a small fraction of the field strength (high signal-to-noise ratio). The analysis is based on the Wiener smoother formulation for continuous data in an infinite plane (Refs. 40, 41), except that the gridding (discrete sampling) is accounted for. The gravity field is assumed to be band limited and the sample spacing to satisfy the Nyquist criterion. As a result, there is no aliasing error due to

sampling. These conditions are satisfied here since the data in the Rapp model contain no spectral energy at frequencies higher than the Nyquist frequency ($1/2L$ where L is the grid spacing).

The Wiener transfer function (between east deflection and anomaly), corresponding to the AWN model for the data plus white noise, is easily obtained in the frequency domain. To a first (linear) approximation, the effect of the noise is additive at the variance level and can be calculated separately as a "noise-induced" error in the estimates. This error is combined with the noise-free GEOFAST estimation error (from Table 6.3-1) to give the total estimation error for noisy data. The result of this calculation for various noise levels is shown in Table 6.3-3. For example, for 5 mgal anomaly errors on a 0.25 deg grid, the effect is to degrade the total estimation error from 0.15 arc sec to 0.22 arc sec rms.

TABLE 6.3-3
EFFECT OF MEASUREMENT ERROR

GRID (deg)	MEASUREMENT ERROR rms (mgal)	NOISE-INDUCED ERROR rms (arc sec)	TOTAL ESTIMATION ERROR rms (arc sec)
0.25	0	0.00	0.15
	1	0.03	0.15
	2	0.07	0.17
	5	0.16	0.22
0.50	0	0.00	0.17
	1	0.04	0.17
	2	0.08	0.19
	5	0.20	0.26

6.4 SYNTHETIC LOCAL GRAVITY DATA SET

This data set was generated for use in the gravity gradiometer testing program (Ref. 39). A mass dipole model was constructed with prescribed statistical properties. The statistical gravity model, representative of the gradiometer test area in north Texas, is specified by a seven-shell AWN gravity potential model as shown in Table 6.4-1. The resulting value of rms vertical disturbance (equivalent to the gravity anomaly for a flat-earth approximation) is 31.4 mgal. This model has significant spectral power at wavelengths of 10 km (Fig. 6.4-1).

Synthetic data were generated from the mass dipole model for the vertical gravity disturbance (equivalent to gravity anomaly) and the horizontal gravity disturbances (equivalent to deflections of the vertical). These data consist of a 500 km square gridded at 5 km spacing and constitute the truth data for the experiments described below. As with the synthetic marine gravity data, the GEOFAST algorithm is used to estimate the east gravity disturbance from the vertical gravity disturbance.

TABLE 6.4-1
AWN STATISTICAL GRAVITY MODEL

SHELL NO.	DEPTH (km)	RMS POTENTIAL (mgal·km)
1	2.1	2.3
2	5.0	11.0
3	16.0	72.0
4	52.0	580.0
5	161.0	2300.0
6	861.0	7000.0
7	2150.0	33000.0

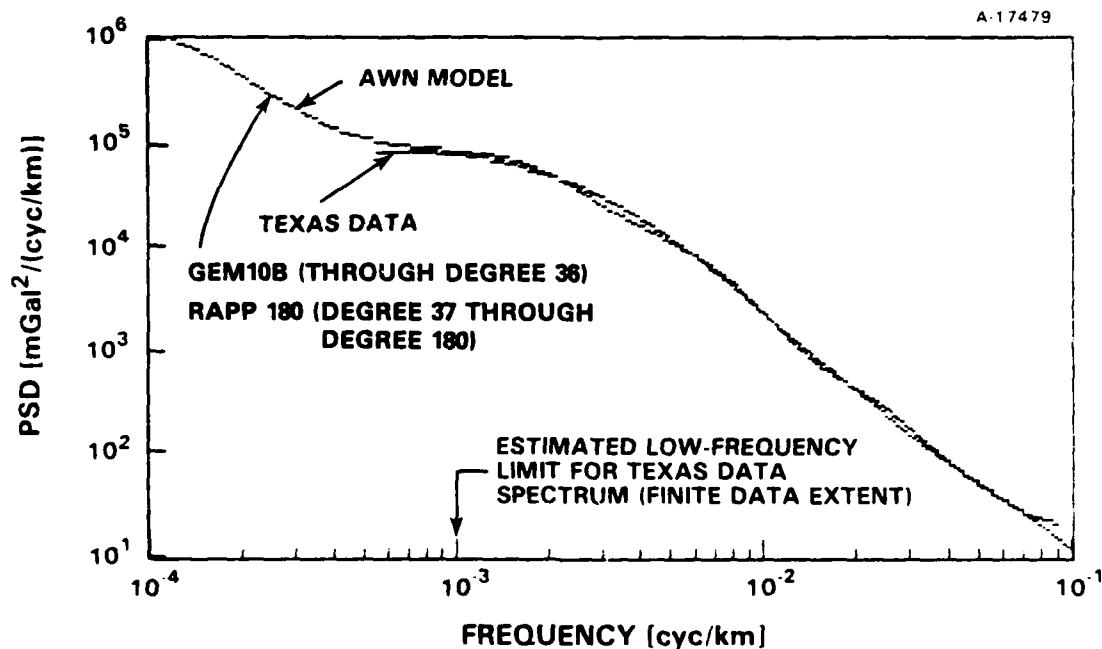


Figure 6.4-1 Along-Track Vertical Disturbance Spectra

Figure 6.4-2 displays a surface plot of a 150 km square region of the east gravity disturbance data at 5 km spacing (900 points). A contour map of the same data is presented in Fig. 6.4-3. There is a pronounced west-to-east trend from positive to negative values in the range 36 mgal to -25 mgal. The average value of the east disturbance is 1.03 mgal and the rms is 12.3 mgal. (This is equivalent to about 2.5 arc sec of deflection.)

6.5 RESULTS WITH SYNTHETIC LOCAL DATA

One test case was computed with truth data from the high-frequency local gravity data sets. No reference field

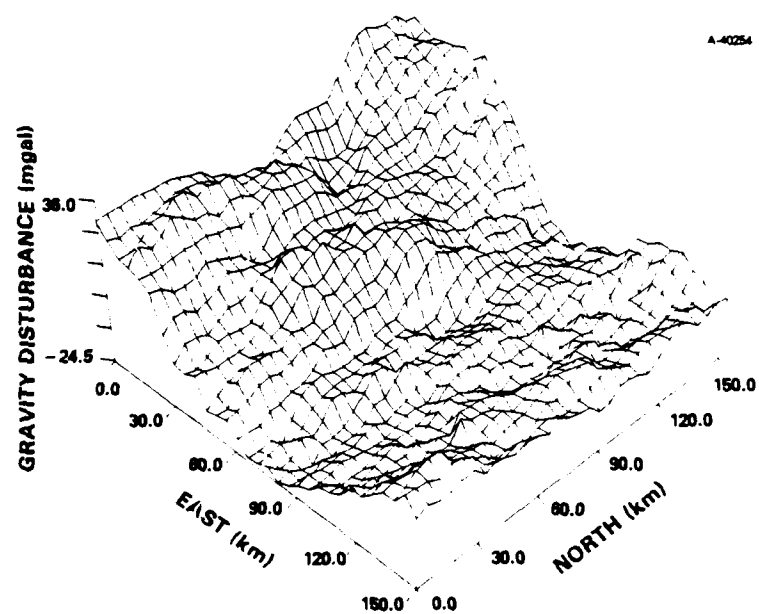


Figure 6.4-2 East Gravity Disturbance Surface Plot

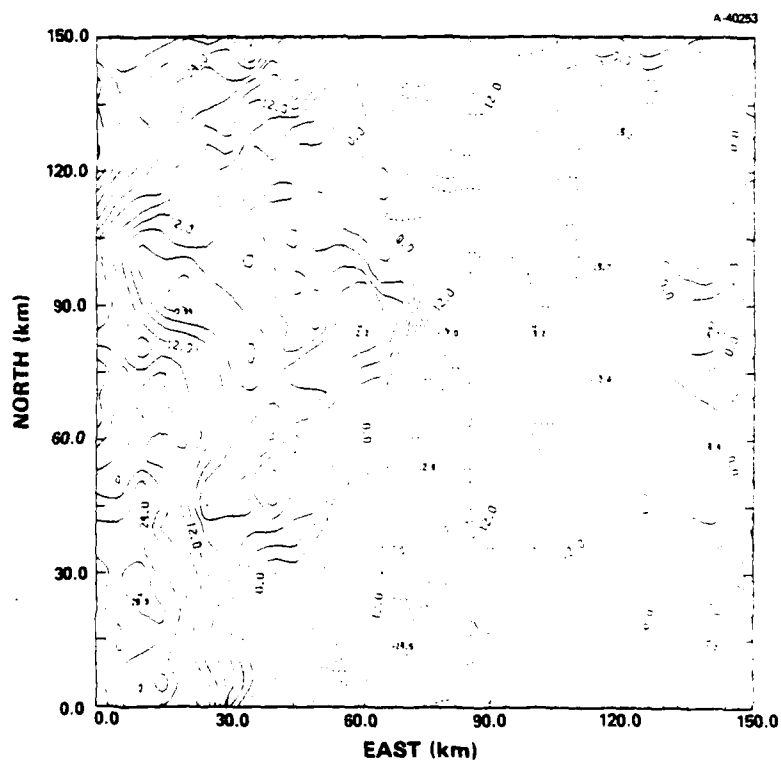


Figure 6.4-3 East Gravity Disturbance Contour Plot (mgal)

was removed from the data. The extent of the data was a 150 km square gridded at 5 km for a total of 900 points. The covariance model for the GEOFAST estimation was a single-shell AWN model with a correlation distance of 10 km. No measurement noise was included since this effect can be assessed analytically as in Section 6.3.3. The GEOFAST bandwidth parameter was chosen to be $m_B = 4$.

Estimation accuracy results for this case are displayed in Table 6.5-1 for successively smaller estimation regions within the dataset. There is a systematic negative bias of about 7 mgal which represents the low-frequency field not observable in such a small data set (150 km is less than 2 deg). This effect would be removed by first subtracting the mean or by a sufficiently high order reference field, as demonstrated in the previous section. The error standard deviation decreases monotonically toward the center of the data (from almost 9 mgal to less than 2 mgal). The accuracy near the center is 1.7 mgal or equivalently 0.35 arc sec of deflection. The rms east disturbance field in the same region is 9.5 mgal so that the rms

TABLE 6.5-1
GEOFAST ESTIMATION ACCURACY

ESTIMATION REGION SIZE (km) [*]	ESTIMATION ERROR (mgal)		
	MEAN	SIGMA	MAXIMUM
150	-6.9	8.8	39.7
120	-8.3	4.8	21.6
80	-9.5	2.8	16.4
40	-10.1	1.7	13.2

*Side length of central square within 150 km square of data.

estimation error is about 17 percent (assuming the mean to be compensated).

Figure 6.5-1 displays the estimation error for all 900 points. It can be seen that the error is mainly concentrated near the edges. This effect is common to all estimation results based on data of finite extent, and will be noticeable

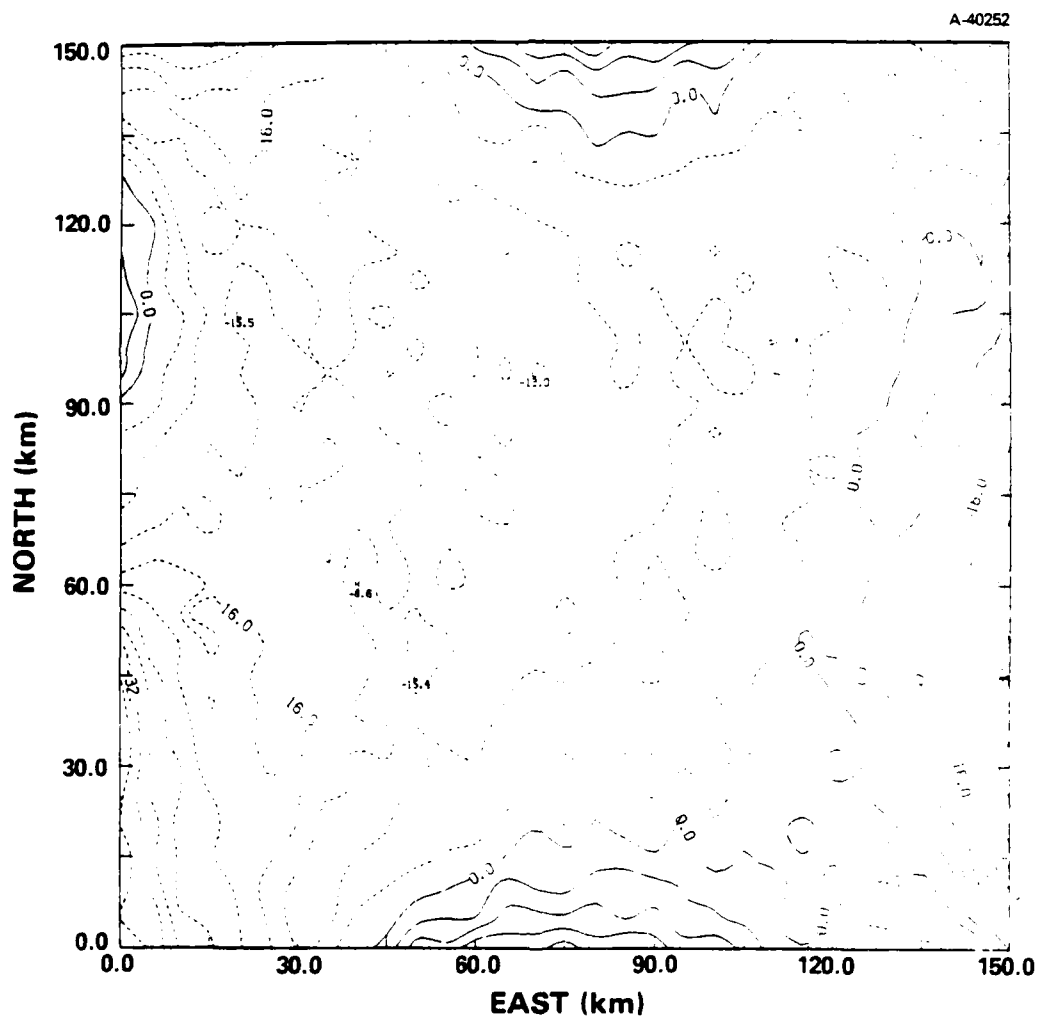


Figure 6.5-1 East Gravity Disturbance Estimation Error (mgal)

within 1 or 2 correlation distances from the edge. Removal of a high-order reference field would reduce this effect by reducing the correlation distance inherent in the data. In addition, some of the sharp central valleys in Fig. 6.4-2 have not been resolved precisely enough. For this data set a finer grid spacing would be expected to provide significant improvement here, by more precisely aligning estimated peaks with the truth data.

6.6 SUMMARY OF RESULTS

Numerical experiments were conducted with the GEOFAST algorithm using synthetic data from two different sources. The first data set was the Rapp 1981 spherical harmonic model evaluated through degree and order 180 for a marine trench area in the Pacific. This provides a moderately high frequency model in an active ocean gravity area.

Numerical experiments with the first data set demonstrate that GEOFAST is able to estimate deflections of the vertical from gravity anomalies to less than 0.2 arc sec rms error. This result is dependent on reducing the data by a high-order reference field (in this case the Rapp model to degree 90). With only a mean subtracted from the data, estimation accuracy is degraded to the order of 1.0 arc sec rms (a factor-of-five degradation).

The effect of measurement noise in anomaly data on deflection estimation accuracy was also studied. For white noise up to 5 mgal rms, total estimation errors were less than 0.3 arc sec rms.

The efficiency of the GEOFAST algorithm was demonstrated by quadrupling the number of datapoints, N , from 900 to 3600. The cost per calculation increased as predicted proportional to $N \log N$. In contrast, standard collocation approaches have a computer load proportional to N^3 . Another important feature of the GEOFAST algorithm that is also illustrated is the design tradeoff between computing cost and estimation accuracy (through a window bandwidth parameter). By this technique, a desired level of accuracy can be achieved for the minimum computer load. In the cases reported here, relaxing the accuracy requirement from 0.1 arc sec to 0.2 arc sec results in a reduction of computation time by a factor of 8.

The second source of synthetic data employed in these experiments is a high-frequency local gravity model at a resolution of 5 km in a moderately active area of the U.S. The GEOFAST algorithm was used with this data set to predict horizontal gravity disturbance from vertical gravity disturbance (equivalent to deflection prediction from anomalies). Results show that estimation accuracy better than 2 mgal rms (0.5 arc sec deflection) is attainable away from the edge of the data. This level of accuracy requires subtracting out a high-order reference field to eliminate wavelengths on the order of 100 km from the data. To obtain additional accuracy, this gravity field would need to be sampled at a higher rate than 5 km.

The results presented in this chapter demonstrate that the GEOFAST technique could be applied to current problems in reduction of gravity gradiometer or satellite altimeter data. In these applications, a large volume of gridded data is available and computer loading poses the major bottleneck. Accuracy and resolution requirements inherent in high-quality map production dictate a need to process the data without compression via averaging or parametric surface fitting. In this

context, the computer problem must be addressed directly, and the GEOFAST method is an example of such an approach. In contrast, the collocation approaches described in Refs. 20 and 21 and summarized in Chapter 3 were unable to utilize all of the available data observations. These approaches required averaging or subsampling the observations (see Table 3.3-2) before estimation.

7.

SUMMARY AND CONCLUSIONS

This report describes research on geodetic algorithms, with emphasis on the prediction of gravity anomalies and deflections of the vertical. Two general types of methods are considered:

- Classical integral formulas
- Modern statistical estimation (least-squares collocation).

The mathematical details of the major algorithms in each category are given in Appendix A.

The present work builds upon and complements work done by the IAG Special Study Group 3.90 on "Evaluation of Local Gravity Field Determination Methods." TASC was invited to participate in this Study Group because of our development of the GEOFAST algorithm. Recent work by the IAG Study Group (Refs. 20 and 21), which is based mainly on analysis of gravity anomaly, deflection of the vertical, and terrain height data from the White Sands, NM area, is summarized in Chapter 3. Chapter 4 of this report describes TASC's analyses of the topographic contribution to deflections of the vertical in the White Sands area. This report also includes a new derivation of the convolutional approximation to terrain corrections (Chapter 5 and Appendix B). Our tests of the GEOFAST algorithm using synthetic marine and local gravity data are described in Chapter 6.

This final chapter is divided into three sections. Section 7.1 is a summary of our key contributions, Section 7.2 reiterates the major conclusions, and Section 7.3 contains recommendations and suggestions for further research.

7.1 SUMMARY OF KEY CONTRIBUTIONS

The key contributions of TASC's research on geodetic algorithms are:

- Spectrum and cross-spectrum analyses of terrain and gravity anomaly profiles from the White Sands, NM test area (Chapter 4, Appendix C)
- Analysis of correlations between topography and observed deflections of the vertical in the White Sands area (Chapter 4, Appendix C)
- A new derivation for the convolution approach to terrain corrections showing that this approach is actually more accurate than had been claimed in the recent literature (Chapter 5, Appendix B)
- Detailed evaluation and quantification of the accuracy of the GEOFAST algorithm, based on synthetic marine and local gravity data (Chapter 6)
- A summary in consistent notation of the major geodetic algorithms (Appendix A)
- A compact summary of recent results by the IAG Special Study Group 3.90 (Chapter 3).

These contributions fall into the two general areas of: analysis of free-air gravity, deflections of the vertical, and topographic effects in the White Sands area; and detailed comparison and evaluation of geodetic algorithms including the GEOFAST algorithm.

7.2 CONCLUSIONS

The spectral analysis of free-air gravity and topographic effect profiles reflects the strongly anisotropic characteristics of the White Sands area. In particular, the data profiles were divided into four categories, based on geographic orientation of the profile segment (north-south or east-west) and type of terrain (mountain or plateau). The main conclusions from power spectrum and coherence analysis are:

- Plateau profile segments show consistently lower power for topographic effect than for free-air anomalies
- Mountain segments show higher power when the profile orientation is north-south
- East-west segments show local peaks in both coherence and power that are absent in the north-south segments
- Short wavelength coherence between topographic effect and free-air anomaly is high for east-west segments and low for north-south profile segments.

Deflections of the vertical in the White Sands are predicted from topography alone show a high correlation (80-90 percent) with observed (astrogeodetic) deflections, as illustrated by means of scatter diagrams. The predictions account for about 50 percent of the rms and 80 percent of the mean in the observed data. Results are not improved substantially by assuming isostatic compensation or different densities for mountain and plateau regions.

Numerical experiments with the GEOFAST algorithm show that:

- GEOFAST determines deflections of the vertical to within 0.2 arc sec rms from synthetic marine gravity data
- This accuracy degrades to 0.3 arc sec in the presence of 5 mgal (rms) noise, and to 1 arc sec if a global geopotential reference model is not used
- The predicted dependence of computation time on number of data points and on bandwidth is achieved in practice. A 3600-point data set is computed in 4 min with $m_B=0$ and in 30 min with $m_B=4$.
- An accuracy of 0.5 arc sec rms is achieved with the synthetic local gravity data set (5 km sample spacing) if a reference field including wavelengths longer than 100 km is removed.

Each of the four algorithms applied to predict deflections of the vertical in the White Sands area, as described in the 1985 Report (Ref. 21), is capable of approximately 1 arc sec (rms) accuracy in both components. Despite the demonstrated generality and flexibility of least-squares collocation, algorithms based on classical integral formulas remain viable, especially in combination with FFT implementations.

7.3 RECOMMENDATIONS AND SUGGESTIONS FOR FURTHER WORK

These are the principal findings and recommendations of this study:

- Algorithms based on both modern estimation (collocation) and classical integral formulations have important contemporary applications
- For a given application, the following considerations apply in selecting an appropriate algorithm:

- Where availability of error estimates is an important consideration, collocation methods should be used
 - When input data are of mixed types, collocation should be used
 - If statistical optimality of the estimates is an important consideration, collocation is indicated
 - When a large number of estimates are required, the FFT implementation of the classical integral formulas and the GEOFAST FFT implementation of collocation are expected to be the most efficient choices
 - For a small number of estimates, local collocation and non-FFT implementations of classical integral formulas are most efficient
- Since the achieved levels of accuracy for algorithms in the IAG Study reflect primarily data quality and availability, the ultimate accuracy capability of the algorithms must be evaluated using synthetic data that include a realistically broad spectrum of wavelengths
 - Algorithms should be applied to residual data with known terrain effects and global reference fields removed
 - Remove-and-restore techniques which incorporate the above removal, plus a later restoration of the terrain and global long wavelength effects, are essential to realize the full performance of both classical and modern geodetic algorithms.

Since available computer power is still a limitation on the accuracy and utility of geodetic algorithms in practice, we suggest consideration of the implementation and practical use of new computer architectures such as vector, parallel, and systolic processors.

APPENDIX A
GEODETIC ALGORITHMS

A.1 INTEGRAL EVALUATION METHODS

The purpose of this appendix is to review briefly the classical integral evaluation methods for determining the undulation of the geoid and the deflections of the vertical from gravity data. These methods include the original formulations of Stokes and Vening Meinesz as well as more recent developments and extensions. They are treated in the standard reference literature (Ref. 1, for example).

The classical formulations assume the availability of input quantities (measured gravity) on, or close to, the physical surface of the earth. Since the variables appearing in the classical solution are linearized small quantities which often correspond to the difference in shape and gravity field between the ellipsoid and the geoid, it is frequently necessary to reduce measured gravity to the geoid (free-air reduction) for comparison with normal gravity on the ellipsoid. The integral formula of Stokes relates the separation between geoid and ellipsoid at a point (the undulation N) to the gravity anomaly on the entire geoid:

$$N = \frac{R}{4\pi\gamma} \iint_{\sigma} \Delta g S(\psi) d\sigma \quad (\text{A.1-1})$$

where

R is an assumed mean radius for the earth
(usually taken as the radius of a sphere
having the same volume as the ellipsoid)

γ is an assumed mean value for gravity

σ represents the surface of a sphere approximating the ellipsoid

Δg is the free-air anomaly

ψ is the angular separation, on the surface of the sphere, between the point for which the solution is being computed and the element of integration, $d\sigma$

$S(\psi)$ is the Stokes function

The Stokes function, $S(\psi)$, can be expressed in the form:

$$S(\psi) = \sum_{n=2}^{\infty} \frac{2n+1}{n-1} P_n(\cos \psi) \quad (\text{A.1-2})$$

or in the equivalent finite form

$$S(\psi) = 1 + \operatorname{cosec} \left(\frac{\psi}{2} \right) - 6 \sin \left(\frac{\psi}{2} \right) - 5 \cos \psi \\ - 3 \cos \psi \ln \left[\sin \left(\frac{\psi}{2} \right) + \sin^2 \left(\frac{\psi}{2} \right) \right] \quad (\text{A.1-3})$$

Similarly, the Vening Meinesz formulas relate the north-south (ξ) and east-west (η) components of the deflection of the vertical at a point on the geoid to worldwide gravity anomalies:

$$\xi = \frac{1}{4\pi\gamma} \iint_{\sigma} \Delta g \left(\frac{dS}{d\psi} \right) \cos \alpha \, d\sigma \quad (\text{A.1-4})$$

$$\eta = \frac{1}{4\pi\gamma} \iint_{\sigma} \Delta g \left(\frac{dS}{d\psi} \right) \sin \alpha \, d\sigma \quad (\text{A.1-5})$$

where

$\frac{dS}{d\psi}$, the derivative of the Stokes function, is the Vening Meinesz function

α is the azimuth of the great-circle arc (of length ψ) joining the solution point and the element of integration, $d\sigma$

An explicit expression for the Vening Meinesz function, $\frac{dS}{d\psi}$, is given in Eq. A.1-6:

$$\begin{aligned} \frac{dS}{d\psi} = & - \frac{\cos(\frac{\psi}{2})}{2 \sin^2(\frac{\psi}{2})} + 8 \sin \psi - 6 \cos(\frac{\psi}{2}) - \frac{3[1 - \sin(\frac{\psi}{2})]}{\sin \psi} \\ & + 3 \sin \psi \ln[\sin(\frac{\psi}{2}) + \sin^2(\frac{\psi}{2})] \end{aligned} \quad (A.1-6)$$

Improvements in the accuracy of the basic Stokes and Vening Meinesz formulas have been achieved by modifications that take into account the effects of:

- Gravitational attraction of the mass of the atmosphere (Ref. 47)
- Local topography (Ref. 34)
- Integration over an ellipsoid instead of the assumed sphere (Ref. 48).

Despite these improvements, the strongest limitation in the use of these formulas is that they require, in principle, knowledge of gravity anomalies all over the earth in order to compute undulation or deflection at a particular location. Another

limitation is that the input gravity data must be reduced to the geoid, with the results also applying to this theoretical surface rather than to the actual surface of the earth. Thus, for example, a further correction for the curvature of the plumb line is required to relate the results of the Vening Meinesz computation to deflections actually measured at the surface of the earth.

Approaches to addressing these limitations will be reviewed below. These include the use of satellite-derived spherical harmonic data, in the form of geopotential spherical expansions, to replace or supplement actual gravity anomaly data in remote regions, and the so-called modern or nonclassical approach, introduced by Molodenskii, that uses data referred to the physical surface of the earth.

Modern (nonclassical) solution - Associated usually with the name of the Russian geodesist Molodenskii, the so-called modern solution to the problem of determining the shape of the earth (and hence the deflection of the vertical) from gravity measured on the surface departs from the classical approach in that the use of the geoid is dispensed with; the desired output quantities (such as height anomaly or deflection at the surface) as well as the input quantities (measured gravity) are referred to the physical surface of the earth. The modern solution was introduced in 1945 and has undergone considerable development and improvement since that time. An up-to-date reference source for the modern solution is Part D of Ref. 2, while earlier presentations are found in Ref. 3 and Chapter 8 of Ref. 1.

Molodenskii's original formula for the determination of the deflection of the vertical from worldwide gravity data takes the form (Ref. 1):

$$\xi = \frac{1}{4\pi\gamma} \iint_{\sigma} (\Delta g + G_1) \left(\frac{dS}{d\psi} \right) \cos \alpha \, d\sigma - \frac{\Delta g}{\gamma} \tan \beta_1 \quad (\text{A.1-7})$$

$$\eta = \frac{1}{4\pi\gamma} \iint_{\sigma} (\Delta g + G_1) \left(\frac{dS}{d\psi} \right) \sin \alpha \, d\sigma - \frac{\Delta g}{\gamma} \tan \beta_2 \quad (\text{A.1-8})$$

where the symbols have the same meaning as in the corresponding Eqs. A.1-4 and A.1-5, except as indicated in the discussion to follow.

The free-air anomaly Δg appearing in Eqs. A.1-7 and A.1-8 differs from the classical free-air anomaly (as used in Eqs. A.1-4 and A.1-5) in that it is an anomaly referred to ground level rather than to the geoid:

$$\Delta g = g_p - \gamma_Q \quad (\text{A.1-9})$$

where

g_p is actual gravity measured at a point P on the surface of the earth

γ_Q is normal gravity at a point Q, on the reference surface known as the telluroid (Ref. 1), corresponding to P.

Furthermore, the anomaly referred to ground level is modified by G_1 , which is a terrain (and local mass anomaly) correction term to account for the departure of the earth's physical surface from a surface of equal potential. This term is calculated by approximating an integral of the form:

$$G_1 = \frac{R^2}{2\pi} \iint_{\sigma} \frac{h-h_p}{\ell_o^3} \Delta g \, d\sigma \quad (\text{A.1-10})$$

which involves the terrain relief ($h-h_p$) between the point for which the correction is being determined, P, and other points in its vicinity; as well as the gravity anomaly Δg . In Eq. A.1-10, the chordal distance between the point P and the element of integration is ℓ_o ; the other symbols have been defined above. In theory, the integral in Eq. A.1-10 is extended over the entire sphere. Practical implementations, however, generally do not extend beyond 50 km from the computation point.

The second term in Eqs. A.1-7 and A.1-8 represents the effect of the slope, or tilt, of the terrain in the vicinity of the computation point, with β_1 representing the inclination of a north-south terrain profile with respect to horizontal, and β_2 representing the corresponding east-west inclination.

The Pellinen Version - A subsequent modification of the Molodenskii solution by Pellinen (Ref. 4) offers computational advantages as well as a simpler formulation. This is the formulation which is the basis for the present state of the art of gravimetric determination of deflections of the vertical using a deterministic (nonstatistical) approach.

Pellinen's formulas

$$\xi = \frac{1}{4\pi\gamma} \iint_{\sigma} (\Delta g)' \left(\frac{dS}{d\psi} \right) \cos \alpha \, d\sigma \quad (\text{A.1-11})$$

$$\eta = \frac{1}{4\pi\gamma} \iint_{\sigma} (\Delta g)' \left(\frac{dS}{d\psi} \right) \sin \alpha \, d\sigma \quad (\text{A.1-12})$$

have the same form as the formulas of Vening Meinesz (Eqs. A.1-4 and A.1-5), except for the use of the modified gravity anomaly, $(\Delta g)'$, in place of the classical gravity anomaly. This modified anomaly incorporates all effects of the topography and is computed as follows:

$$(\Delta g)' = \Delta g + C \quad (A.1-13)$$

where

Δg is the free-air anomaly referred to ground level (Eq. A.1-9)

C is the topographic correction term.

The correction term C is computed in theory by evaluating the integral

$$C = \frac{R^2}{2\pi} \iint_{\sigma} \frac{(h-h_P)(\Delta g - \Delta g_P)}{\ell^3} d\sigma \quad (A.1-14)$$

This resembles the Molodenskii terrain correction term, G_1 , as defined in Eq. A.1-10, except for the use of a relative gravity anomaly, $\Delta g - \Delta g_P$, referred to the anomaly at the computation point, P . In practice (as was pointed out in the discussion of Eq. A.1-10), the integral over the entire sphere appearing in Eq. A.1-14 is replaced by a summation limited to points in the immediate vicinity of P .

Numerical implementation - The practical numerical implementation of formulas like Eq. A.1-1 for the determination of undulation, or Eqs. A.1-11 and A.1-12 for the components of deflection, is based on the use of a finite sum to replace the integral. The principle will now be illustrated by a discussion

of the method for computing deflection of the vertical. In the Pellinen approach discussed above, there are two sets of integrals that must be evaluated numerically. At each gravity station a topographic correction term, C , is computed by approximating the integral of Eq. A.1-14, using gravity and terrain relief data in the vicinity of the gravity station. This is applied as an adjustment to the ground level free-air anomaly. With the gravity data thus adjusted, the integrals in Eqs. A.1-11 and A.1-12 are then evaluated by a second numerical procedure, in which the integral over the entire sphere is partitioned into five zones at increasing radial distances from the computation point. The representation and treatment of the gravity data, as well as the details of approximating the integral by a finite sum, vary from zone to zone, as summarized below.

The evaluation of both types of integrals enumerated above is usually done through the use of a circular template system of the type introduced by Rice (Ref. 5). In its original form, this system consisted of 57 concentric rings surrounding the computation point, the innermost ring beginning at a distance of 100 m from the center, and the outermost ring ending at a distance of 1094.3 km from the center (see Table I of Ref. 5). Note that because of the singularity of the Vening Meinesz function when ψ , the angular separation, approaches zero, a special treatment was used to incorporate the effect of gravity stations within 100 m (see the discussion of the innermost zone below); and, in his original treatment, Rice did not account for the effects of anomalies beyond 1094.3 km, accepting the contribution of the distant zone as an error source. The system of rings is further divided into zones by a set of radial lines projecting from the center at an angular separation of 10 deg. There are, then, a total of 2052 zones (excluding the innermost zone) in the Rice template system.

The key point in this system is the choice of the radii of the circles bounding the various rings. These radii are chosen (based on the variation of the Vening Meinesz function with distance from the center) so that each zone contributes the same amount of deflection at the center for a given mean value of gravity anomaly over the zone. In particular, each Rice zone contributes 0.001 arc sec of radial deflection if the mean gravity anomaly for the zone is 1.0 mgal.

With the use of this template system, the numerical evaluation of an integral reduces to two simple steps:

- The determination of a mean (or other representative) value of the gravity anomaly within each zone
- The summation of the contributions from all of the zones.

For the evaluation of the topographic correction term (Eq. A.1-14), a template system is devised in Ref. 6 that consists of 90 zones, having the characteristics summarized in Table A.1-1 (Ref. 6).

Evaluation of the topographic correction term, using this template system, is a two-stage process:

- Determine suitable mean values, within each zone, of
 - gravity anomaly difference
 - terrain height difference
- Compute a weighted sum of the individual zone contributions.

Reference 6 recommends a uniform application of the topographic correction computation to each gravity station in the point

TABLE A.1-1
TEMPLATE SYSTEM FOR TOPOGRAPHIC CORRECTION

RING NUMBER (Note 1)	CONTRIBUTION TO TOPOGRAPHIC CORRECTION (mgal) (Note 2)	INNER RADIUS (km)	OUTER RADIUS (km)	NUMBER OF ZONES
2	7.5×10^{-5}	0.100	0.137	6
3	7.5×10^{-5}	0.137	0.217	6
4	7.5×10^{-5}	0.217	0.526	6
5	1.5×10^{-5}	0.526	0.734	9
6	1.5×10^{-5}	0.734	1.218	9
7	1.5×10^{-5}	1.218	3.556	9
8	4.0×10^{-6}	3.556	7.287	9
9	1.0×10^{-6}	7.287	9.878	12
10	1.0×10^{-6}	9.878	15.330	12
11	1.0×10^{-6}	15.330	34.210	12

Note 1: The effects of Ring 1 (points within 100 m) require special treatment because of the divergence of the integral

Note 2: This is the contribution to the correction term from a zone for which the mean height difference is 100 m and the mean gravity anomaly difference is 1 mgal.

gravity anomaly data base. In Ref. 7, on the other hand, the correction is applied much more selectively (with due regard to computational resources) at points where, based on the nature of the surrounding terrain and the amount of short-wavelength energy in the gravity anomaly field, the topographic correction is expected, a priori, to be significant.

THE ANALYTIC SCIENCES CORPORATION

The first step in the evaluation of the integral formulas of Eqs. A.1-11 and A.1-12 is the partitioning of the domain of integration into five zones:

- Innermost - within 100 m of the computation point
- Inner - a 3-deg square centered on the one-deg square containing the computation point
- Near - the 15-deg square centered on the 5-deg square containing the computation point
- Middle - the 45-deg square centered on (but excluding) the near zone
- Outer - the rest of the earth's surface, beyond the middle zone.

Within each of the zones, the contribution to the integral is evaluated as outlined below.

Innermost Zone - A special treatment is required for the innermost zone, which must be excluded from the domain of integration in Eqs. A.1-11 and A.1-12 to avoid divergence of the integral, since the Vening Meinesz function behaves asymptotically as

$$\frac{dS}{d\psi} \sim -\frac{2}{\psi^2} \quad (\text{A.1-15})$$

as ψ approaches zero. Within this innermost zone there must be sufficient gravity data to permit an estimate of the north-south and east-west components of the horizontal gradient of the gravity anomaly. The traditional approach (Ref. 5) is to use a square mesh of 8 points arranged symmetrically within the innermost zone for the gradient estimation. Quite clearly,

the use of gradiometer data, if available, would be particularly appropriate in this application. The innermost zone contributions are then:

$$\xi_{IM} = - \frac{1}{2\gamma} (\text{grad } \Delta g)_{NS} r_{IM} \quad (A.1-16)$$

$$\eta_{IM} = - \frac{1}{2\gamma} (\text{grad } \Delta g)_{EW} r_{IM} \quad (A.1-17)$$

where

γ is normal gravity at the computation point

r_{IM} is the radius of the innermost zone (typically, r_{IM} is 100 m)

$(\text{grad } \Delta g)_{NS}$ is the north-south component of the horizontal gradient of the gravity anomaly

$(\text{grad } \Delta g)_{EW}$ is the east-west component of the horizontal gradient of the gravity anomaly

Inner Zone - Within the inner zone, a circular template system based on the concept of Rice rings is employed to organize the computations. The smallest of the 21 rings begins at a distance of 100 m from the computation point, while the outermost ring ends at a distance of 128.6 km. Since the rings are subdivided uniformly by radial lines separated by 10 deg, the total number of compartments is 756. The radii defining the rings are chosen so that any compartment will contribute 0.002 arc sec of radial deflection if the modified gravity anomaly within that compartment has a uniform value of 1 mgal.

The computational procedure for the inner zone consists of these stages:

- Sorting the point gravity anomalies into the appropriate compartments
- Using interpolation procedures to compute a best estimate of the gravity anomaly at the center of each compartment
- Summing the contributions from all of the compartments.

Beyond the inner zone, the gravity data are used in the form of mean gravity anomalies defined for square compartments. The contribution from the area of overlap between the inner-zone ring template and the block pattern of the near zone, known as the transition area, is evaluated by an elaborate special procedure (Refs. 6 and 7) to ensure that no area is omitted and no contribution is duplicated.

Near Zone - Within the near zone, the gravity field is represented by 0.5-deg mean gravity anomalies; the integrals (Eqs. A.1-11 and A.1-12) reduce to simple sums over the individual blocks, with the kernel function

$$K = \left(\frac{dS}{d\psi} \right) \cos \alpha \quad (\text{A.1-18})$$

or

$$K = \left(\frac{dS}{d\psi} \right) \sin \alpha \quad (\text{A.1-19})$$

evaluated at the center of the block.

Middle and Outer Zones - Mean gravity anomalies defined for one-deg squares are used for the middle zone; five-deg mean gravity anomalies are used in the outer zone. The evaluation of the contribution of each individual block is essentially as described for the near zone.

Summary - The salient features of the evaluation procedure described above, which is presented in detail in Refs. 6 and 7, are summarized in Table A.1-2, which reviews the type of data and the computational method used within each of the zones.

Use of spherical harmonic expansions - Although the integral formulas for undulation and deflection nominally require a knowledge of point gravity anomaly values over the entire globe, it is clear that the contribution from zones distant from the point of computation comes only from the long-wavelength content of the gravity field. In this approach,

TABLE A.1-2
OVERVIEW OF THE EVALUATION OF THE
PELLINEN INTEGRAL FORMULA

ZONE	DATA USED	COMPUTATIONAL METHOD
Innermost	Point gravity anomalies (note possibility of using gradiometer data)	Eqs. A.1-16 and A.1-17
Inner	Point gravity anomalies, terrain height data	Circular template system (Rice rings)
Near	0.5-deg mean gravity anomalies	Summation over indi- vidual blocks
Middle	1-deg mean gravity anomalies	Summation over indi- vidual blocks
Outer	5-deg mean gravity anomalies	Summation over indi- vidual blocks

detailed gravity anomaly data are used only within an annular cap of radius ψ_0 centered on the point of computation. For the computation of the undulation, for example, the following approach (Ref. 8) is representative:

The input data are the measured surface gravity anomalies Δg within the annular cap of radius ψ_0 , and the computed gravity anomalies Δg_s outside of this region. The computed anomaly is expressed in terms of the spherical harmonic expansion of the geopotential in the form

$$\Delta g_s = \frac{GM}{R^2} \sum_{n=2}^{\infty} (n-1) \left(\frac{a}{R}\right)^n \sum_{m=0}^n (C'_{nm} \cos m\lambda + S_{nm} \sin m\lambda) P_{nm}(\sin \phi) \quad (A.1-20)$$

where

- GM is the geocentric gravitational constant
- R is the distance of the computation point from the earth's center
- a is the earth's equatorial radius
- ϕ and λ are geocentric latitude and longitude of the computation point
- P_{nm} is the associated Legendre function of degree n and order m

In Eq. A.1-20, S_{nm} and C'_{nm} are the spherical harmonic coefficients of the geopotential, with the prime signifying that the C_{nm} coefficients have been adjusted to remove the effect of the normal gravity field associated with the reference ellipsoid.

The undulation N is then expressed exactly in the form

$$N = N_1 + N_2 + N_3 \quad (\text{A.1-21})$$

where N_1 is the undulation that would be computed from spherical harmonic data only; N_2 and N_3 represent the contribution to the undulation of $\Delta g - \Delta g_s$ in the annular cap and the rest of the earth, respectively. The contribution N_1 is written explicitly as

$$N_1 = \frac{GM}{R\gamma} \sum_{n=2}^{\infty} \left(\frac{a}{R}\right)^n \sum_{m=0}^n (C'_{nm} \cos m\lambda + S_{nm} \sin m\lambda) P_{nm}(\sin \phi) \quad (\text{A.1-22})$$

where γ is normal gravity at the computation point. The annular cap contribution has the same form as Eq. A.1-1:

$$N_2 = \frac{R}{4\pi\gamma} \iint_{\sigma} (\Delta g - \Delta g_s) S(\psi) d\sigma \quad (\text{A.1-23})$$

except that the adjusted anomaly $(\Delta g - \Delta g_s)$ is used and the integration extends only over the annular cap. Finally, the utility of this approach depends on choosing the radius of the annular cap so that the contribution of N_3 can be neglected. Hence, the formula used in practice is

$$N = N_1 + N_2 \quad (\text{A.1-24})$$

The error contributed by neglecting N_3 can be reduced by modifying the Stokes kernel $S(\psi)$, as discussed, for example, in Refs. 9 and 10.

A.2 LEAST-SQUARES COLLOCATION

Least-squares collocation is a modern technique for estimating geodetic quantities from observed data. It has several advantages over classical integral formulas:

- Collocation allows a mix of different types of quantities in the input data and different types may likewise be estimated. For example, the classical Vening Meinesz integral permits computation of deflections of the vertical from measured gravity anomalies. However, least-squares collocation may use observations of anomalies and other quantities, such as astrogeodetic deflections or gravity gradients, to estimate simultaneously deflections and additional quantities, such as undulation of the geoid.
- No special processing is required for irregularly-spaced observation or estimation points.
- The effects of errors in the input data, including lack of independence, are easily included. Also, with very modest extra computation, the variances and covariances of the estimated quantities may be determined.
- In its most general form, collocation includes the estimation of parameters governing systematic variations in the data, such as terms pertaining to the normal potential and reference system or the density used for terrain corrections.

However, least-squares collocation has its disadvantages, too:

- It requires the inversion of a square matrix with dimension equal to the number of data values. This limits the speed

of the algorithm and the number of data that may be processed.

- A model must be provided, which is usually assumed to be stationary and isotropic, for the covariance of the anomalous potential. (From such a model other covariances and cross-covariances are derived.)

This appendix is organized into five subsections, as follows. Appendix A.2.1 briefly outlines the development and background of least-squares collocation. Appendix A.2.2 describes the least-squares interpolation of gravity anomalies, which is a special case of collocation. It covers much of the mathematical development essential to collocation. The covariance and cross-covariance of geodetic quantities of different types are covered in Appendix A.2.3, in terms of linear operators applied to the covariance of the anomalous potential. In Appendix A.2.4, least-squares interpolation is generalized to least-squares collocation involving quantities of mixed type by combining the results of the preceding two sections. A final generalization, to include the simultaneous estimation of linear parameters, is mentioned briefly. Appendix A.2.5 concludes with a discussion of the practical application of collocation.

A.2.1 Background

Least-squares collocation was introduced in geodesy in the late 1960s by Krarup (Ref. 11) and Moritz (Refs. 12 and 13). It is a generalization of least-squares interpolation to include an arbitrary mix of types of geodetic quantities and the simultaneous linear estimation of parameters governing systematic behavior of the field. Heiskanen and Moritz (Ref. 1, pp. 267-270) discuss least-squares prediction of gravity anomalies (using the term prediction to encompass both interpolation

and extrapolation), although their derivation is limited to error-free data. The more general derivation given in the following subsection includes the effects of measurement errors in the data. Independently, Gentry and Nash (Ref. 14) developed an optimal algorithm for the estimation of deflections of the vertical from gravimetry. Like least-squares interpolation, it is a special case of collocation. Tscherning (Ref. 15) published a general computer program (GEOCOL) for least-squares collocation and has updated it frequently ever since. Tait (Ref. 16; see also Appendix A.3 and Chapter 6 of this report) describes a fast Fourier-domain implementation of collocation for application to points on a regular grid.

A fairly recent and very thorough discussion of the fundamentals and theory of collocation is given by Moritz (Ref. 2); his review paper (Ref. 17) provides a more compact summary. Published accounts of various applications of collocation are abundant (e.g., Refs. 18, 19, 20, 21).

A remark about the term "least-squares collocation" itself may be helpful. "Least-squares" emphasizes the statistical nature of the algorithm, but "collocation" by itself generally refers to a strictly deterministic technique used in the numerical solution of inhomogeneous differential equations (Ref. 22). In such equations, a differential operator L applied to an unknown function u equals a forcing function f .

$$Lu = f \qquad (A.2-1)$$

The strategy of collocation is to obtain a numerical approximation to the solution u , in terms of a linear combination of basis functions, that minimizes $||Lu-f||$ where the norm $|| \ ||$ depends on the values of Lu and f only at a set of discrete points, rather than over a continuous interval. Such a norm

has obvious advantages in terms of numerical computation. In spite of major differences, there are parallels between this collocation technique and least-squares collocation. Geodetic quantities are known only at discrete points and "least-squares" implies minimization of a particular norm involving values only at those points. Furthermore, collocation may be viewed as primarily an attempt to estimate the anomalous potential, from which all other quantities may be derived. In this light, the anomalous potential is the analogy of the function u ; the observations are analogous to the values of f on the discrete point set, which should equal linear functionals of the anomalous potential, i.e., the analogs of Lu evaluated at the discrete points.

A.2.2 Least-Squares Interpolation

Least-squares interpolation is a special case of least-squares collocation in which only a single type of quantity is involved and parameter adjustment is not included. Here it is assumed, to be concrete, that gravity anomaly observations are to be interpolated. Only the covariance function for gravity anomalies is needed, but otherwise, the mathematical development proceeds just as in least-squares collocation (without parameter adjustment).

Least-squares interpolation and collocation employ the statistical concepts of expectation and covariance. The gravity-anomaly covariance function, a function of two points P and Q , is defined by

$$C(P,Q) = E \{ \Delta g_P \Delta g_Q \} \quad (A.2-2)$$

where $E\{ \}$ is the expected value operator. Frequently, it is assumed that the covariance function is stationary and isotropic

with respect to the horizontal coordinates, which means that the horizontal coordinates of P and Q enter into $C(P,Q)$ only through the horizontal distance between P and Q. On a global scale this is the spherical distance ψ defined in Fig. A.2-1 for two points on the unit sphere, where θ and λ denote colatitude and longitude, respectively. According to a basic relation in spherical trigonometry,

$$\cos \psi = \cos \theta \cos \theta' + \sin \theta \sin \theta' \cos(\lambda - \lambda') \quad (\text{A.2-3})$$

If the covariance function is stationary and isotropic, and if r denotes radial distance from the center of the earth, then

$$\begin{aligned} C(P,Q) &= \text{average of } \Delta g(r,\theta,\lambda) \Delta g(r',\theta',\lambda') \text{ over} \\ &\quad \text{all pairs of points such that } r = r_P, \\ &\quad r' = r_Q, \text{ and } \psi = \psi_{PQ} \\ &= C(r_P, r_Q, \psi_{PQ}) \end{aligned} \quad (\text{A.2-4})$$

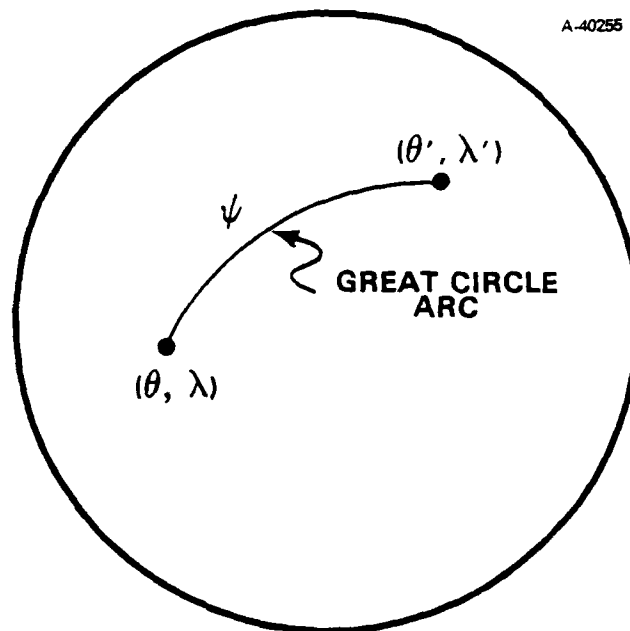


Figure A.2-1 Spherical Distance

The gravity-anomaly covariance function is also defined on a local scale. In the stationary isotropic case it depends on the Euclidean horizontal distance

$$s = \sqrt{(x-x')^2 + (y-y')^2} \quad (\text{A.2-5})$$

where x and y denote horizontal Cartesian coordinates. Letting z denote the elevation

$$C(P,Q) = C(z_P, z_Q, s_{PQ}) \quad (\text{A.2-6})$$

Now consider observations of the gravity anomaly at the points Q_1, Q_2, \dots, Q_n . The spatial distribution of the observation points is unimportant and may be quite irregular. Each observation ℓ will consist of the true gravity anomaly Δg plus a measurement error n . At the point Q_i ,

$$\ell_i = \Delta g_i + n_i \quad (\text{A.2-7})$$

Given the covariance function of the gravity anomaly and a covariance matrix for the measurement errors, the remainder of this section demonstrates how to:

- Find the optimal estimate of Δg at the point P
- Determine the variance of the estimate
- Determine the covariance of estimates of Δg at points P_1, P_2, \dots, P_m .

The estimate of Δg at P , $\Delta \hat{g}_P$, is assumed to be a linear combination of the observations

$$\Delta \hat{g}_P = \sum_{i=1}^n a_i \ell_i \quad (\text{A.2-8})$$

AD-A172 481

TOPICS IN GEODETIC ALGORITHM RESEARCH(U) ANALYTIC
SCIENCES CORP READING RM R P COWEN ET AL. 15 AUG 86
TASC-TR-5186-1 NS0014-85-C-0134

2/2

UNCLASSIFIED

F/G 8/5

NE

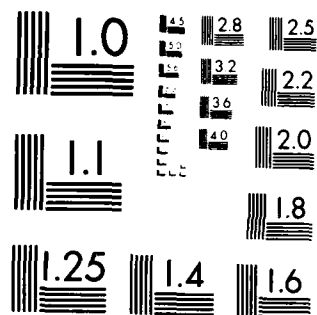
END

DATA

FILMED

11 86

DTIC



XEROCOPY RESOLUTION TEST CHART
NATIONAL BUREAU OF STANDARDS 1963-A

The error in this estimate is defined as

$$e_p = \Delta g_p - \Delta \hat{g}_p \quad (A.2-9)$$

where Δg_p is the true value of the gravity anomaly at P. The optimal estimate $\Delta \hat{g}_p$ is obtained by choosing the coefficients a_1, a_2, \dots, a_n to minimize the expectation of the squared error

$$\begin{aligned} E\{e_p^2\} &= E\{\Delta g_p^2 - 2\Delta g_p \sum_{i=1}^n a_i \ell_i + \sum_{i=1}^n \sum_{j=1}^n a_i a_j \ell_i \ell_j\} \\ &= C_{pp} - 2 \sum_{i=1}^n a_i C_{pi} + \sum_{i=1}^n \sum_{j=1}^n a_i a_j \bar{C}_{ij} \end{aligned} \quad (A.2-10)$$

where

$$C_{pp} = E\{\Delta g_p^2\} \quad (A.2-11)$$

$$C_{pi} = E\{\Delta g_p \ell_i\} = E\{\Delta g_p \Delta g_i\} + E\{\Delta g_p n_i\} \quad (A.2-12)$$

$$\begin{aligned} \bar{C}_{ij} &= E\{\ell_i \ell_j\} = E\{\Delta g_i \Delta g_j\} + E\{\Delta g_i n_j\} \\ &\quad + E\{\Delta g_j n_i\} + E\{n_i n_j\} \end{aligned} \quad (A.2-13)$$

Defining the measurement error covariance as

$$E\{n_i n_j\} = D_{ij} \quad (A.2-14)$$

(which is a diagonal matrix if the measurement errors are uncorrelated) and assuming that the true values and measurement errors are independent,

$$C_{PP} = C(P, P) \quad (A.2-15)$$

$$C_{Pi} = C(P, Q_i) \quad (A.2-16)$$

$$\bar{C}_{ij} = C_{ij} + D_{ij} \quad (A.2-17)$$

where

$$C_{ij} = C(Q_i, Q_j) \quad (A.2-18)$$

Now, for $i = 1, 2, \dots, n$, the derivative of $E\{e_p^2\}$ with respect to a_i is set to zero, yielding

$$\sum_{j=1}^n \bar{C}_{ij} a_j = C_{Pi} \quad i=1, 2, \dots, n \quad (A.2-19)$$

The solution of the linear system in Eq. A.2-19 may be substituted back into Eq. A.2-8 to yield the optimal estimate $\Delta \hat{g}_p$ and into Eq. A.2-10 to determine the variance, completing two of the three tasks listed earlier. These results are best expressed explicitly in matrix notation, which is also helpful in performing the third task -- determining the covariance of multiple estimates of Δg .

The vector

$$\underline{\ell} = \begin{pmatrix} \ell_1 \\ \ell_2 \\ \cdot \\ \cdot \\ \ell_n \end{pmatrix} \quad (\text{A.2-20})$$

and matrices

$$A = (a_1 \ a_2 \ \dots \ a_n) \quad (\text{A.2-21})$$

$$C_{P\ell} = (C_{P1} \ C_{P2} \ \dots \ C_{Pn}) = E\{\Delta g_{P\ell}^T\} \quad (\text{A.2-22})$$

and

$$\bar{C}_{\ell\ell} = \{\bar{C}_{ij}\} = E\{\underline{\ell} \ \underline{\ell}^T\} \quad (\text{A.2-23})$$

are needed. Note that A and $C_{P\ell}$ are 1 by n row vectors. In the case of simultaneous estimation at m different locations, they generalize to m by n matrices. Equations A.2-8, A.2-10, and A.2-19 are equivalent to

$$\Delta \hat{g}_P = A \underline{\ell} \quad (\text{A.2-24})$$

$$E\{e_P^2\} = C_{PP} - 2AC_{P\ell}^T + A\bar{C}_{\ell\ell}A^T \quad (\text{A.2-25})$$

and

$$\bar{C}_{\ell\ell}A^T = C_{P\ell}^T \quad (\text{A.2-26})$$

respectively.

Substitution of the formal solution of Eq. A.2-26

$$A = C_{P\ell} \bar{C}_{\ell\ell}^{-1} \quad (A.2-27)$$

into Eqs. A.2-24 and A.2-25 yields the optimal estimate

$$\Delta \hat{g}_P = C_{P\ell} \bar{C}_{\ell\ell}^{-1} \underline{\ell} \quad (A.2-28)$$

and its variance

$$E\{e_P^2\} = C_{PP} - C_{P\ell} \bar{C}_{\ell\ell}^{-1} C_{P\ell}^T \quad (A.2-29)$$

When gravity anomalies are interpolated at multiple points P_1, P_2, \dots, P_m , the optimal estimate and variance of each point are still given by Eqs. A.2-28 and A.2-29, but in addition, the covariance between errors in prediction at different points can be computed. Defining the vector of estimated gravity anomalies as

$$\underline{\hat{s}} = \begin{pmatrix} \Delta \hat{g} \text{ at } P_1 \\ \Delta \hat{g} \text{ at } P_2 \\ \vdots \\ \Delta \hat{g} \text{ at } P_m \end{pmatrix} \quad (A.2-30)$$

and applying Eq. A.2-28 to each point yields

$$\underline{\hat{s}} = C_{s\ell} \bar{C}_{\ell\ell}^{-1} \underline{\ell} \quad (A.2-31)$$

where C_{sl} is an m by n matrix defined by

$$C_{sl} = \{C(P_i, Q_i)\} = E\{\hat{s} \underline{l}^T\} \quad (A.2-32)$$

In terms of \hat{s} and the vector of true gravity anomalies,

$$\underline{s} = \begin{pmatrix} \Delta g \text{ at } P_1 \\ \Delta g \text{ at } P_2 \\ \vdots \\ \Delta g \text{ at } P_m \end{pmatrix} \quad (A.2-33)$$

the vector of errors at each point P_1, P_2, \dots, P_m is

$$\begin{aligned} \underline{e} &= \underline{s} - \hat{s} \\ &= \underline{s} - C_{sl} \bar{C}_{ll}^{-1} \underline{l} \end{aligned} \quad (A.2-34)$$

The m by m covariance matrix of errors in the estimated anomalies is simply the expected value of $\underline{e} \underline{e}^T$. This may be expanded as

$$\begin{aligned} E\{\underline{e} \underline{e}^T\} &= E\{\underline{s} \underline{s}^T\} - E\{\underline{s} \underline{l}^T\} \bar{C}_{ll}^{-1} C_{sl}^T \\ &\quad - C_{sl} \bar{C}_{ll}^{-1} E\{\underline{l} \underline{s}^T\} \\ &\quad + C_{sl} \bar{C}_{ll}^{-1} E\{\underline{l} \underline{l}^T\} \bar{C}_{ll}^{-1} C_{sl}^T \end{aligned} \quad (A.2-35)$$

Defining

$$C_{ss} = E\{\underline{s} \underline{s}^T\} = \{C(P_i, P_j)\} \quad (A.2-36)$$

recalling Eq. A.2-23 and Eq. A.2-32, and noting that

$$E\{\underline{l} \underline{s}^T\} = C_{sl}^T \quad (A.2-37)$$

yields the final result

$$E\{\underline{e} \underline{e}^T\} = C_{ss} - C_{sl} \tilde{C}_{ll}^{-1} C_{sl}^T \quad (A.2-38)$$

Note that the diagonal terms of Eq. A.2-38 are the variances of the estimates of each point and are equivalent to Eq. A.2-29, while the off-diagonal terms are covariances between estimates at different points.

A.2.3 Covariance Functions

In generalizing least-squares interpolation to least-squares collocation it is necessary to determine the covariances and cross-covariances of quantities of different types (e.g., the cross-covariance between north deflection of the vertical ξ and gravity anomaly Δg). $K(P, Q)$, the covariance function of the anomalous potential T , is central to this process; its use guarantees a consistent set of covariances and cross-covariances. In analogy to Eq. A.2-2,

$$K(P, Q) = E\{T_P T_Q\} \quad (A.2-39)$$

The purpose of this section is to explain the derivation of additional covariances from $K(P,Q)$ and to present some examples of stationary isotropic models for $K(P,Q)$.

Observable quantities such as gravity anomaly, geoid undulation, deflection of the vertical, and components of the gravity gradient depend on the anomalous potential through linear operators. For example, the relation (Ref. 1)

$$\Delta g = - \frac{\partial T}{\partial r} - \frac{2}{r} T \quad (\text{A.2-40})$$

may be expressed as

$$\Delta g = L^{\Delta g} T$$

where the notation $L^{\Delta g}$ denotes the linear operator:

$$L^{\Delta g} = - \frac{\partial}{\partial r} - \frac{2}{r} \quad (\text{A.2-41})$$

Evaluation at a specific point P may be denoted by adding a subscript to the operator, e.g.,

$$\Delta g_P = L_P^{\Delta g} T = \left(- \frac{\partial}{\partial r} - \frac{2}{r} \right) T(r, \theta, \lambda) \Bigg|_{\substack{r=r_P \\ \theta=\theta_P \\ \lambda=\lambda_P}} \quad (\text{A.2-42})$$

Geodetic quantities and their corresponding operators are summarized in Table A.2-1. (γ_0 denotes normal gravity.)

TABLE A.2-1
GEODETIC QUANTITIES AND LINEAR OPERATORS

QUANTITY	SYMBOL	OPERATOR
Anomalous Potential	T	1 (the identity)
Gravity Anomaly	Δg	$-\frac{\partial}{\partial r} - \frac{2}{r}$
Geoid Undulation	N	$1/\gamma_0$
Deflection of the Vertical	north ξ	$\frac{1}{\gamma_0 R} \frac{\partial}{\partial \theta}$
	east η	$-\frac{1}{\gamma_0 r \sin \theta} \frac{\partial}{\partial \lambda}$
Gradient Components	--	$\partial^2/\partial r^2$, etc

The operators in Table A.2-1, which yield geodetic quantities when applied to the anomalous potential, may be applied in pairs to the covariance function of the anomalous potential to yield covariances and cross-covariances as needed. This fundamental observation may be demonstrated with an example. Consider the cross-covariance between the gravity anomaly Δg at point P and the deflection of the vertical ξ at point Q,

$$E\{\Delta g_P \xi_Q\} = E\{(L_P^{\Delta g} T)(L_Q^{\xi} T)\} \quad (\text{A.2-43})$$

The expectation operator is linear (it is a kind of average), so the linear operators $L_P^{\Delta g}$ and L_Q^{ξ} may be moved to the left. Then, from the definition of $K(P, Q)$ (Eq. A.2-39),

$$E\{\Delta g_P \xi_Q\} = L_P^{\Delta g} L_Q^{\xi} K \quad (A.2-44)$$

where $L_P^{\Delta g}$ operates on K as a function of the coordinates of P and L_Q^{ξ} operates on K as a function of the coordinates of Q . For example, the above cross-covariance is written out as

$$L_P^{\Delta g} L_Q^{\xi} K = \left(-\frac{\partial}{\partial r} - \frac{2}{r} \right) \left(\frac{1}{r_0} \frac{\partial}{\partial \theta'} \right) K(r, \theta, \lambda, r', \theta', \lambda') \Big|_{\substack{r=r_P, \theta=\theta_P, \lambda=\lambda_P \\ r'=r_Q, \theta'=\theta_Q, \lambda'=\lambda_Q}} \quad (A.2-45)$$

Another example is the relation between the gravity anomaly covariance function (Eq. A.2-2) and the covariance of the anomalous potential,

$$C(P, Q) = L_P^{\Delta g} L_Q^{\Delta g} K \quad (A.2-46)$$

In practice, $K(P, Q)$ is usually approximated by a parametric model. The definition of $K(P, Q)$, Eq. A.2-39), imposes some constraints on such models.

$$K(P, Q) = E\{T_P T_Q\} = E\{T_Q T_P\} = K(Q, P) \quad (A.2-47)$$

so the covariance function must be symmetric in its dependence on the coordinates of P and Q . Also, the harmonicity of T (it satisfies Laplace's equation outside the earth) implies that K must be harmonic in both the coordinates of P and the coordinates of Q . Parametric models for K are almost always taken to be stationary and isotropic, and in addition, they must be positive semi-definite to ensure positive semi-definite covariance matrices.

All global covariance functions of the form

$$K(P,Q) = \sum_{n=0}^{\infty} k_n \left(\frac{R}{r_P r_Q} \right)^{n+1} P_n (\cos \psi) \quad (A.2-48)$$

where

R is the radius of the earth,

P_n is the Legendre polynomial of degree n ,

$\cos \psi$ is given by Eq. A.2-3) with θ_P , λ_P , θ_Q , and λ_Q substituted for $\theta, \lambda, \theta', \lambda'$,

are stationary and isotropic, because the horizontal coordinates enter in only through the distance ψ . In addition they are harmonic, because, for all non-negative n ,

$$\left(\frac{R}{r_P r_Q} \right)^{n+1} P_n (\cos \psi)$$

satisfies Laplace's equation in the coordinates of both P and Q , and the symmetry between P and Q is evident. Such covariance functions are positive semi-definite if and only if

$$k_n \geq 0 \quad (A.2-49)$$

Two examples of covariance functions in this form are the Tscherning and Rapp model (Ref. 23) in which

$$k_n = \frac{AR^2 S^{n+1}}{(n-1)(n-2)(n+24)} \quad , \quad n \geq 2 \quad (A.2-50)$$

and the attenuated white noise model of Heller and Jordan (Ref. 24), where

$$k_n = \frac{(2n+1)D^2(2R-D)\sigma_T^2}{(R-D)^2(2R^2-2DR+D^2)} \left(\frac{R-D}{R}\right)^{n+1} \quad (\text{A.2-51})$$

The Tscherning and Rapp model has two parameters, A and S. A sets the overall level of the covariance and usually S is slightly less than unity. Also, k_n is set to zero for n less than 2, and for very large values of n as well.

The attenuated white noise model also has two parameters. D is the depth of a sphere on which the anomalous potential is a white noise process and σ_T^2 is the variance on that sphere. In addition to this clear physical interpretation, the covariance function for the attenuated white noise model has the advantage of a closed-form expression, which is more efficient for computational purposes than the summation in Eq. A.2-48.

Given the covariance function $K(P,Q)$ in the form of Eq. A.2-48, the gravity anomaly covariance may be expressed in a related series. It is

$$C(P,Q) = \sum_{n=0}^{\infty} \frac{(n-1)^2 k_n}{R^2} \left(\frac{R}{r_P r_Q}\right)^{n+2} P_n(\cos \psi) \quad (\text{A.2-52})$$

which follows from Eq. A.2-46).

For local covariance functions, in the flat-earth approximation, there are analogs to the above expressions.

$$K(P,Q) = \int_0^{\infty} k(w) e^{-w(z_P+z_Q)} J_0(ws) w dw \quad (A.2-53)$$

where J_0 is the zero-order Bessel function of the first kind and

$$s = [(x_P - x_Q)^2 + (y_P - y_Q)^2]^{\frac{1}{2}} \quad (A.2-54)$$

is clearly stationary, isotropic, and symmetric. It is also harmonic in the coordinates of both P and Q because

$$e^{-w(z_P+z_Q)} J_0(ws)$$

satisfies Laplace's equation, and it is positive semi-definite if and only if

$$k(w) \geq 0 \quad (A.2-55)$$

for all w . The corresponding expression for the gravity anomaly covariance function is

$$C(P,Q) = \int_0^{\infty} w^2 k(w) e^{-w(z_P+z_Q)} J_0(ws) w dw \quad (A.2-56)$$

Two examples are the flat-earth form of the attenuated white noise model (Ref. 24) in which

$$k(w) = 4D^2 \sigma_T^2 e^{-2wD} \quad (A.2-57)$$

and Reilly's covariance model (Refs. 25, 26), in which

$$k(w) = C_0(d^4/2) e^{-w^2 d^2/2} \quad (\text{A.2-58})$$

A.2.4 Collocation

Given a covariance function for the anomalous potential $K(P,Q)$ and the linear operators in Table A.2-1, it is straightforward to generalize least-squares collocation to estimate quantities of different types from data of different types. In fact, Eqs. A.2-31 and A.2-38 hold exactly if the definitions of the observation vector \underline{l} , the estimation vector $\underline{\hat{s}}$, and the covariance matrices are modified. This is most easily demonstrated with a concrete example.

Suppose that, rather than consisting solely of gravity anomaly measurements as in Eq. A.2-7, the observation vector \underline{l} includes deflections of the vertical also, e.g.,

$$\underline{l} = \begin{pmatrix} \Delta g \text{ at } Q_1 + n_1 \\ \xi \text{ at } Q_2 + n_2 \\ \vdots \\ \vdots \end{pmatrix} \quad (\text{A.2-59})$$

and that both deflection of the vertical and geoid undulation are to be estimated, e.g.,

$$\underline{\hat{s}} = \begin{pmatrix} \hat{\xi} \text{ at } P_1 \\ \hat{N} \text{ at } P_2 \\ \vdots \\ \vdots \end{pmatrix} \quad (\text{A.2-60})$$

Then the covariance matrices appearing in Eqs. A.2-31 and A.2-38 become

$$C_{s\ell} = E\{\underline{s} \underline{\ell}^T\} = \begin{pmatrix} L_{P_1}^{\xi} & L_{Q_1}^{\Delta g} K & L_{P_1}^{\xi} & L_{Q_2}^{\xi} K & \dots \\ L_{P_2}^N & L_{Q_1}^{\Delta g} K & L_{P_2}^N & L_{Q_2}^{\xi} K & \\ \vdots & \vdots & \vdots & \vdots & \end{pmatrix} \quad (A.2-61)$$

$$\bar{C}_{\ell\ell} = E\{\underline{\ell} \underline{\ell}^T\} = \begin{pmatrix} L_{Q_1}^{\Delta g} L_{Q_1}^{\Delta g} K + D_{11} & L_{Q_1}^{\Delta g} L_{Q_2}^{\xi} K + D_{12} & \dots \\ L_{Q_1}^{\Delta g} L_{Q_2}^{\xi} K + D_{12} & L_{Q_2}^{\xi} L_{Q_2}^{\xi} K + D_{22} & \\ \vdots & \vdots & \end{pmatrix} \quad (A.2-62)$$

and

$$C_{ss} = E\{\underline{s} \underline{s}^T\} = \begin{pmatrix} L_{P_1}^{\xi} & L_{P_1}^{\xi} K & L_{P_1}^{\xi} & L_{P_2}^N K & \dots \\ L_{P_1}^{\xi} & L_{P_2}^N K & L_{P_2}^N & L_{P_2}^N K & \\ \vdots & \vdots & \vdots & \vdots & \end{pmatrix} \quad (A.2-63)$$

$$\text{where } \underline{s} = \begin{pmatrix} \text{true value of } \xi \text{ at } P_1 \\ \text{true value of } N \text{ at } P_2 \\ \vdots \\ \vdots \end{pmatrix} \quad (\text{A.2-64})$$

and $E\{(\underline{s}-\hat{\underline{s}})^T (\underline{s}-\hat{\underline{s}})\}$ has been minimized.

By the above approach, the least-squares interpolation of a set of data (including errors) of homogeneous type has been extended to least-squares collocation, in which the types of data and estimated quantities may be heterogeneous. In addition, it is possible to incorporate the simultaneous estimation of a set of parameters upon which the data are linearly dependent. Such systematic adjustments might pertain, for example, to the geodetic reference system, the density chosen for terrain corrections, or arbitrary long-wavelength trends in the data. In practice, however, such adjustments are often done independently of the collocation procedure (e.g., Refs. 20, 21) and the details are omitted here. They are available in many of the works by Moritz (e.g., Refs. 2, 17).

A.2.5 Practical Considerations

A remark on the computational aspect of least-squares interpolation and collocation is necessary. The matrix inverse

$$\bar{C}_{\ell\ell}^{-1}$$

appears in both the expression for the optimal value of $\Delta\hat{g}_p$ (Eq. A.2-28) and the expression for its covariance (Eq. A.2-29),

and also in the more general expressions in Eqs. A.2-31 and A.2-38. However, in practice, it is more efficient and accurate to avoid the explicit computation of a matrix inverse. Instead, one should deal directly with the fundamental expressions in Eqs. A.2-24, -25, and -26.

Because $\bar{C}_{\ell\ell}$ is symmetric and positive semi-definite it has a Cholesky decomposition (e.g., Ref. 27) such that

$$\bar{C}_{\ell\ell} = U^T U \quad (\text{A.2-65})$$

where U is an upper triangular matrix. Once U has been computed, Eq. A.2-26 is solved for the 1 by n coefficient matrix A in two steps. First, the solution y to the system

$$U^T y = C_{p\ell}^T \quad (\text{A.2-66})$$

is computed. This involves only straightforward substitution because of the triangular structure of U^T . Next, A is computed from

$$UA^T = y \quad (\text{A.2-67})$$

which is likewise straightforward. Then $\Delta\hat{g}_p$ is computed directly from Eq. A.2-24 rather than from Eq. A.2-28. Similarly, $E\{e_p^2\}$ is computed from

$$E\{e_p^2\} = C_{pp} - AC_{p\ell}^T \quad (\text{A.2-68})$$

(obtained by using Eq. A.2-26 to eliminate $\bar{C}_{\ell\ell}$ from Eq. A.2-25) rather than from Eq. A.2-29. This procedure is readily extended to compute estimates of multiple quantities and their covariances (in either interpolation or collocation), denoted formally by

Eqs. A.2-31 and -38. Note that the Cholesky decomposition need not be repeated because the same data covariance matrix $\bar{C}_{\ell\ell}$ is needed for each of the estimates.

A second remark concerns the covariance of the gravity field and the handling of data. As mentioned above, stationary, isotropic covariance models are normally used. However, the gravity field of the earth is far from stationary. Its character varies with location on a global scale (e.g., between ocean basin, continental shelf, continent, etc) and on a local scale (e.g., between a mountain and adjacent lowland). Also, the prominence of linear features such as ocean trenches and rises, island chains, mountain chains, and continental rift zones indicates that the field is far from isotropic. In practice (Ref. 21), this difficulty is circumvented not by using non-stationary, anisotropic covariance models (which would require too many parameters to be practical) but rather by estimating residual quantities from residual data. The residuals are computed by removing systematic components, such as those computed from topography and from long-wavelength models of the gravity field, from the data. Collocation is performed on the residual field, which is generally more stationary and isotropic than the field itself. After collocation, the systematic components are restored, i.e., added to the estimated residual quantities.

A.3 THE GEOFAST ALGORITHM

A.3.1 Formulation of the Problem

The GEOFAST algorithm (Ref. 16) was developed to provide an efficient computational solution to the minimum-variance estimation equations

$$\hat{\underline{x}} = C_{xz} C_{zz}^{-1} \underline{z} \quad (\text{A.3-1})$$

In geodetic work, this formula is commonly known as least-squares collocation. It is equivalent to Eq. A.2-31 with minor notational changes: \underline{x} replaces \underline{s} , \underline{z} replaces \underline{l} , and the bar on \bar{C}_{zz} is dropped for simplicity. Here, \underline{z} is a data vector of dimension N and C_{zz} is the sum of its auto-covariance matrix (of dimension N by N) plus a measurement noise covariance matrix. The vector of estimates $\hat{\underline{x}}$ is of dimension M , and C_{xz} is the cross-covariance matrix between \underline{x} and \underline{z} of dimension M by N . The data covariance is generally modeled by an analytic function with parameters fitted to global or local data. The cross-covariance matrix C_{xz} is then analytically derived from the auto-covariance by using the physical relationship between the estimated quantities \underline{x} and the observed quantities \underline{z} (Appendix A.2.3). The method is implicit since this relationship does not appear explicitly via a measurement equation of the form $\underline{z} = H \underline{x}$. Formally, the covariances are defined by

$$C_{zz} = E\{\underline{z} \underline{z}^T\}, \quad C_{xz} = E\{\underline{x} \underline{z}^T\} \quad (\text{A.3-2})$$

(equivalent to Eqs. A.2-23 and A.2-32) where E is the expectation operator and both vectors are assumed to have zero means.

Computer solution of Eq. A.3-1 by standard techniques involves on the order of N^3 operations (such as multiplications and additions) to obtain the intermediate vector

$$\underline{u} = C_{zz}^{-1} \underline{z} \quad (\text{A.3-3})$$

and on the order of MN operations to yield the estimates

$$\hat{\underline{x}} = C_{xz} \underline{u} \quad (\text{A.3-4})$$

This limits the feasible application of these methods to data sets of a few hundred points at most, whereas thousands of measurements are often available from sensors such as satellite altimeters.

With some assumptions about the data and the use of frequency domain techniques, this workload can be reduced dramatically to the order of $N \log_2 N$. These assumptions are as follows. First, let the data points $z(\theta, \phi)$ be given on a rectangular grid in the θ, ϕ plane (Fig. A.3-1). Second, assume that the covariance between two data points is a function of relative position only. That is, the covariance function is shift-invariant (or a displacement kernel)

$$\text{COV} [z(\theta_1, \phi_1), z(\theta_2, \phi_2)] = f_{zz}(\theta_2 - \theta_1, \phi_2 - \phi_1) \quad (\text{A.3-5})$$

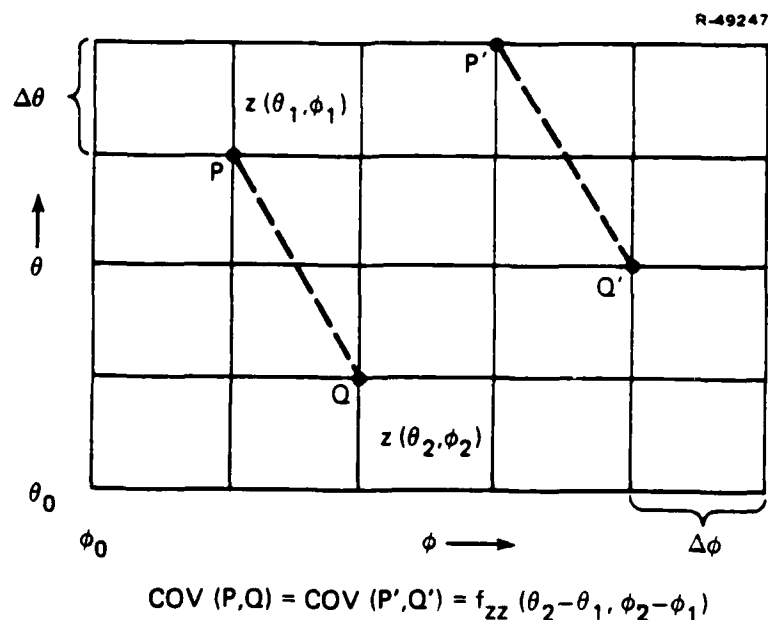


Figure A.3-1 Data and Covariance Structure

Note that this includes, but is not restricted to, the case of isotropic models. Third, similar conditions are assumed for the cross-covariance and estimate points $x(\theta, \phi)$, namely,

$$\text{COV} [x(\theta_1, \phi_1), z(\theta_2, \phi_2)] = f_{xz}(\theta_2 - \theta_1, \phi_2 - \phi_1) \quad (\text{A.3-6})$$

Fourth, the estimates are to be obtained on the same grid as the data.

The foregoing assumptions are consistent with practical applications. The GEOFAST algorithm maps data given on a limited region of a spherical (or ellipsoidal) surface onto a plane with very little distance distortion. The data are then gridded. Shift invariance then corresponds to the common model of stationary statistics. The estimate grid may actually be any translation (that is any offset in altitude, latitude, and longitude) of the data grid. With a fast algorithm, it is often cheaper to compute estimates at all grid locations even if only a subset is wanted.

The estimation equation (Eq. A.3-1) takes on a special structure which is exploited by the GEOFAST algorithm. The natural form for the data is an n_1 by n_2 matrix

$$Z = [z_{jk}] \quad , \quad z_{jk} = z(\theta_0 + j\Delta\theta, \phi_0 + k\Delta\phi) \quad (\text{A.3-7})$$

where $j=0,1,\dots,n_1-1$ and $k=0,1,\dots,n_2-1$ corresponding to the data grid (Fig. A.3-1) with origin (θ_0, ϕ_0) and mesh size $(\Delta\theta, \Delta\phi)$. The total number of grid points is $N = n_1 n_2$. The data matrix Z is put in vector form \underline{z} by listing its elements in row-by-row order. With this convention the N by N covariance matrix C_{zz} assumes a block structure (see Ref. 16)

$$C_{zz} = \begin{bmatrix} T_0 & T_1 & \cdot & \cdot & T_{n_1-1} \\ T_{-1} & T_0 & \cdot & \cdot & T_{n_1-2} \\ \cdot & \cdot & \cdot & \cdot & \cdot \\ T_{-(n_1-1)} & T_{-(n_1-2)} & \cdot & \cdot & T_0 \end{bmatrix} \quad (\text{A.3-8})$$

in which there are n_1 by n_1 blocks and each block is of dimension n_2 by n_2 . The block matrix T_k is the cross-covariance between the elements in two rows of Z which are k rows apart. This depends only on k by shift-invariance. By the same argument each block matrix T_k is of the form

$$\begin{bmatrix} t_0 & t_1 & \cdot & \cdot & t_{n_2-1} \\ t_{-1} & t_0 & \cdot & \cdot & t_{n_2-2} \\ \cdot & \cdot & \cdot & \cdot & \cdot \\ t_{-(n_2-1)} & t_{-(n_2-2)} & \cdot & \cdot & t_0 \end{bmatrix} \quad (\text{A.3-9})$$

where t is evaluated using Eq. A.3-5 or A.3-6.

The matrix C_{zz} is said to be block Toeplitz with Toeplitz blocks, or simply block Toeplitz. Note that C_{zz} is symmetric and is completely determined by its first block row (or block column), whereas the blocks (except T_0) are not symmetric and are determined by their first row and column. Altogether the definition of C_{zz} requires fewer than $2n_1n_2 = 2N$ parameters. The structure of C_{xz} is also block Toeplitz, but symmetry does not hold in general; approximately $4N$ parameters are needed to define it. In summary, the geodetic estimation

problem becomes equivalent to the inversion and multiplication of block Toeplitz matrices.

A.3.2 Outline of the Algorithm

The GEOFAST algorithm achieves its efficiency by transforming the estimation equations into the frequency domain where an accurate approximation can be made to reduce the workload. The transformation is accomplished with the Fast Fourier Transform (FFT), which requires on the order of $N \log_2 N$ operations. The transformed covariance matrices are closely approximated by (block) banded matrices resulting in a solution workload of order N . A simple trade-off between approximation accuracy and computer workload is controllable by choice of the bandwidth.

A simplified flow chart of the algorithm is shown in Fig. A.3-2. Input to the computation consists of the n_1 by n_2 data matrix Z , together with the definition of the covariance matrices C_{xz} , C_{zz} . As seen in Eqs. A.3-8 and A.3-9, each covariance can be specified by $4n_1n_2$ parameters which are naturally arranged as a $2n_1$ by $2n_2$ correlation matrix. Specifically, let the Toeplitz matrix T in Eq. A.3-9 be represented by the column vector

$$\underline{t} = \left[0, t_{-(n_2-1)}, \dots, t_{-1}, t_0, t_1, \dots, t_{n_2-1} \right]^T \quad (\text{A.3-10})$$

of dimension $2n_2$. Then each block matrix T_k in Eq. A.3-8 can be represented by a vector \underline{t}_k , and the matrix C_{zz} by the $2n_1$ by $2n_2$ matrix

$$T_{zz} = \left[\begin{array}{c|c|c|c|c|c|c|c} 0 & \underline{t}_{-(n_1-1)} & \cdots & \underline{t}_{-1} & \underline{t}_0 & \underline{t}_1 & \cdots & \underline{t}_{n_1-1} \end{array} \right]^T \quad (\text{A.3-11})$$

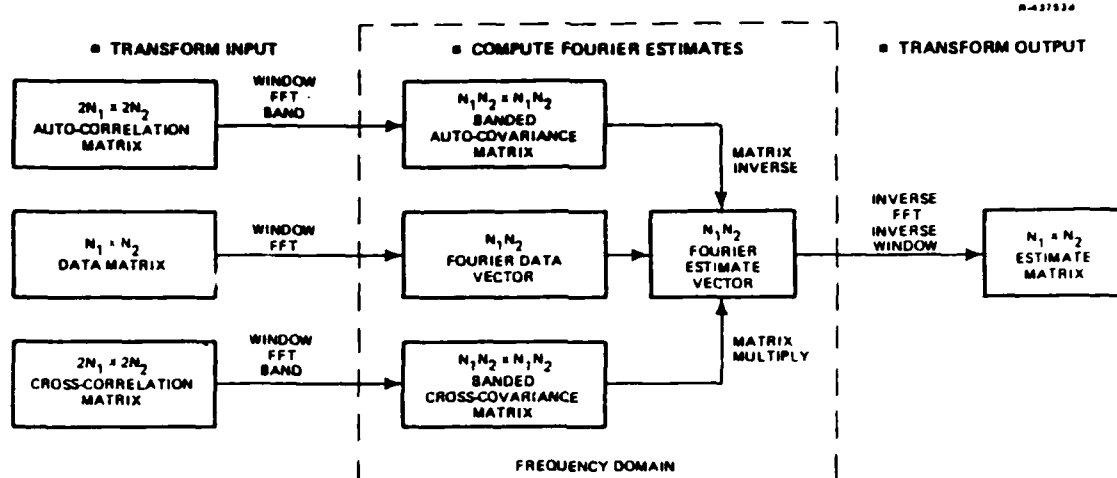


Figure A.3-2 Two-Dimensional GEOFAST Algorithm

For the symmetric case (C_{zz}) only half of the matrix T_{zz} is required with $\underline{t}_{-k} \equiv \underline{t}_k$. Total computer storage for input is of order $N = n_1 n_2$.

The first stage of the algorithm is the transformation of the inputs to the frequency domain. The FFT is simply an efficient implementation of the complex Discrete Fourier Transform (DFT) which is defined in two dimensions by

$$z'_{pq} = \frac{1}{\sqrt{n_1 n_2}} \sum_{j=0}^{n_1-1} \sum_{k=0}^{n_2-1} z_{jk} \exp \left\{ -2\pi i \left(\frac{pj}{n_1} + \frac{qk}{n_2} \right) \right\} \quad (\text{A.3-12})$$

Since the estimation equations, Eq. A.3-1, are in terms of the data vector \underline{z} it is convenient to express Eq. A.3-12 in the equivalent matrix form,

$$\underline{z}' = \underline{F} \underline{z} \quad (\text{A.3-13})$$

The N by N complex two-dimensional DFT matrix F has a special structure which is discussed further in Ref. 16. The vector \underline{z}' in Eq. A.3-13 is the complex representation of the data vector \underline{z} in a finite Fourier series of complex exponentials. Since real quantities are more convenient to deal with in a computer, a further transformation to a sine and cosine series is performed by combining real and imaginary parts. This corresponds to the matrix operations (redefining \underline{z}')

$$\underline{z}' = H F \underline{z} \quad (\text{A.3-14})$$

where H is a very sparse complex N by N matrix. The product HF is, of course, a real matrix.

Finally, the accuracy of the banded approximation, which is essential for the success of the algorithm, is critically enhanced by the introduction of a data window. In matrix form this becomes (redefining \underline{z}' again)

$$\underline{z}' = H F W \underline{z} \quad (\text{A.3-15})$$

where W is a real N by N diagonal matrix. That is, each data value z_{jk} is multiplied by a scalar weight w_{jk} before applying the DFT. This windowing compensates for the finite extent of the data grid in a manner explained in Ref. 16. A representative window function in two dimensions would be a gaussian probability density which is peaked at the center and tapered toward the edges of the data grid. In GEOFAST an optimal one-dimensional window w^0 derived by Kaiser (Ref. 28) is used to form a product window $w_{jk} = (w_j^0)(w_k^0)$ (Fig. A.3-3). The combined data transformation in Eq. A.3-15 can be implemented in order $N \log_2 N$ operations since multiplications by H and W are both order N .

R-49248

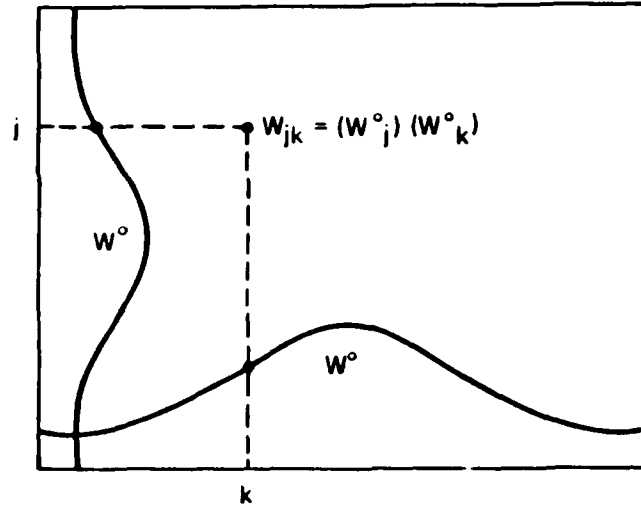


Figure A.3-3 Product Window Definition

Corresponding to the frequency domain data vector \underline{z}' (consisting of Fourier coefficients) is the auto-covariance matrix

$$C'_{zz} = E\{\underline{z}'(\underline{z}')^T\} = (H F W) C_{zz} (H F W)^T \quad (A.3-16)$$

Similarly, introducing the transformed estimates

$$\underline{\hat{x}}' = (H F W) \underline{\hat{x}} \quad (A.3-17)$$

leads to the cross-covariance matrix

$$C'_{xz} = E\{\underline{\hat{x}}'(\underline{z}')^T\} = (H F W) C_{xz} (H F W)^T \quad (A.3-18)$$

A straightforward row and column implementation of Eqs. A.3-16 and A.3-18 would result in an order $N^2 \log_2 N$ algorithm. This is avoided by replacing C'_{xz} and C'_{zz} by their banded approximations, and calculating only those elements within the retained bands. If the number of bands in the one-dimensional window is m_B this

reduces the workload to the order of $m_B^2 N \log_2 N$, where for typical applications m_B is small and independent of N . The scheme used to compute C'_{xz} and C'_{zz} bandwise is derived in Ref. 16 and is an essential part of the GEOFAST algorithm.

The preceding transformations constitute the first stage of the calculation (Fig. A.3-2). Note that storage requirements for the covariances are of order $m_B^2 N$. The second stage consists of the solution of the estimation equations in the frequency domain. The estimation equations in the transformed variables become simply

$$\underline{\hat{x}}' = C'_{xz} (C'_{zz})^{-1} \underline{z}' \quad (\text{A.3-19})$$

coupled with the inverse of Eq. A.3-17

$$\underline{\hat{x}} = (H F W)^{-1} \underline{\hat{x}}' \quad (\text{A.3-20})$$

It is easily verified that the solution of Eqs. A.3-19 and A.3-20 is identical to the solution of Eq. A.3-1. As before, the equations are solved in two steps

$$\underline{u}' = (C'_{zz})^{-1} \underline{z}' \quad (\text{A.3-21})$$

$$\underline{\hat{x}}' = C'_{xz} \underline{u}' \quad (\text{A.3-22})$$

Since C'_{xz} is banded, the multiplication in Eq. A.3-22 requires only on the order of $m_B^2 N$ operations.

However, analysis of the solution of Eq. A.3-21 is more complicated. It is shown in Ref. 16 that the block

Toeplitz structure of C_{zz} in Eq. A.3-8 gives rise to a corresponding block-banded structure for C'_{zz} in which the blocks are also banded (Fig. A.3-4). There is an essential difference between this structure and the simple band structure of a diagonal block which is the one-dimensional analog of C'_{zz} . In the one-dimensional problem the symmetric band matrix C'_{zz} can be inverted in order $m_B^2 n$ operations by the standard Cholesky technique (Refs. 29, 30), where n is the matrix dimension and m_B the number of superdiagonal bands. When the Cholesky technique is applied to the block-banded structure of the two-dimensional problem, the internal banding within the blocks is lost during the calculation. This difficulty is known as "fill-in." The result is an effective bandwidth of $m_B n_2$, where m_B is now the number of blockbands of size n_2 by n_2 , and a workload of order $(m_B n_2)^2 (n_1 n_2)$. Assuming $n_1 = n_2$ gives an order of effort proportional to $n_1^4 = N^2$ rather than N .

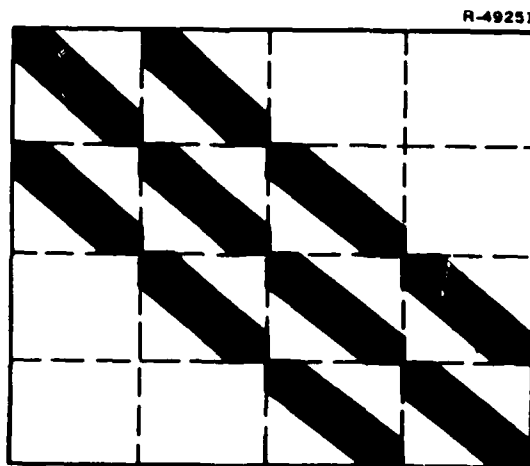


Figure A.3-4 Block Banded Structure

If it is desired to reduce the computing effort further, an order N algorithm for the solution of Eq. A.3-21 can be developed by using an iterative method based on a special class of covariance matrices. This special type of covariance structure is termed separable and is characterized by a covariance function in Eq. A.3-14 of the form

$$f_{zz}(\theta_2 - \theta_1, \phi_2 - \phi_1) = f_1(\theta_2 - \theta_1) f_2(\phi_2 - \phi_1) \quad (\text{A.3-23})$$

This class of functions is not general enough to include the statistical models required for gravimetric applications, but it can serve as an approximation for use in an iterative method. It is shown in Ref. 16 that for a separable covariance matrix Eq. A.3-21 "factors" into two one-dimensional matrix equations of the form

$$V' = (C_2')^{-1} (Z')^T \quad (\text{A.3-24})$$

$$U' = (C_1')^{-1} (V')^T \quad (\text{A.3-25})$$

where C_1' , C_2' correspond to f_1 , f_2 and are square band matrices of dimension n_1 , n_2 . The matrices Z' and U' are both of dimension n_1 by n_2 , and are equivalent to the vectors \underline{z}' and \underline{u}' when their elements are listed in row-by-row order. If the bandwidth of the matrix C_2' is m_B , then Eq. A.3-24 can be solved by the Cholesky method in order $m_B n_2 (m_B + n_1)$ operations. Assuming $n_1 = n_2$, the total workload for both equations is thus of order $m_B N$ in the separable case.

The iterative solution of Eq. A.3-21 in the nonseparable case proceeds as follows. Choose the matrix D' as a separable approximation to C'_{zz} (which may be done in a natural way) and define the matrix E' by

$$C'_{zz} = D' + E' \quad (A.3-26)$$

The matrix E' will be block-banded since both C'_{zz} and D' are. The estimation equation can now be written implicitly

$$\underline{u}' = (D')^{-1} [\underline{z}' - E'\underline{u}'] \quad (A.3-27)$$

or in recursive form

$$\underline{u}'(k+1) = (D')^{-1} [\underline{z}' - E'\underline{u}'(k)] \quad (A.3-28)$$

where k indicates the iteration number and $\underline{u}'(0)$ is any convenient initial solution.

Since both the inversion and multiplication in Eq. A.3-28 require on the order of N operations, so does one step of the iteration. If the number of steps, m_s , necessary for convergence of the iteration is independent of N and small enough, the total workload to solve Eq. A.3-21 is of order N . It can be shown that the rate of convergence depends on the norm of the matrix $(D')^{-1}E'$, which will be small if the separable approximation is a good one. Furthermore, a simple modification to the iteration guarantees convergence for any positive definite matrix D' . The convergence properties of the iterative technique, Eq. A.3-28, and the appropriate choice of the approximating matrix D' are discussed in Ref. 16.

The solution of the estimation equations in the frequency domain completes the second stage of the GEOFAST algorithm (Fig. A.3-2). The third stage consists of the inverse transformation back to the space domain (Eq. A.3-20). Since W is a diagonal matrix, its inverse is an order N operation. The complex DFT matrix F can be inverted in order $N \log_2 N$ operations

by means of the inverse FFT, while the inverse of the matrix H can be obtained analytically and has the same sparse structure as H itself. Thus, the final stage has a workload dominated by $N \log_2 N$.

The computer time and storage requirements for the GEOFAST algorithm are summarized in Table A.3-1. The numbers given are asymptotic estimates, valid for large N , and do not include multiplicative factors independent of N except for m_B and m_s . For repeated application of the algorithm with the same covariance model the matrices C'_{xz} and C'_{zz} can be stored, reducing the time requirement to the order of $N \log_2 N$ for each application to a new data set.

TABLE A.3-1
COMPUTER TIME AND STORAGE REQUIREMENTS

ALGORITHM STAGE	ASYMPTOTIC ORDER OF MAGNITUDE	
	TIME	STORAGE
1: Input Transforms	$m_B^2 N \log_2 N$	$m_B^2 N$
2: Estimation Equations	$m_s m_B^2 N$	$m_B^2 N$
3: Output Transform	$N \log_2 N$	N
Full Solution	$m_B^2 N \log_2 N$	$m_B^2 N$

N = Total number of data points

m_B = Bandwidth in one dimension

m_s = Number of steps for convergence

A.4 OTHER FOURIER TRANSFORM METHODS

When the flat-earth approximation is valid (Ref. 31), methods based on the two-dimensional Fourier transform lead to efficient algorithms for a variety of geodetic computations. The flat-earth versions of the Stokes integral for geoid undulation, the Vening Meinesz integral for deflections of the vertical, and the Poisson integral for upward continuation are naturally implemented by Fourier transforms, because each has the form of a two-dimensional linear convolution. In addition, the flat-earth terrain correction can be approximated as a sum of linear convolution integrals.

This appendix considers the basic theory of Fourier transform methods. Section A.4.1 states the conventions and notation used for two-dimensional Fourier transforms and convolutions. The Fourier transform implementations of the Stokes and Vening Meinesz integrals are outlined in Section A.4.2. (Upward continuation, long known to be very straightforward in the transform domain, is omitted from further discussion.)

All Fourier transform methods have several elements in common. In each case, the basic strategy is as follows:

- Apply appropriate weighting and/or enclosing windows to the data
- Take the numerical Fourier transform of a set of measurements
- Multiply by the appropriate transfer function (almost always computed directly from an analytic expression)
- Finish by returning to the space domain with a numerical inverse transform.

The methods are fast, because they take advantage of the speed of the Fast Fourier Transform (FFT) algorithm, and simultaneously compute all output values. They require a regular grid of input data, and return output values on the same geographical grid as the input data. (Values at intermediate or arbitrary points must be interpolated.) As with most Fourier transform applications, care is required to apply reasonable windowing to the data (to avoid undesirable edge effects) and to avoid spatial aliasing in the input data.

A.4.1 Fourier Transforms and Convolution Integrals

In the following two sections Bracewell's (Ref. 32, pp. 241-243) conventions for the two-dimensional Fourier transform and two-dimensional convolution integral are used. The Fourier transform of a two-dimensional function $f(x,y)$ is defined by

$$F(u,v) = \iint f(x,y) e^{-i2\pi(ux+vy)} dx dy \quad (A.4-1)$$

where x and y are Cartesian coordinates in the plane, u and v are Cartesian coordinates in the transform domain, and $i = \sqrt{-1}$. The integration extends over the entire plane; the limits are omitted for convenience. The inverse transform is given by

$$f(x,y) = \iint F(u,v) e^{i2\pi(ux+vy)} du dv \quad (A.4-2)$$

Here again, and throughout the remainder of the section, integration limits of $-\infty$ and $+\infty$ are omitted for convenience.

The convolution of a pair of two-dimensional functionals $f(x,y)$ and $g(x,y)$ is expressed by the integral

$$f \star g \Big|_{x,y} = \iint f(x',y')g(x-x',y-y')dx'dy' \quad (A.4-3)$$

where the primes denote auxiliary variables of integration. According to the Convolution Theorem the Fourier transform of a convolution is simply the product $F(u,v)G(u,v)$, where G denotes the Fourier transform of g . Applying Eq. A.4-2 yields

$$f \star g \Big|_{x,y} = \iint F(u,v)G(u,v)e^{i2\pi(ux+vy)}dudv \quad (A.4-4)$$

which is the principal basis for the methods described in the remainder of this section.

A.4.2 Stokes and Vening Meinesz Integrals

Derivation of the Fourier transform versions of the flat-earth Stokes and Vening Meinesz integrals is straightforward, because there is no need for approximations to cast them in the form of linear convolution integrals; the exact formulas already are in such form. Thus, as outlined in Ref. 31 and implemented by Sideris (in Ref. 21) and at TASC (this report, p. A-57), it is natural to apply Fourier transform (hence FFT) methods to the computation of geoid undulation and deflections of the vertical from gravity anomalies.

The flat-earth Stokes integral for undulation of the geoid is

$$N(x_p, y_p) = \frac{1}{2\pi g_0} \iint \frac{\Delta g(x, y)}{r_0} dx dy \quad (A.4-5)$$

where g_0 is normal gravity, Δg is the gravity anomaly function, and $r_0 = [(x_p - x)^2 + (y_p - y)^2]^{\frac{1}{2}}$. The north (meridional) and east (prime vertical) components of the deflection of the vertical, ξ and η , respectively, are given by the flat-earth Vening Meinesz integral

$$\begin{pmatrix} \xi(x_p, y_p) \\ \eta(x_p, y_p) \end{pmatrix} = \frac{1}{2\pi g_0} \iint \Delta g(x, y) \begin{pmatrix} (y_p - y)/r_0^3 \\ (x_p - x)/r_0^3 \end{pmatrix} dx dy \quad (A.4-6)$$

where the y-axis is directed north and the x-axis is directed east. (Note that $\xi = -\partial N/\partial y$ and $\eta = -\partial N/\partial x$.)

Expressed as convolutions, Eqs. A.4-5 and A.4-6 are

$$N(x_p, y_p) = \frac{1}{2\pi g_0} \Delta g * \frac{1}{(x^2 + y^2)^{\frac{1}{2}}} \Big|_{x_p, y_p} \quad (A.4-7)$$

$$\begin{pmatrix} \xi(x_p, y_p) \\ \eta(x_p, y_p) \end{pmatrix} = \frac{1}{2\pi g_0} \Delta g * \begin{pmatrix} y/(x^2 + y^2)^{3/2} \\ x/(x^2 + y^2)^{3/2} \end{pmatrix} \Big|_{x_p, y_p} \quad (A.4-8)$$

The Fourier transforms of the kernel functions in Eqs. A.4-7 and A.4-8 are straightforward closed-form expressions. The FFT may be applied to gridded gravity anomaly data to estimate the

Fourier transform $\Delta G(u,v)$. Thus, one may evaluate Eqs. A.4-7 and A.4-8 efficiently, at all points on a regular grid, by multiplication in the transform domain followed by an inverse FFT, as in Eq. A.4-4. The relevant Fourier transform pairs are listed in Table A.4-1.

Some of the practical aspects of using geodetic algorithms based on FFT implementation of the convolution Eqs. A.4-7 and A.4-8 have already been mentioned. In the late 1970s, TASC implemented computer programs using a mixed radix FFT for performing the flat-earth Stokes and Vening Meinesz computations. Work with this software, using marine gravity and altimetry data, as well as terrestrial observations, clarified some of the advantages and disadvantages of the Fourier transform approach. Unlike collocation, this approach is deterministic, not statistical. An advantage relative to collocation is that

TABLE A.4-1
FOURIER TRANSFORM PAIRS

FUNCTION	TRANSFORM
$\Delta g(x,y)$	$\Delta G(u,v)$
$1/(x^2+y^2)^{1/2}$	$1/(u^2+v^2)^{1/2}$
$y/(x^2+y^2)^{3/2}$	$-2\pi i v/(u^2+v^2)^{1/2}$
$x/(x^2+y^2)^{3/2}$	$-2\pi i u/(u^2+v^2)^{1/2}$
$\left\{ \begin{array}{l} N(x,y) \\ \xi(x,y) \\ \eta(x,y) \end{array} \right\}$	$\frac{1}{2\pi g_0} \Delta G(u,v)/(u^2+v^2)^{1/2}$ $-\frac{i}{g_0} \Delta G(u,v) \left\{ \begin{array}{l} v/(u^2+v^2)^{1/2} \\ u/(u^2+v^2)^{1/2} \end{array} \right\}$

there is no need to assume covariance models, yet the corresponding disadvantage is that the variances and covariances of the estimation errors are not available. A characteristic of the FFT approaches is that data and estimates must be on regular grids. As discussed above in Section A.3.1 of this appendix, the grid requirement is consistent with practical applications; the computational effort of gridding the data is more than offset by the much improved efficiency of these methods.

Other important aspects of the FFT approaches that must be considered are the need to control spectral leakage and aliasing by proper windowing of the data region. TASC found that leakage problems could be controlled by first removing a low-order spherical harmonic reference field from the data, then adding back the appropriate reference values after applying the flat-earth Stokes or Vening Meinesz algorithms to the reduced data. (This approach is also described in Ref. 21.) Edge effects have been successfully controlled in work at TASC by adding a continuous border region to the data, formed by two-dimensional reflection of the outer edge of the data. The frequency domain algorithms are then applied to the FFT of the extended region.

When implemented with the practical modifications described above, the FFT-based flat-earth Stokes and Vening Meinesz algorithms have proven to be very fast, accurate, and easy to implement. They deserve more widespread use.

APPENDIX B
FFT TERRAIN CORRECTION ALGORITHM: DETAILS OF
NEW DERIVATION

This appendix describes in detail the new derivation of the FFT terrain correction algorithm introduced in Chapter 5 and Ref. 35. As noted in Chapter 5, the flat-earth terrain correction, a nonlinear function of terrain elevation $h(x,y)$, may be expressed approximately in terms of linear convolution integrals involving h and h^2 . The appendix begins with a review of the previous derivations of such approximate forms (Refs. 33 and 34). It is followed by the new derivation, showing how the approximation is more rigorous than claimed by its proponents. Finally, two analytic examples illustrate the effects of various forms of the approximation.

The flat-earth terrain correction, evaluated at the point (x_p, y_p) , is given by (e.g., Eq. 5-1; Ref. 33, Eq. 11; Ref. 34, Eq. 7.16)

$$c(x_p, y_p) = G\rho \iint dx dy \int_{h_p}^{h(x,y)} \frac{(z-h_p)dz}{[(x_p-x)^2 + (y_p-y)^2 + (h_p-z)^2]^{3/2}}$$

(B-1)

where G is the gravitational constant, ρ is the density assumed for the terrain, and $h_p = h(x_p, y_p)$.

Now, expanding the denominator,

$$\begin{aligned}\frac{1}{r^3} &= \frac{1}{[(x_p-x)^2 + (y_p-y)^2 + (h_p-z)^2]^{3/2}} \\ &= \frac{1}{r_0^3} - \frac{3}{2} \frac{(z-h_p)^2}{r_0^5} + \dots\end{aligned}\quad (B-2)$$

where $r_0 = [(x_p-x)^2 + (y_p-y)^2]^{1/2}$. Thus, it is reasonable to make the approximation

$$\frac{1}{r^3} \approx \frac{1}{r_0^3} \quad (B-3)$$

assuming $(z-h_p)^2/r_0^2 \ll 1$, and to integrate over z to obtain

$$c(x_p, y_p) \approx \frac{1}{2} G\rho \iint \frac{[h(x,y)-h_p]^2}{[(x_p-x)^2 + (y_p-y)^2]^{3/2}} dx dy \quad (B-4)$$

In both previous derivations (Ref. 33, Eq. 14; Ref. 34, Eq. 7.17), this is an important intermediate result. Note that the quantity $(z-h_p)^2/r_0^2$ is generally small for large r_0 while for very small r_0 it is bounded by the square of the topographic slope S :

$$(z-h_p)^2/r_0^2 \leq (h(x,y)-h_p)^2/r_0^2 \leq S^2 \quad (B-5)$$

Equation B-4 may be expressed as a sum of two convolutions plus a constant term by expanding the numerator:

$$c(x_p, y_p) \approx \frac{1}{2} G\rho \left[\left. (h^2 * f) \right|_{x_p, y_p} - 2h_p \left. (h * f) \right|_{x_p, y_p} + h_p^2 \iint f(x,y) dx dy \right] \quad (B-6)$$

where $f(x,y) = (x^2+y^2)^{-3/2}$. Equation B-6 suggests computing the terrain correction by applying Eq. A.4-4 to the Fourier transforms (Eq. A.4-1) of f and h , and f and h^2 . There is a problem, however: the function $(x^2+y^2)^{-3/2}$ is not integrable over the plane and its Fourier transform does not exist. Two remedies have been suggested.

Reference 33 follows the approach of evaluating f numerically on a regular x - y grid, replacing the singularity at $x=y=0$ by zero, then computing a numerical Fourier transform (using the FFT). In addition, the nonconvergent integral appearing in the third term in Eq. B-6 was replaced by the value of the numerical transform at $u=v=0$. Obviously, this is an ad hoc remedy, and it is difficult to evaluate its effect, since a sum of infinite quantities is replaced by a sum of finite quantities.

The second remedy was suggested in Ref. 34 and also mentioned in Ref. 33. It consists of an analytic modification of f such that

$$f(x,y) = (x^2+y^2+a^2)^{-3/2} \quad (B-7)$$

where a is a constant that is chosen empirically. The modified f has the Fourier transform

$$F(u,v) = 2\pi a^{-1} e^{-2\pi a \sqrt{u^2+v^2}} \quad (B-8)$$

and

$$\iint f(x,y) dx dy = F(0,0) = 2\pi a^{-1} \quad (B-9)$$

Although it is more straightforward to implement, avoiding a numerical transform of the modified f , this remedy appears as ad hoc as the first; also there is an arbitrary constant to be chosen.

However, Eq. B-7 combined with Eq. B-6 is a better approximation to Eq. B-1 than is Eq. B-4, given a suitable choice of the constant a . The FFT algorithm for terrain effect computation is actually more rigorous than its proponents have claimed.

To understand why this is so, consider the following expressions:

$$c(x_p, y_p) \cong G\rho \iint dx dy \int_{h_p}^{h(x,y)} \frac{(z-h_p) dz}{[(x_p-x)^2 + (y_p-y)^2 + a^2]^{3/2}} \quad (B-10a)$$

$$= \frac{1}{2} G\rho \iint \frac{[h(x,y)-h_p]^2}{[(x_p-x)^2 + (y_p-y)^2 + a^2]^{3/2}} dx dy \quad (B-10b)$$

Equation B-10b is equivalent to the combination of Eqs. B-6 and B-7; Eq. B-10a is identical to Eq. B-1 except that in the denominator $(h_p-z)^2$ is replaced by a^2 . Thus, the combination of Eqs. B-6 and B-7 follows directly from the exact (flat-earth) terrain correction (Eq. B-1), given the single approximation $(h_p-z)^2 \cong a^2$. The meaning of a^2 is now clear; it represents an average value of $(h_p-z)^2$ and its optimal value always exceeds zero because $(h_p-z)^2$ is always positive.

Thus, the two stages of approximation applied in Refs. 33 and 34 are unnecessary and partially cancel one another. Truncation of the series expansion of $1/r^3$ leads to an overestimate of the terrain correction which is compensated by the fact that $(x^2+y^2+a^2)^{-3/2}$ underestimates $(x^2+y^2)^{-3/2}$.

Examples with exact analytic solutions help to illustrate and evaluate the various approximations to the flat-earth terrain correction. Two such examples are given here. The first involves the conical mountain used in Ref. 34 (pp. 46-47). The second is based on an "inner zone" of constant slope. (Note that the approximations in the integrands of Eqs. B-4 and B-10b are both most severe when r_0 is small.)

The conical mountain, with height H and slope angle θ , is illustrated schematically in Fig. B-1. The terrain correction at the summit point P is straightforward to evaluate. Placing the origin such that $x_p=y_p=0$, the height function is

$$h(x,y) = h(r_0) = \begin{cases} H - r_0 \tan \theta & r_0 \leq H/\tan \theta \\ 0 & r_0 \geq H/\tan \theta \end{cases} \quad (B-11)$$

where $r_0 = \sqrt{x^2+y^2}$. Thus, $h_p = H$. Substitution into Eq. B-1 gives the exact result

$$\begin{aligned} c_{\text{exact}} &= 2\pi G\rho \int_0^\infty r_0 dr_0 \int_H^{h(r_0)} \frac{(z-H)dz}{[r_0^2 + (H-z)^2]^{3/2}} \\ &= 2\pi G\rho H \sin \theta \end{aligned} \quad (B-12)$$

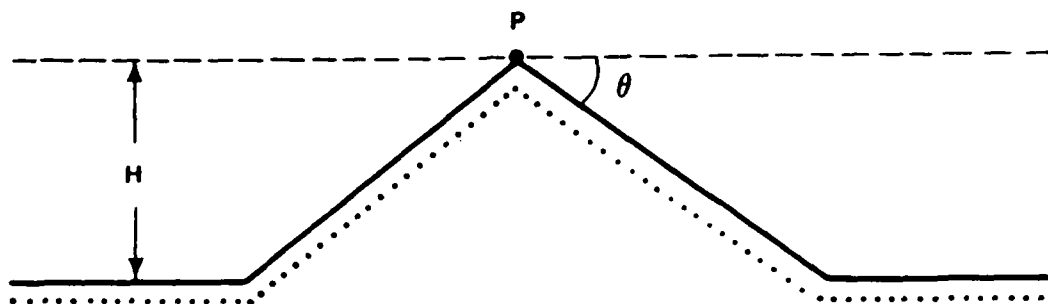


Figure B-1 Conical Mountain

(as shown in Ref. 34, Eq. 7.24). On the other hand, substitution into Eq. B-10b yields the approximate terrain correction

$$\begin{aligned}
 c_{\text{approx}}(a) &= \pi G \rho \int_0^{\infty} \frac{[h(r_o) - H]^2}{[r_o^2 + a^2]^{3/2}} r_o dr_o \\
 &= 2\pi G \rho \tan \theta [(H^2 + a^2 \tan^2 \theta)^{1/2} - a \tan \theta]
 \end{aligned}
 \tag{B-13}$$

which is a function of the parameter a . Substitution of $h(x,y)$ into Eq. B-4 is equivalent to setting $a=0$,

$$c_{\text{approx}}(0) = 2\pi G \rho H \tan \theta \tag{B-14}$$

in agreement with Eq. 7.25, Ref. 34.

As pointed out earlier, the optimal value of a^2 exceeds zero. In fact, for the single point P , a may be chosen such that $c_{\text{approx}}(a) = c_{\text{exact}}$. By solving the equation

$$\tan \theta [(H^2 + a^2 \tan^2 \theta)^{\frac{1}{2}} - a \tan \theta] = H \sin \theta \quad (B-15)$$

for a , one finds $a = H (\sin \theta)/2$. Of course, setting $a = H (\sin \theta)/2$ in Eq. B-10b probably would not lead to exact results for points on the flank of the cone, or on the surrounding plain, but the point is that a range of nonzero values of a does better than $a=0$. Furthermore, for the summit point P, one can derive an upper bound of that range by setting the underestimate of the terrain correction incurred by using $c_{\text{approx}}(a)$ equal to the overestimate incurred using $c_{\text{approx}}(0)$:

$$c_{\text{exact}} - c_{\text{approx}}(a) = c_{\text{approx}}(0) - c_{\text{exact}}$$

$$H \sin \theta - \tan \theta [(H^2 + a^2 \tan^2 \theta)^{\frac{1}{2}} - a \tan \theta] = H \tan \theta - H \sin \theta$$

$$a = \frac{2H \cos^2 \theta (1 - \cos \theta)}{\sin \theta (2 \cos \theta - 1)} \quad (B-16)$$

Table B-1 presents the computed values of these results for several values of θ .

TABLE B-1
CONICAL MOUNTAIN EXAMPLE

θ	BEST a	UPPERBOUND ON a
Small θ (in radians)	$\frac{1}{2}\theta H$	θH
15 deg	0.13H	0.26H
30 deg	0.25H	0.55H
45 deg	0.35H	H

The table indicates, for instance, that for $\theta = 30$ deg $c_{\text{approx}} = c_{\text{exact}}$ if $a = 0.25H$ and any value of a between 0 and $0.55H$ yields a better approximation than does $a = 0$.

Another straightforward example can be developed by considering the inner zone in which r_o is small enough to allow the approximation of the terrain correction by its first-order Taylor expansion. This is the region where the approximations to $1/r^3$ have the greatest effect. Consider the case where $0 \leq r_o \leq R$ and

$$x_p = y_p = 0$$

$$h(x,y) = h(r_o, \phi) = h_p + S r_o \cos \phi$$

(B-17)

where $x = r_o \cos \phi$ and $y = r_o \sin \phi$. This defines a circular zone of constant slope S with its gradient directed (arbitrarily) in the x -direction. From Eq. B-1, the exact terrain correction due to this zone is

$$\begin{aligned} c_{\text{exact}} &= G\rho R \int_0^{2\pi} [1 - (1 + S^2 \cos^2 \phi)^{-\frac{1}{2}}] d\phi \\ &= \frac{\pi}{2} G\rho S^2 R \left(1 - \frac{9}{16} S^2 + \dots \right) \end{aligned} \quad (\text{B-18})$$

Equation B-10 yields

$$\begin{aligned} C_{\text{approx}}(a) &= \frac{\pi}{2} G \rho S^2 [(R^2 + a^2)^{\frac{1}{2}} + a^2 (R^2 + a^2)^{-\frac{1}{2}} - 2a] \\ &= \frac{\pi}{2} G \rho S^2 R (1 - 2 \frac{a}{R} + \dots) \end{aligned} \quad (\text{B-19})$$

and setting $a = 0$ or applying Eq. B-4 yields

$$C_{\text{approx}}(0) = \frac{\pi}{2} G \rho S^2 R. \quad (\text{B-20})$$

Clearly, the approximate solution can be closely matched to the exact by choosing $a = \frac{9}{32} S^2 R$ while for a slope corresponding to 30 degrees, $c_{\text{approx}}(0)$ includes an error of almost 20%.

The analytic examples presented here complement the numerical example given in Chapter 5, and along with details of the new derivation reaffirm the conclusions that the FFT terrain correction algorithm is more rigorous than claimed by its proponents and that the optimal value of the parameter a always exceeds zero.

APPENDIX C
ANALYSIS OF TERRAIN EFFECTS USING
WHITE SANDS DATA

C.1 INTRODUCTION

In a region of high relief such as the White Sands study area, it is important to include the effects of terrain in the prediction of gravity anomaly or deflections of the vertical from gravity anomaly observations. The research described in this appendix addresses the quantitative determination of the importance of terrain effects, including dependence on wavelength, variation with terrain type, and the orientation of prominent terrain and gravity features. This complements the work of the IAG Study group (Refs. 20, 21) on algorithms for prediction of gravity disturbance and deflection of the vertical.

The investigations documented in this appendix are summarized for quick overview in Fig. C.1-1. They include two distinct studies. One of these, as outlined in the upper half of Fig. C.1-1, makes use of spectral techniques to examine and compare observed free-air gravity anomalies and computed topographic effects for two types of terrain -- mountain and plateau -- and for two profile orientations -- east-west and north-south. The methodology and conclusions of this study are the subject of Sections C.2, C.3, and C.4 of this appendix.

The second study, outlined in the lower half of Fig. C.1-1, examines how well deflections of the vertical can be predicted from local topographic data, supplemented by a

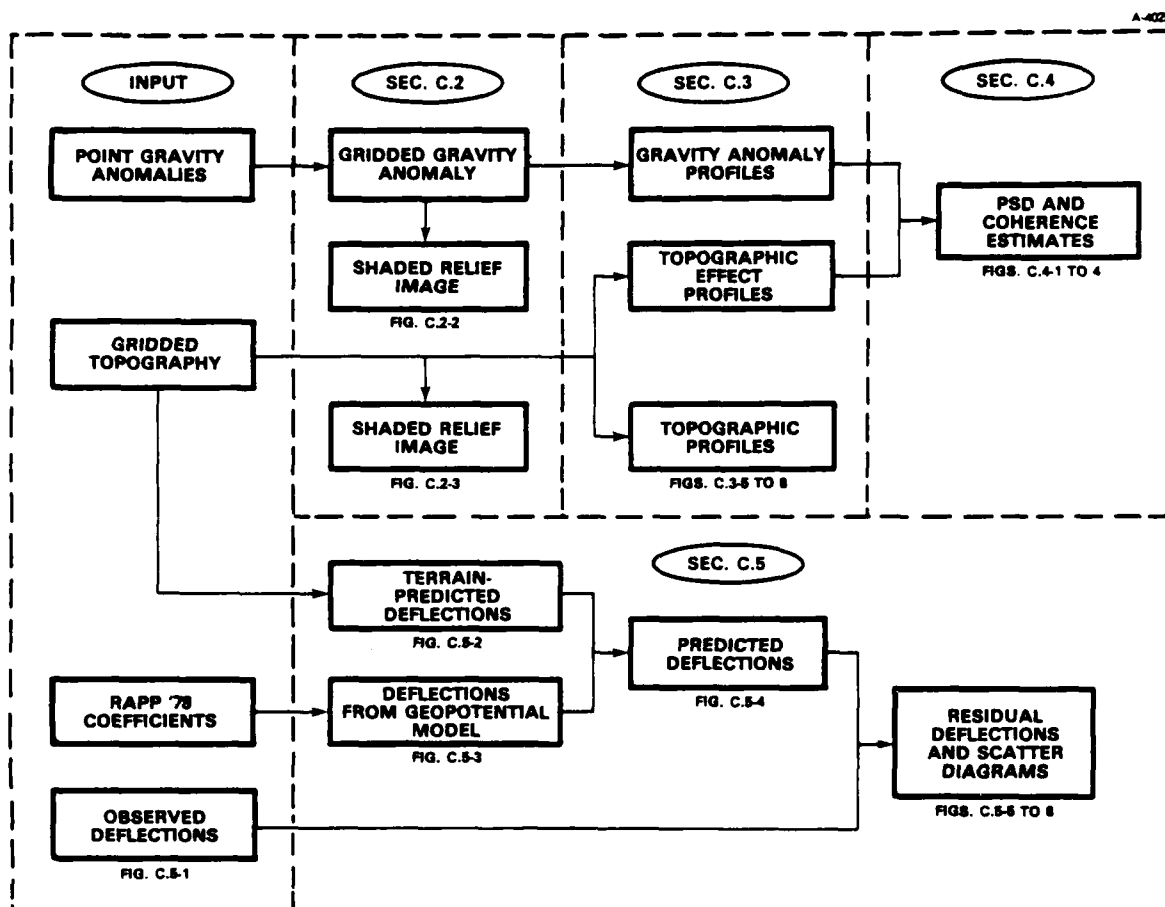


Figure C.1-1 Overview of Terrain Effects Analysis

long-wavelength component derived from a global geopotential model. This study is described in Section C.5 of the appendix.

The first step in the spectral studies, described in Section C.2, is to grid and display the free-air gravity anomaly data over a 3 deg by 3 deg portion of the White Sands area, and to display gridded topographic elevations over the same 3 deg by 3 deg area. Six profiles of gravity and topography are selected from these data sets and gravity effects due to topography are computed for each profile using a particular point-mass algorithm which is described and illustrated in

Section C.3. Section C.4 describes the estimation of power spectral densities and the coherence between free-air gravity and the topographic effect from selected subsets of the profiles (sorted by terrain type and profile orientation) by means of state-space modeling, and includes illustration and analysis of the results. (This satisfies the need for spectral analysis indicated by K.P. Schwarz in the 1983 Study Group Report (Ref. 20).)

In the second study, the point mass algorithm of Section C.3 is applied to predict the topographic contributions to the deflections of the vertical at each of the astrogeodetic truth data locations. Using these predictions, bounds are placed on the significance of the topographic effect. The astrogeodetic data are too sparse to support the use of gridding followed by state-space modeling like that applied to the gravity data.

C.2 GRIDDED GRAVITY AND TOPOGRAPHIC DATA

Gravity data were supplied in the form of free-air point gravity anomaly measurements unevenly distributed over a 5.5 by 5.5 deg area (Ref. 20). A 3 by 3 deg subset of this area extending from 32 to 35 deg North and 105 to 108 deg West was selected for this study. This subset was selected because it contained a relatively dense concentration (3855 points) of gravity observations and was also covered by digital gridded topographic data. Figure C.2-1 shows a map of the locations of the 3855 gravity measurements used in this study.

In order to perform spectral analysis of free-air point gravity measurements, it is necessary to grid the data. A 121 by 121 grid (40 grid intervals per degree) is computed over

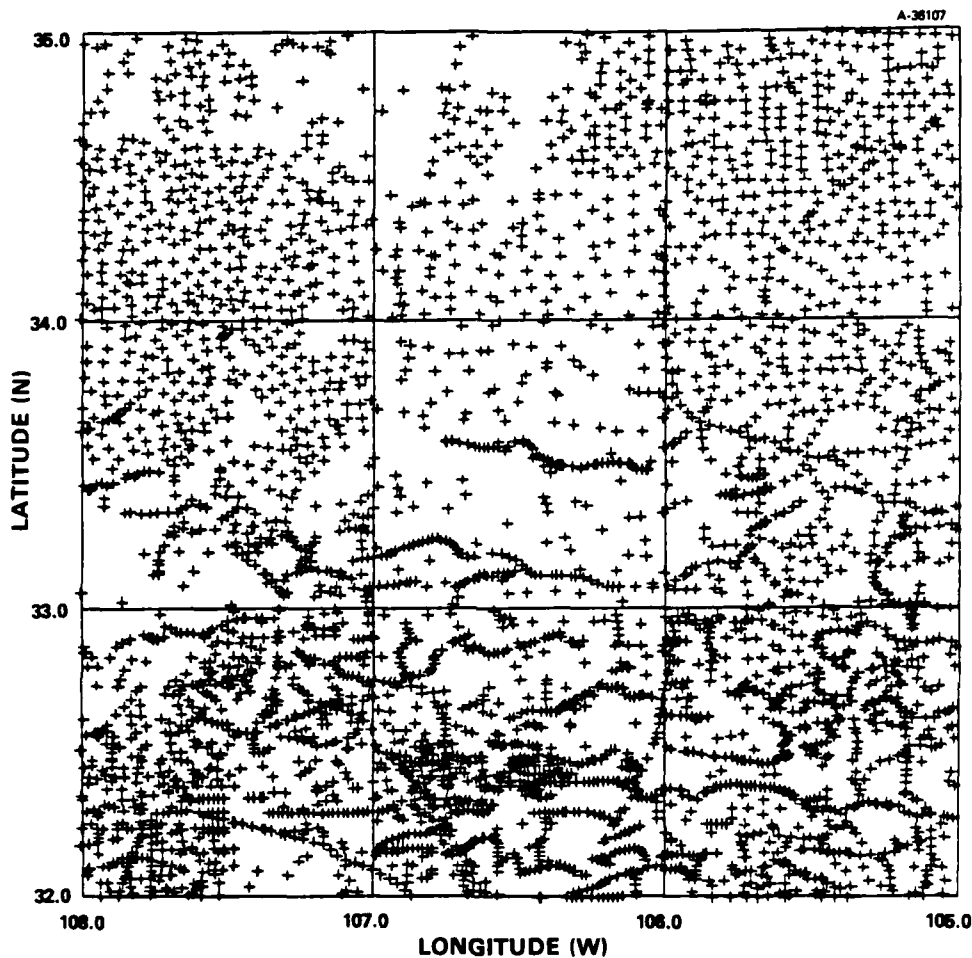


Figure C.2-1 Locations of Free-Air Gravity Anomaly Points in the Study Area

the study area using the Barnes analysis scheme (Ref. 42). The gridding algorithm consists of a computationally simple, Gaussian weighted-averaging technique which assigns a weight to a datum solely as a function of distance between datum and grid point.

Figure C.2-2 is a color shaded-relief image of the 3 by 3 deg free-air gravity anomaly grid. The magnitudes of the

WHITE SANDS FREE-AIR GRAVITY

35 N

1000

105



100



32 N

108 W

105 W

TASC

gravity values range from approximately -60 to 165 mgals, and are indicated by hue, as shown on the scale bar. Shading is included to enhance short-wavelength features in the data. The shading is computed using a southeast-to-northwest directional derivative.

The gridded topographic data covering the 3 by 3 deg study area are shown as a color, shaded-relief image in Fig. C.2-3. The sampling interval of the topographic data is 120 samples per degree (a 360 by 360 grid). This grid sampling is three times as dense as the sampling interval of the gridded gravity and accounts for the greater sharpness of the topography image. The scale bar provides a conversion between hue and elevation as in the gravity image. The shading is based on a directional derivative simulating illumination from the southeast.

C.3 PROFILES OF ANOMALIES AND TOPOGRAPHIC CORRECTIONS

Three types of profiles are discussed in this section: free-air gravity anomaly profiles, topographic effect profiles, and residual anomaly profiles. The free-air gravity anomaly profiles are taken along rows or columns of the free-air gravity anomaly grid. Topographic effect profiles consist of gravity disturbance values computed from an algorithm which is discussed below. The residual anomaly profiles result from subtracting topographic effect profiles from the corresponding free-air gravity anomaly profiles.

An algorithm which computes the vertical component of the gravity disturbance from topographic data was used to compute the topographic effect profiles. Figure C.3-1 illustrates the essential elements of this algorithm. The topographic

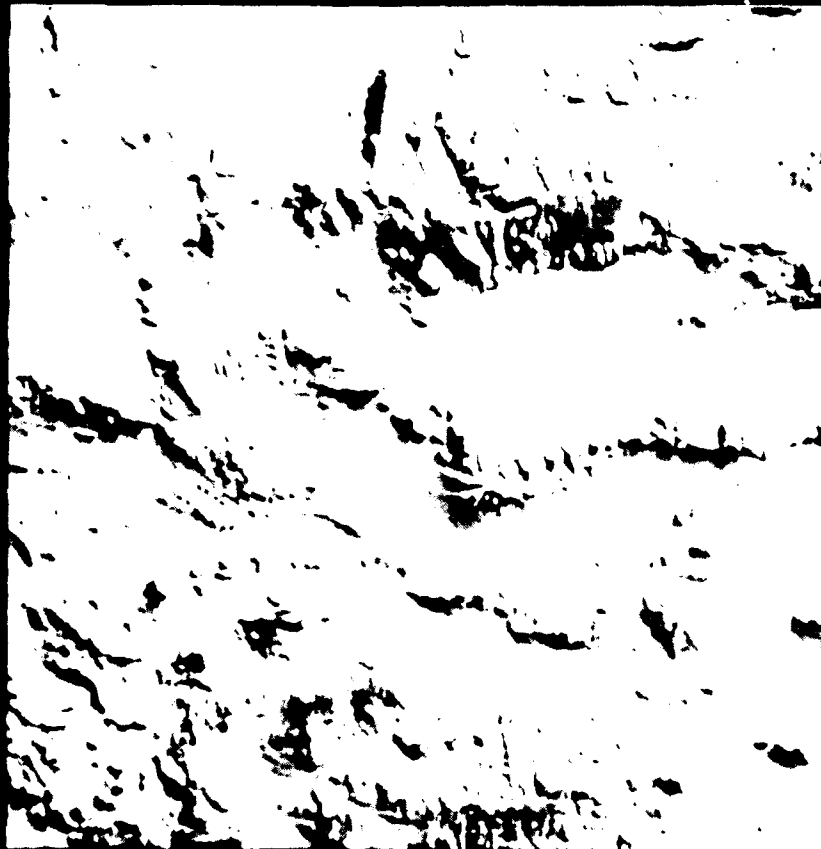
WHITE SANDS TOPOGRAPHY

35 N

Elev
2000 m



1000 m



32 N

108 W

105 W

TASC

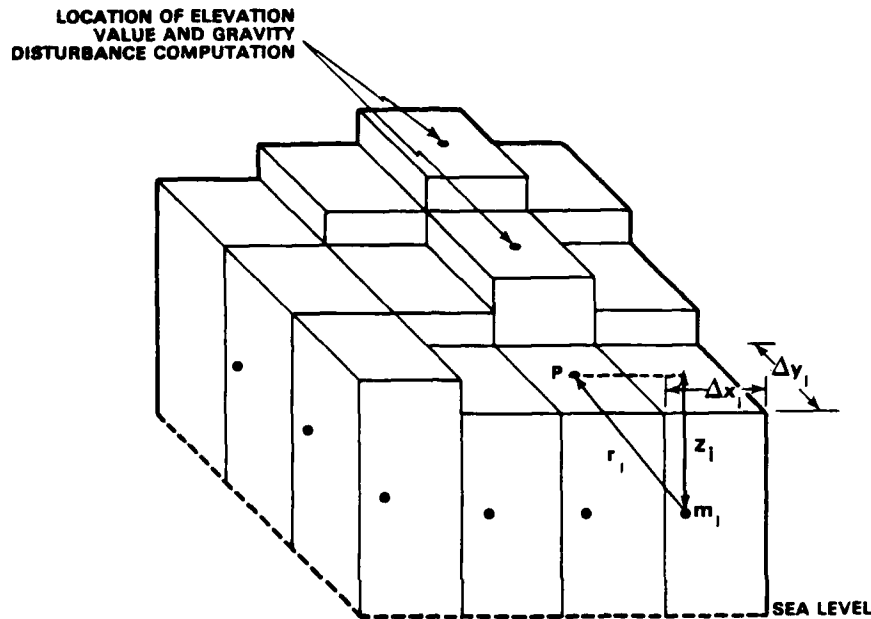


Figure C.3-1 Pictorial Representation of Gravity Disturbance Computation

data are treated as a grid of vertical rectangular prisms extending upward from sea level. The mass of each prism is computed by multiplying the volume times the density, and is considered to be a point mass located at the center of each prism. The vertical component of the gravity disturbance at P (see Fig. C.3-1) is then computed by summing the point masses over a square window as follows:

$$\delta g_p = \sum_{i=1}^{w^2} \frac{Gm_i}{r_i^2} \times \frac{z_i}{r_i} \quad (C.3-1)$$

where

δg_p = the vertical component of the gravity disturbance at point P

w = window width

m_i = mass of each prism

G = gravitational constant

$$r^2 = x^2 + y^2 + z^2$$

The disturbance values closely approximate the complete Bouguer correction because both slab and terrain effects are taken into account by setting sea level as the lower boundary of the prisms.

The profile sampling density for the topographic effect equals that of the gridded topography, 120 points per degree. In order to match the point locations and sampling density of the free-air gravity anomaly profiles (40 points per degree), the profile data series are averaged and subsampled using a three-point moving window.

Once the free-air gravity anomaly profiles and topographic effect profiles consist of identical point locations and spacing, it becomes possible to take the difference between the two, forming the residual anomaly profiles.

A total of six profile locations are selected to cover a variety of terrain types. Figure C.3-2 shows the profile locations superposed on a contour map of the White Sands topography. Three profiles run east-west, and are labeled EW-1, -2 and -3, and three run north-south, and are labeled NS-1, -2, and -3.

At each of the profile locations shown in Fig. C.3-2, the free-air gravity anomaly, topographic effect and residual anomaly profiles are computed. These three profile types, along with terrain elevation profiles, are plotted for each location and are shown in Figs. C.3-3 through C.3-8. Subsets

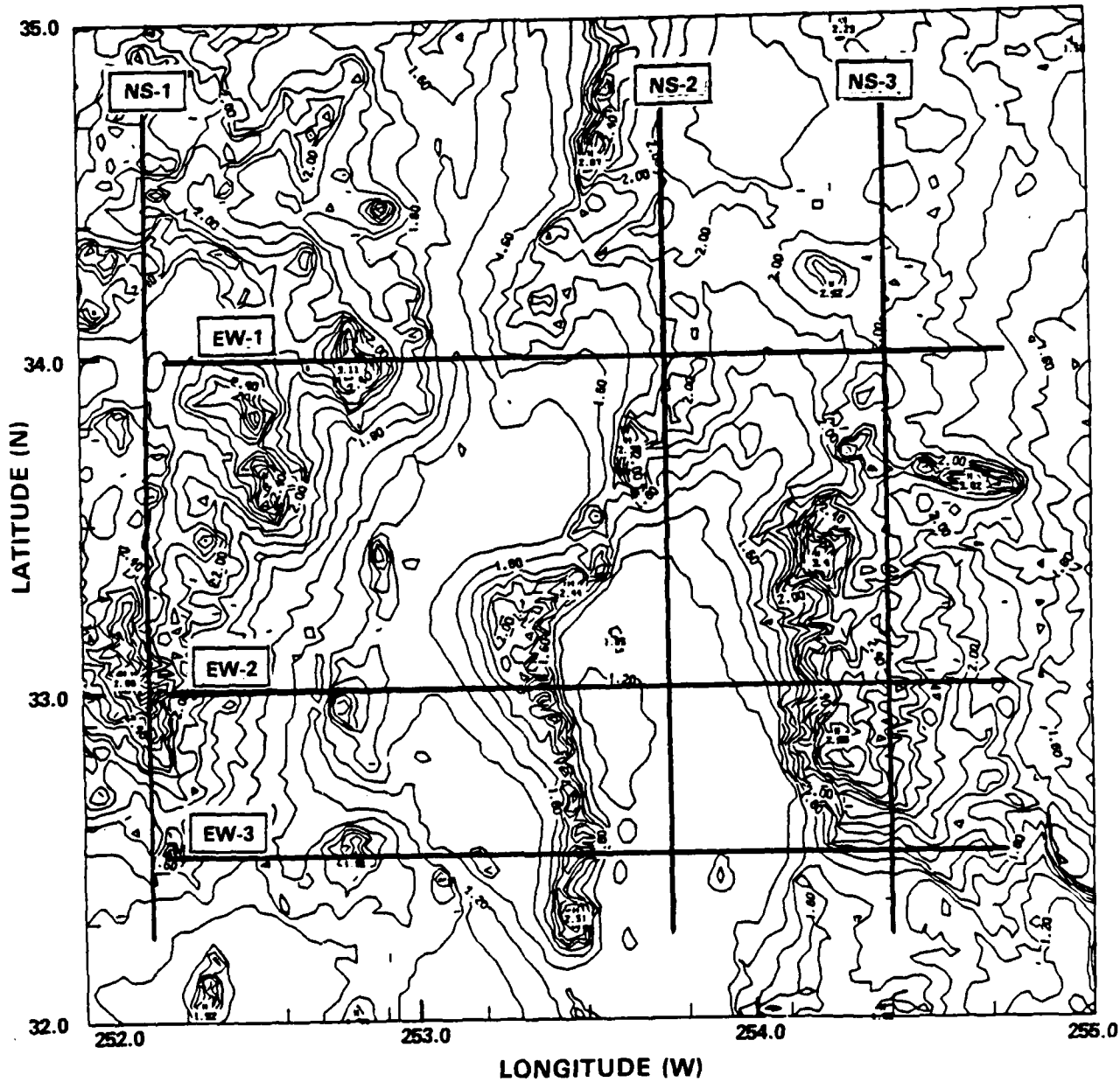


Figure C.3-2 Map of Profile Locations

THE ANALYTIC SCIENCES CORPORATION

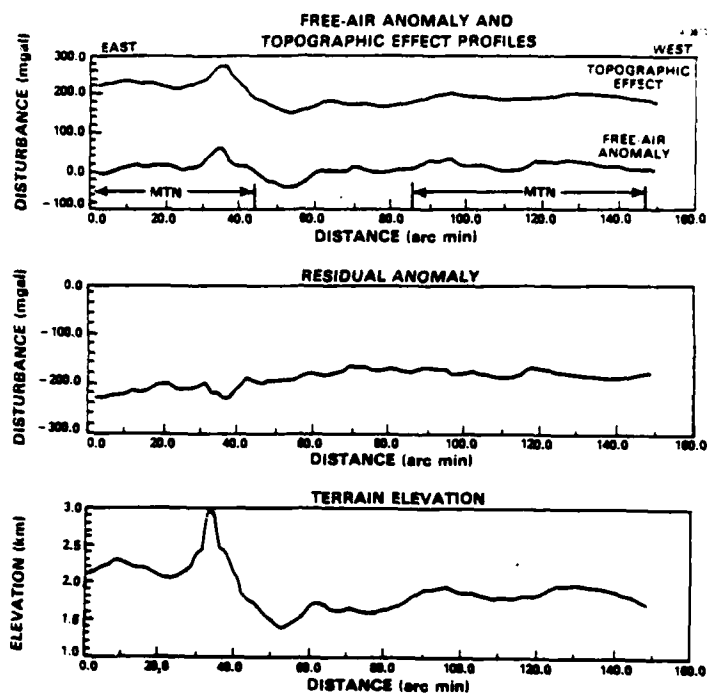


Figure C.3-3 Profile EW-1

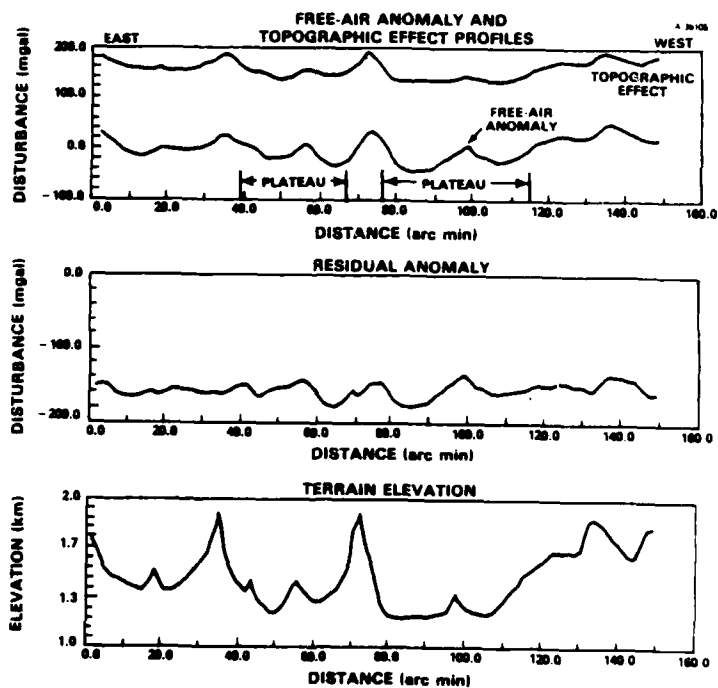


Figure C.3-4 Profile EW-2

THE ANALYTIC SCIENCES CORPORATION

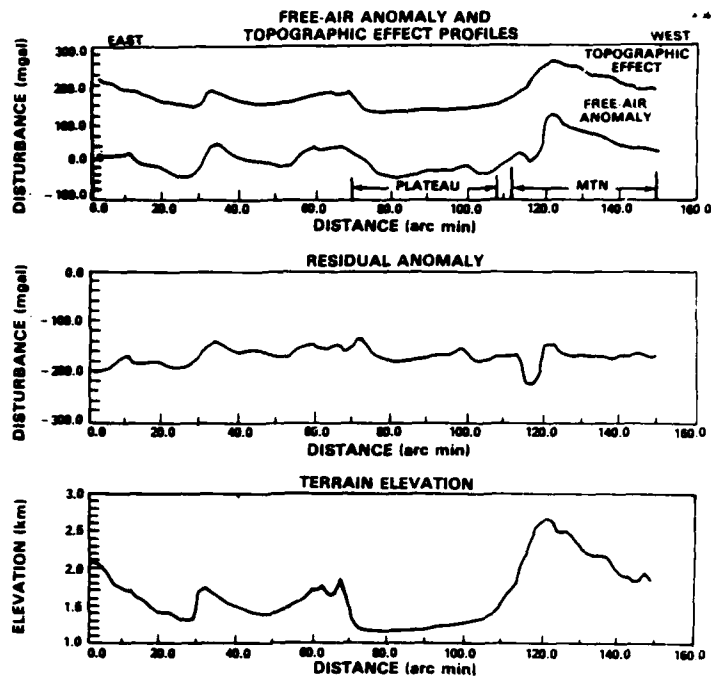


Figure C.3-5 Profile EW-3

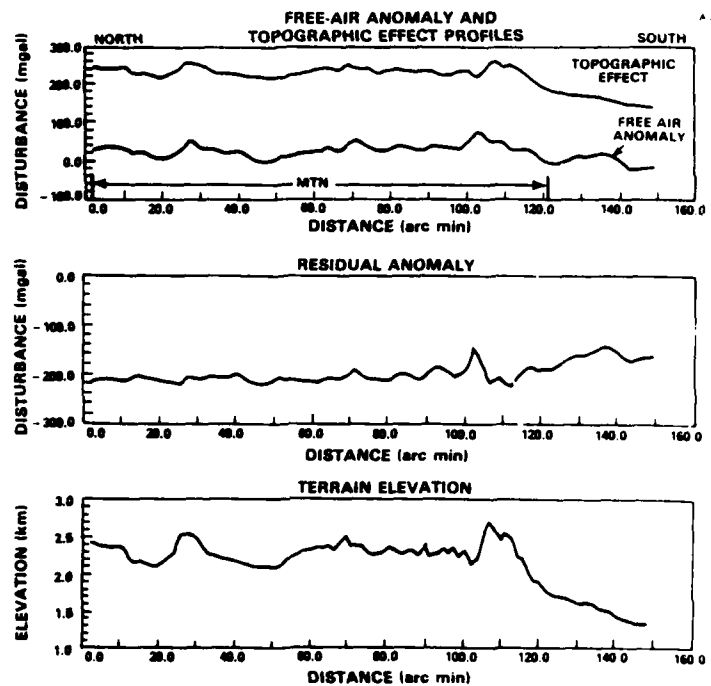


Figure C.3-6 Profile NS-1

THE ANALYTIC SCIENCES CORPORATION

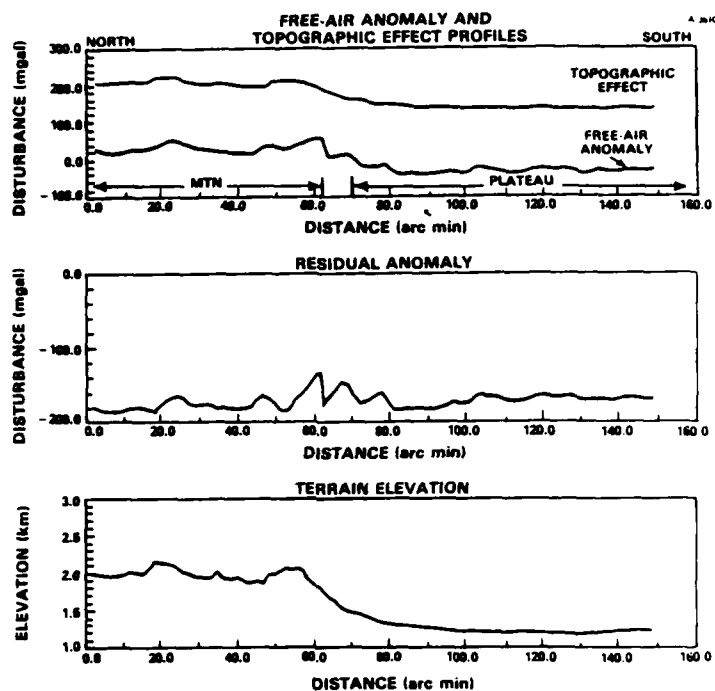


Figure C.3-7 Profile NS-2

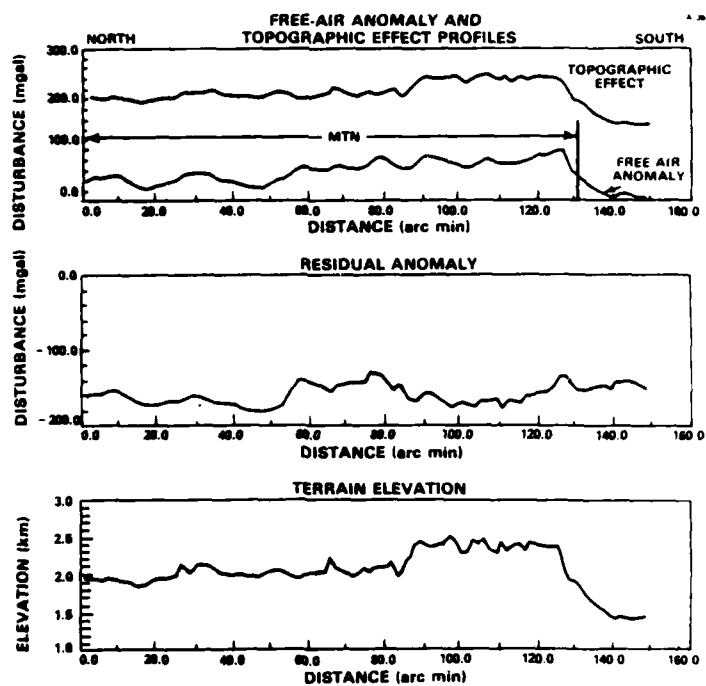


Figure C.3-8 Profile NS-3

of mountainous- and plateau-type terrains are also indicated on these plots. The predominantly negative values of the residual anomalies are consistent with regional Bouguer gravity for the southwestern U.S. (Ref. 43).

The next section of this appendix presents further discussion and interpretation of these profiles in terms of power spectral densities and spectral coherences, derived using modern state-space estimation techniques.

C.4 POWER SPECTRAL DENSITIES OF PROFILES

Segments of data representing mountainous- and plateau-type terrains are selected from the six profiles shown in Fig. C.3-2. The actual segments used are indicated on the profile plots in Figs. C.3-3 through C.3-8. The criterion used to classify the terrain into these two types defines elevations above 1750 m being defined as mountainous, and elevations below 1500 m as plateau.

The purpose of the spectral analysis of these profile segments is to determine spectral differences between terrain types and to determine the extent to which directional (east-west versus north-south) anisotropy exists. In order to make these spectral comparisons, the data segments are pooled into four groups: 1) east-west plateau, 2) north-south plateau, 3) east-west mountain, and 4) north-south mountain. Power spectra for each of the four groups are computed by state-space modeling, as described below.

A method of state-space modeling (Ref. 44) is used to produce the power spectral density (PSD) estimates discussed in this section. This method consists of two steps. First, a

model is developed for the data series using a canonical-variates (CV) technique. The CV technique produces a family of optimal state-space models by solving a finite number of linear equations for the state-space model parameters. In the second step, the power spectrum of the model is computed. Once the model parameters are computed, many statistical analyses may be performed, including an analysis of coherence between the data series. This state-space modeling method is advantageous for our purposes because it allows multiple tracks of data to be pooled for spectrum estimates that are limited by the total extent of the data, rather than the lengths of the individual track segments.

Figures C.4-1 through C.4-4 show power spectral density (PSD) plots of free-air gravity anomaly, topographic effect, and residual anomaly for each of the four groups of data: east-west plateau, north-south plateau, east-west mountain, and north-south mountain. Coherence between the topographic effect and free-air gravity anomaly data series is also plotted for each of the four data groups.

C.4.1 Discussion of Results

As noted above, the selected data segments representing mountainous- and plateau-type terrains in east-west and north-south profile orientations are pooled into four distinct groups. The various PSDs estimated from these four groups are discussed below.

East-west Plateau - The data segments used to form this pool consist of two segments from profile EW-2 (Fig. C.3-4) and one segment from profile EW-3 (Fig. C.3-5). Figure C.4-1 shows the PSDs for the free-air gravity anomaly, topographic effect, and residual anomaly. The PSD plot shows that at all

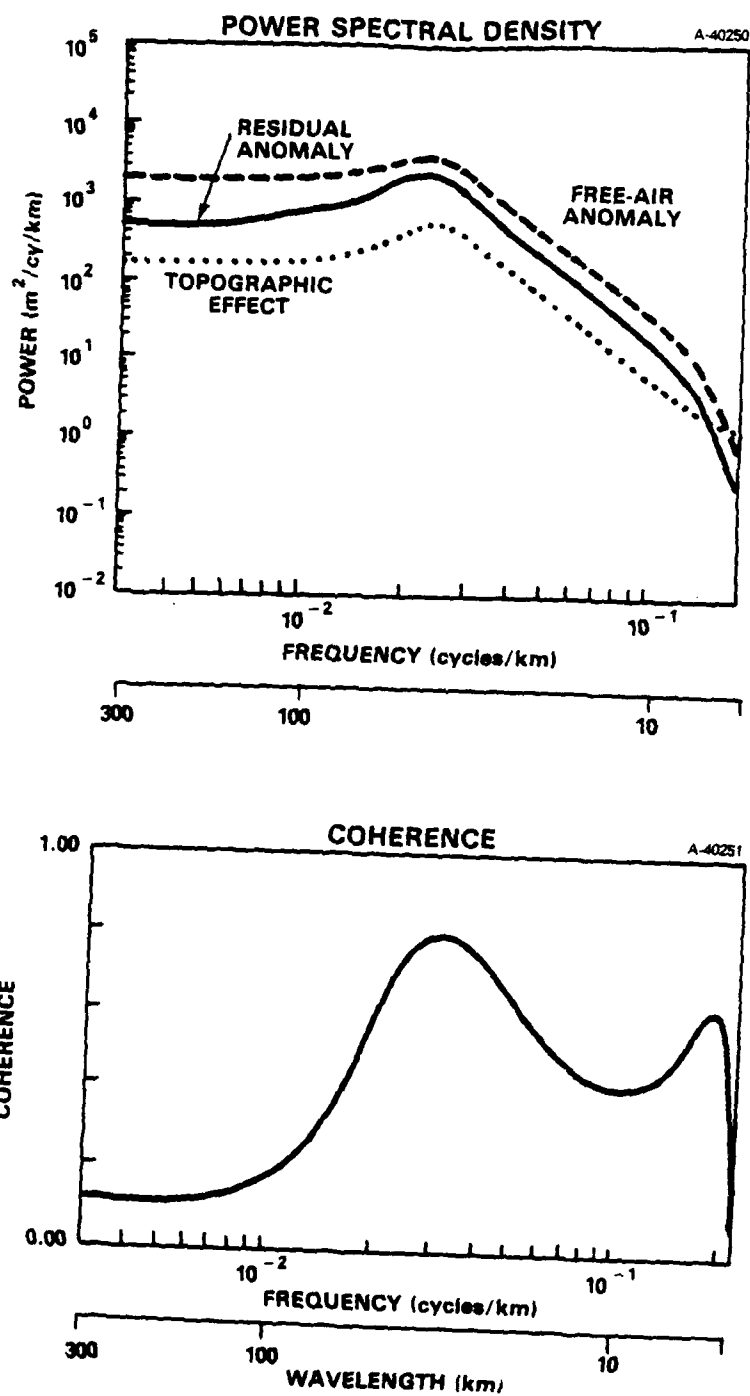


Figure C.4-1 East-West Plateau Terrain

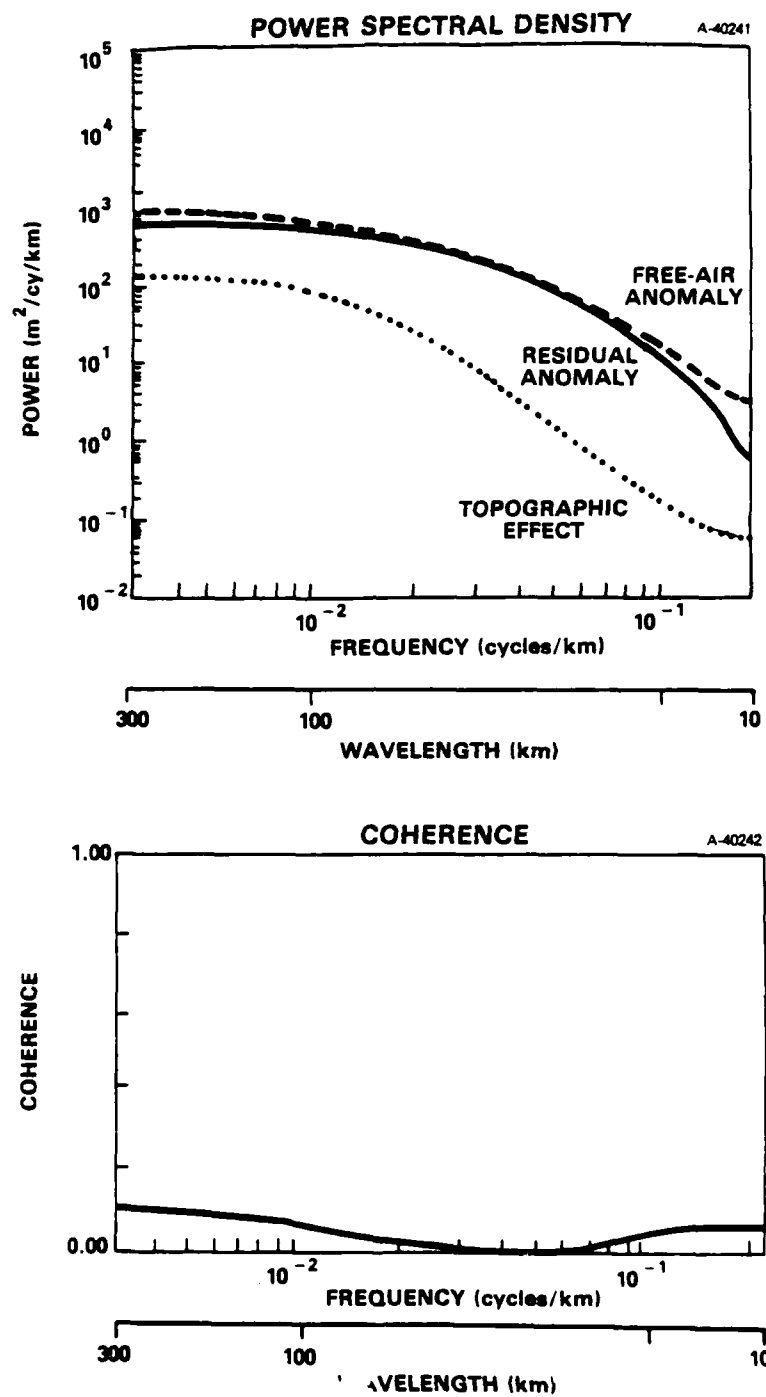


Figure C.4-2 North-South Plateau Terrain

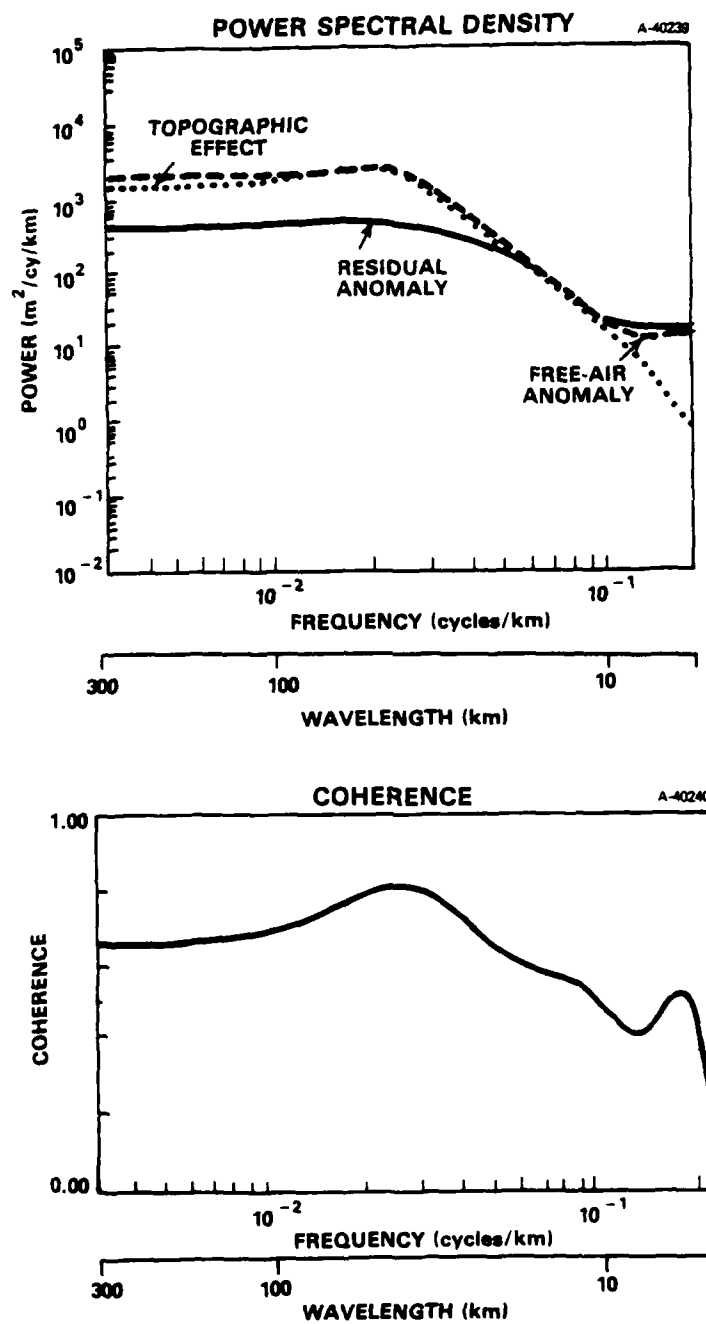


Figure C.4-3 East-West Mountainous Terrain

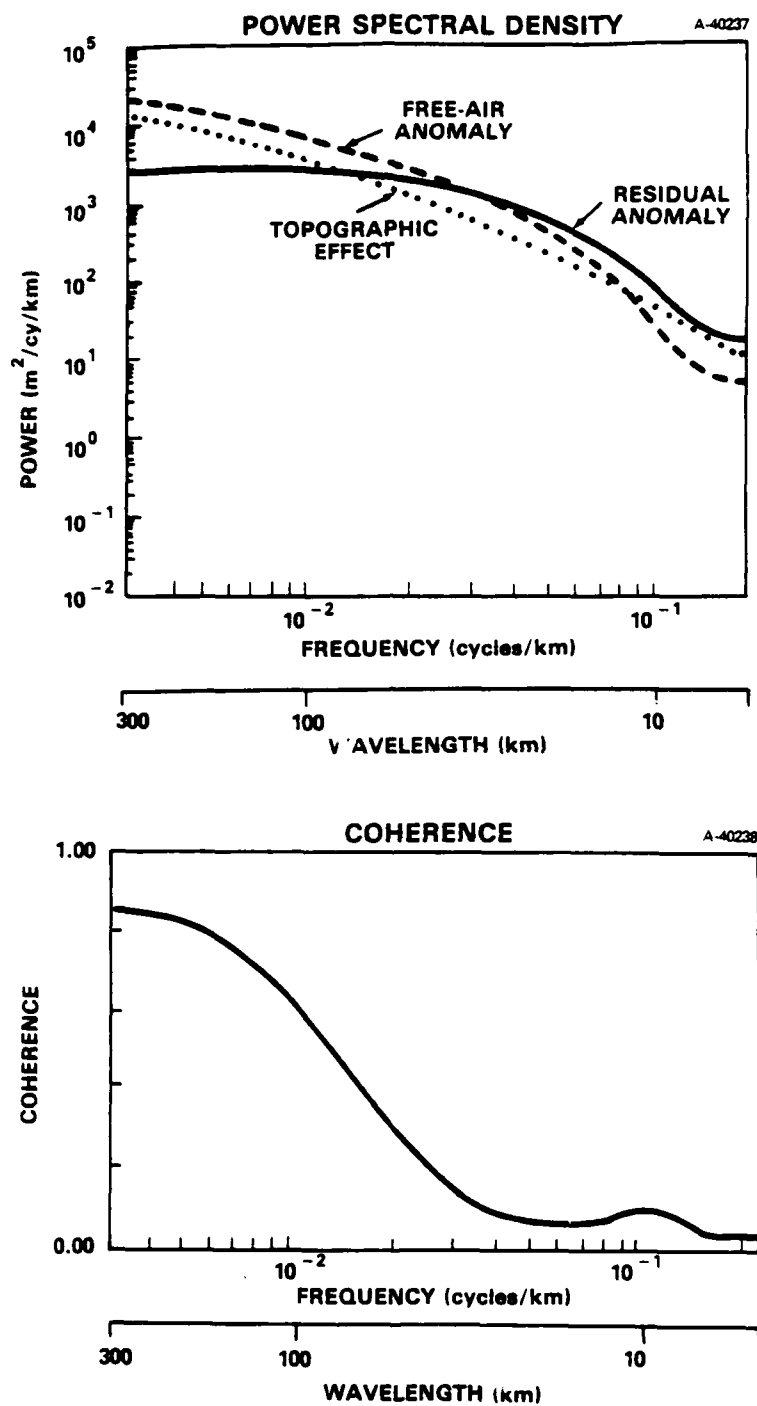


Figure C.4-4 North-South Mountainous Terrain

frequencies, the topographic effect has less power than the free-air gravity anomaly or residual anomaly. A local peak in power at 40 km wavelength is seen in all three PSDs. This peak may be due to the large north-south-trending geologic features crossing the White Sands study area (see Figs. C.2-2 and C.2-3).

The plot of coherence between free-air gravity anomaly and topographic effect data series shows that there is low coherence at longer wavelengths (>60 km) and higher coherence at shorter wavelengths, particularly in the region of the local peak of power. The sudden drop in coherence near the folding frequency is due to the finite sample spacing and is not of geophysical significance.

North-south Plateau - The data segment used for the north-south plateau group is from profile NS-2 (Fig. C.3-7). The plot of the three PSDs (Fig. C.4-2) shows that the topographic effect has very low power. Subtraction of the topographic effect from the free-air gravity anomaly does not significantly change the amount of power in the gravity anomaly PSD; terrain plays a very minor role in this case. The coherence between the free-air gravity anomaly and topographic effect PSD is extremely low at all frequencies.

East-west Mountain - The data segments used to form this group are from two segments of profile EW-1 (Fig. C.3-3) and one segment of profile EW-3 (Fig. C.3-5). Examination of the PSD plot (Fig. C.4-3) shows a local peak in power similar to that observed in the E-W plateau group. Unlike the E-W plateau group, though, the peak appears only in the topographic effect and free-air gravity anomaly PSDs, and is absent in the residual anomaly PSD. Since the free-air and topographic effect PSDs track each other very well, much of the power in the

free-air gravity anomaly data is due to terrain. A large decrease in the amount of power of all three PSDs at short-wavelengths is also observed.

The peak in coherence corresponding to the PSD power peak is located at a wavelength of about 40 km, similar to the coherence plot in Fig. C.4-1. The coherence between free-air gravity anomaly and topographic effect is fairly high at most frequencies; therefore, along these profiles most of the gravity signal reflects topography directly.

North-south Mountain - The data segments used to form this group consist of one segment from profile NS-1 (Fig. C.3-6), one segment from NS-2 (Fig. C.3-7), and one segment from NS-3 (Fig. C.3-8). Figure C.4-4 shows the three PSDs computed for this group. The power in all three PSDs rolls off (decreases) with a decrease in wavelength. The coherence begins to decrease sharply in the vicinity of this roll-off of power. At long wavelengths (>100 km) there is high coherence; at shorter wavelengths, the coherence drops off dramatically.

C.4.2 Conclusions

The PSD and coherence results of the preceding section are presented in Table C.4-1. These results strongly reflect the anisotropy in the terrain: east-west profiles show higher correlation between terrain and free-air gravity anomaly than north-south profiles. This is because the predominant structural features of the terrain (mountain ridges and valleys) run north-south. The correlation is strongest at wavelengths between 25 and 50 km.

This conclusion reinforces the importance of removing terrain effects before applying collocation techniques. The

TABLE C.4-1
COMPARISON OF MOUNTAIN AND PLATEAU REGIONS IN NORTH-SOUTH
AND EAST-WEST DIRECTIONS

DATA TYPE	FREE-AIR GRAVITY ANOMALY		TOPOGRAPHIC EFFECT		RESIDUAL ANOMALY		SQUARED COEFFICIENT CORRECTION
	RMS (mgal)	-3dB WAVELENGTH (km)	RMS (mgal)	-3dB WAVELENGTH (km)	RMS (mgal)	-3dB WAVELENGTH (km)	
East-West Plateau	16.3	23	6.0	17	12.0	19	0.33
North-South Plateau	5.8	65	2.0	100	5.6	50	0.05
East-West Mountain	13.2	25	13.6	25	7.2	20	0.67
North-South Mountain	21.5	200	16.4	200	12.9	36	0.62

need to do this is obvious for mountainous areas; it was pointed out by the IAG study group. The present results, however, indicate that even in plateau areas, where the topographic contribution to free-air gravity anomaly is small, there is substantial correlation between topography and gravity anomaly for the east-west tracks. Hence, for such areas, it will be worthwhile to compensate for possible anisotropy by applying terrain-remove-and-restore techniques before carrying out collocation or other estimation procedures.

C.5 TERRAIN EFFECTS ON DEFLECTIONS OF THE VERTICAL

A control data set containing 441 astrogeodetic observations of deflections of the vertical was provided in the IAG SSG C.70 test data set, version 1a (Ref. 20). These data are located primarily in the central region of the 3 deg by 3 deg study area (32 deg to 35 deg North and 105 deg to 108 deg West). Because the data are not dense enough to support the computation of a regular grid, the spectral analysis method used in the previous section is not feasible. The present analysis examines

the prediction of the irregularly spaced astrogeodetic deflections as the sum of a short-wavelength component (computed directly from the terrain height data using a point-mass algorithm) and a long-wavelength component derived from a global geopotential model. An improved prediction method can include contributions from measured gravity anomaly data, using algorithms such as Vening Meinesz integration or least-squares collocation (Appendix A; Refs. 20 and 21), although here, as in Section C.1, the terrain contribution is emphasized.

C.5.1 Discussion of Results

Figure C.5-1 shows the 441 observed deflections of the vertical used in this analysis. In this figure, the arrows indicate the direction and magnitude of the deflection, with the location of the deflection station shown at the tail of the plotted vector. It is important to note that the east components of the deflections of the vertical are opposite in sign to those plotted in the most recent IAG study group report (Ref. 21, Fig. 1.6, p. 11). Earlier work (Ref. 18, Fig. 10, p. 7852) showed a subset of the observed data with the east components of the deflections of the vertical in agreement with those shown in Fig. C.5-1. Investigation of this discrepancy has revealed that the data set distributed on tape is erroneous. The east component of the deflection of the vertical (η) is generally much larger than the north component (ξ), largely as a result of the north-south trending topographic features present in the study area.

The point-mass algorithm used to predict gravity disturbance (see Eq. C.3-1) is modified to permit computation of the north and east components of the deflections of the vertical. Using the gridded topographic data described in Section C.2, the point-mass algorithm is applied to compute

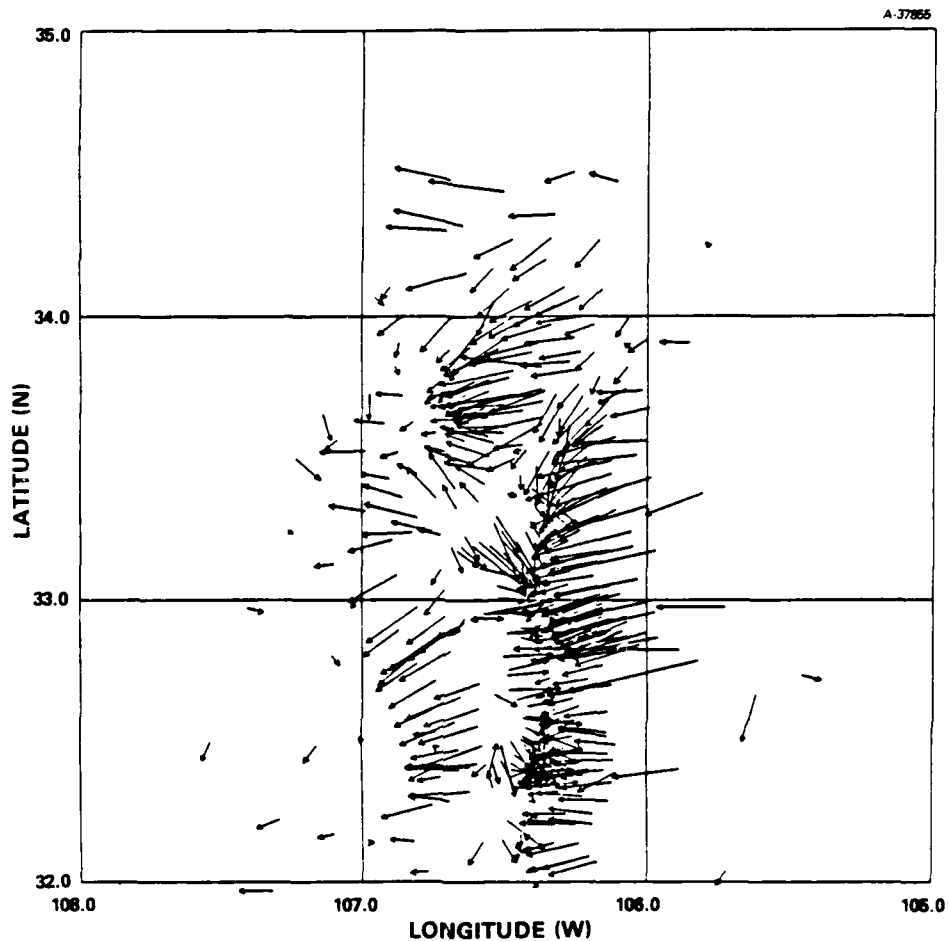


Figure C.5-1 Observed Deflections of the Vertical

deflection values at each of the 441 observed data locations. The resulting terrain-predicted deflections of the vertical are shown in Fig. C.5-2. These values represent a significant portion of the short-wavelength component of the observed deflections of the vertical.

Figure C.5-3 displays deflections of the vertical computed from Rapp's 1978 (Ref. 37) set of geopotential coefficients to degree and order 180, at the observed data locations. TASC-developed software is used to perform a spherical harmonic

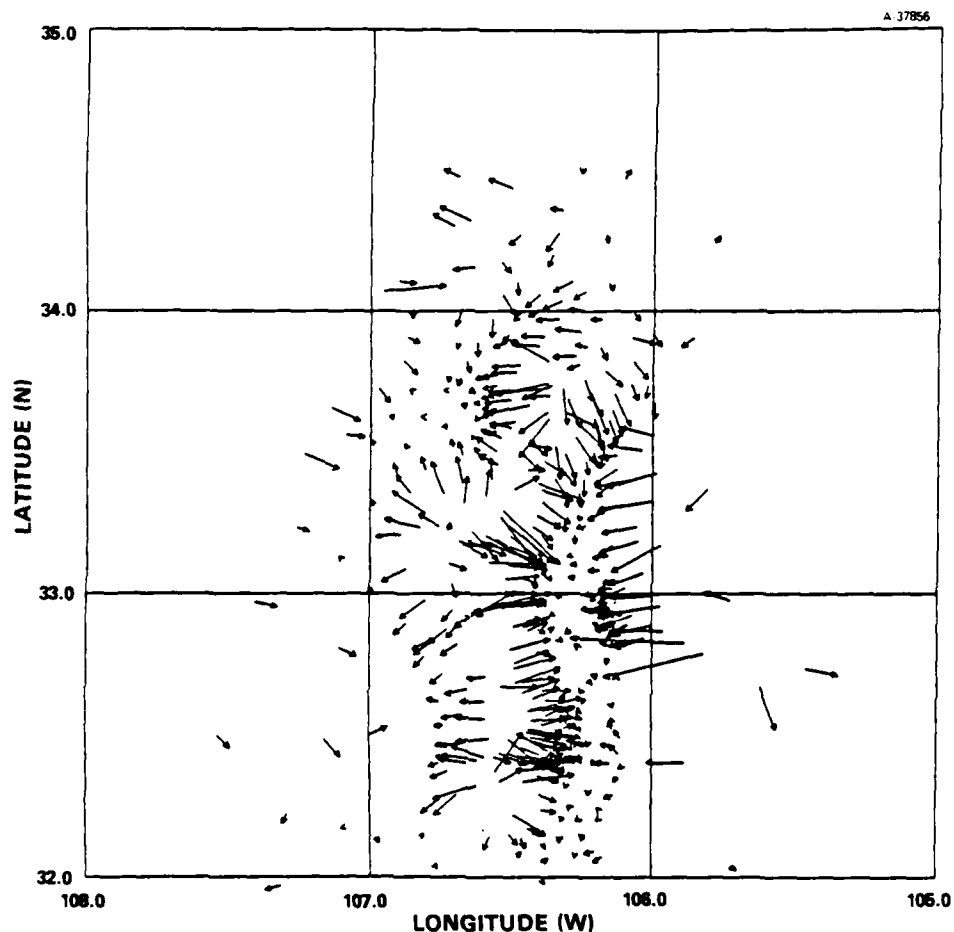


Figure C.5-2 Terrain-Predicted Deflections of the Vertical

expansion of the coefficients and evaluate the deflection components on a regular grid in colatitude and longitude (Ref. 45). The deflections predicted from the geopotential model are fairly constant in both magnitude and direction; they approximate the mean of the observed deflections.

The long-wavelength contribution predicted by the Rapp 1978 model was compared with two other prediction models:

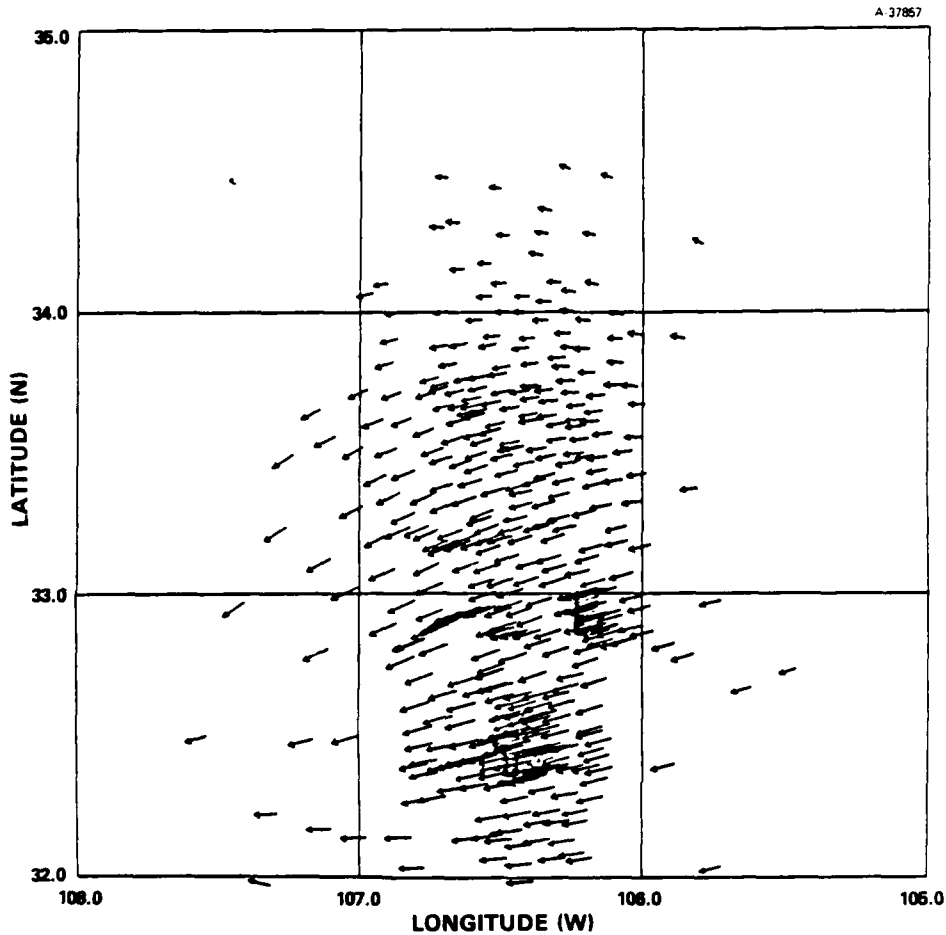


Figure C.5-3 Deflections of the Vertical from Geopotential Model

- The long-wavelength deflections of the vertical computed from Rapp 1981 (Ref. 38) geopotential model
- The long-wavelength components obtained from a low degree polynomial fit to the observed data.

The Rapp 1981 model produces deflections that are nearly the same as those computed from the Rapp 1978 (Ref. 37) coefficients; they agree in regional trend and magnitude. The low-order polynomial fit to the observations also shows the same

general trend. The older coefficients are selected for use in our present analysis in order to be consistent with work performed by the IAG Study Group.

The short-wavelength terrain-predicted deflections (Fig. C.5-2) and the long-wavelength deflections from the geopotential model (Fig. C.5-3), when summed, provide an approximation to the observed deflections of the vertical (Fig. C.5-1). Figure C.5-4 shows predicted deflections of the vertical which are obtained by summing the contributions of the terrain effects and the geopotential model. The summed predictions correlate well with the direction of the observed deflections,

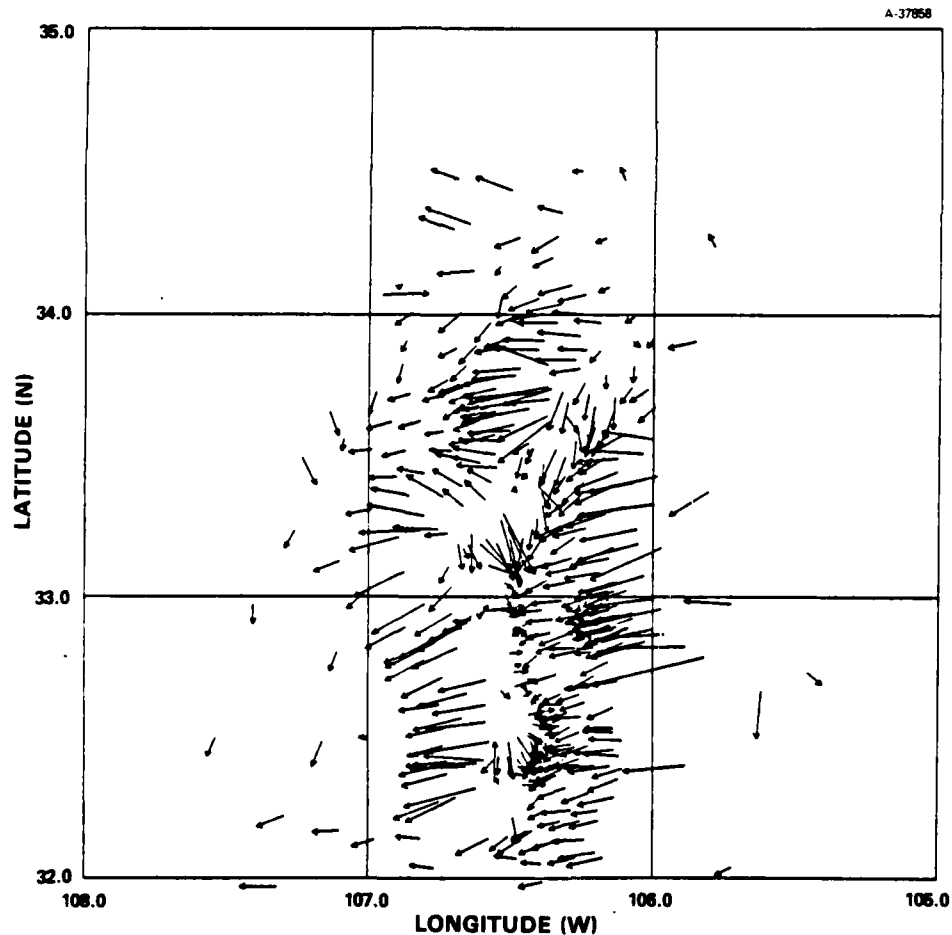


Figure C.5-4 Predicted (Geopotential Model + Terrain-Predicted) Deflections of the Vertical

but the magnitudes are generally smaller. Figure C.5-4 also agrees with "terrain reduced" deflections of the vertical produced by Tscherning and Forsberg (Ref. 20, Fig. 2, p. 89).

Figure C.5-5 shows residual deflections of the vertical derived by subtracting the predicted deflections (shown in Fig. C.5-4) from the observed deflections of the vertical (Fig. C.5-1). The residuals show systematic deflection differences from 4 to 6 arc sec in two north-south bands between 106 deg and 106.5 deg West. A possible source of these systematic deflections is an unmodeled variation in density, which could include, in part, effects of isostatic compensation.

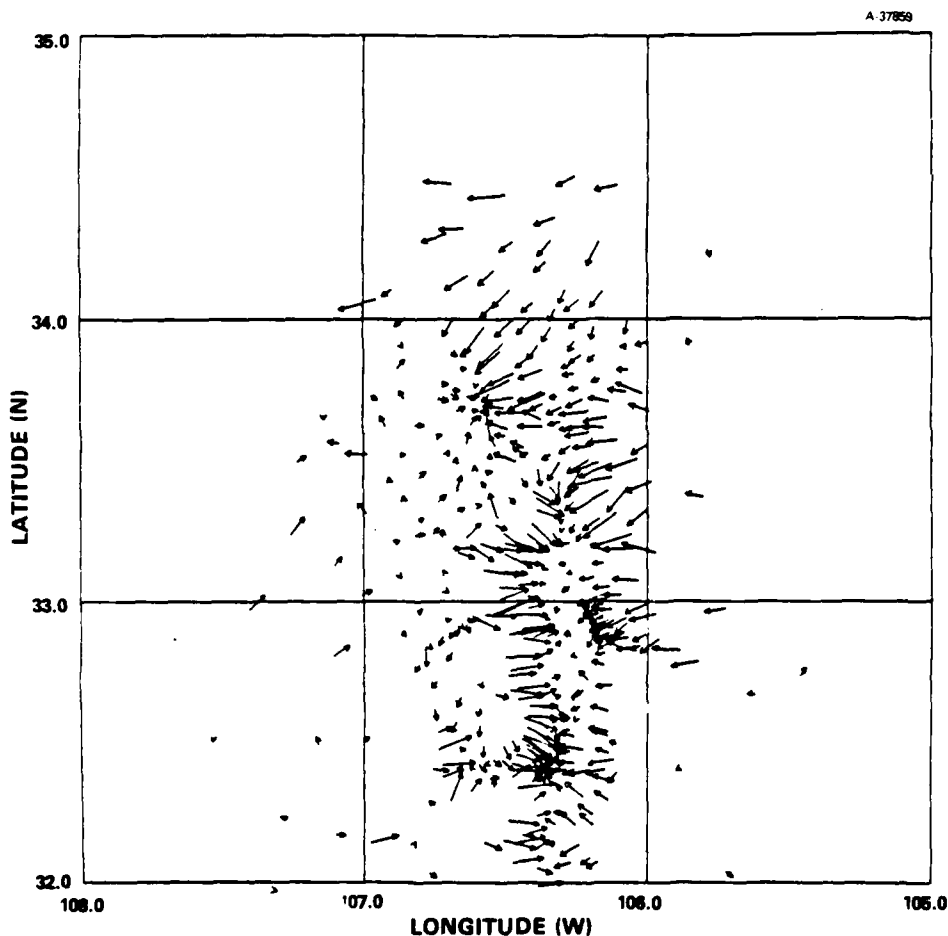


Figure C.5-5 Residual (Observed-Geopotential Model Plus Terrain-Predicted) Deflections of the Vertical

Fundamental statistics of the observed and predicted deflections are tabulated in Table C.5-1. They consist of the rms, mean, and standard deviation. Although they are not independent, the rms

$$\text{rms} = \sqrt{\frac{\sum_{i=1}^n x_i^2}{n}} \quad (\text{C.5-1})$$

and standard deviation (σ)

$$\sigma = \sqrt{\frac{\sum_{i=1}^n (x_i - \bar{x})^2}{n}} \quad (\text{C.5-2})$$

are useful in different ways, so both are included.

TABLE C.5-1
STATISTICS OF OBSERVED AND PREDICTED DEFLECTIONS
OF THE VERTICAL

DEFLECTIONS	FIG. NO.	RMS		MEAN		STANDARD DEVIATION	
		ξ	η	ξ	η	ξ	η
Observed	5.5-1	3.60	7.78	-2.44	-4.56	2.65	6.31
Terrain-Predicted	5.5-2	2.20	4.14	-0.78	0.12	2.06	4.14
Rapp '78 Coef.	5.5-3	1.26	4.40	-1.09	-4.33	0.62	0.77
Predicted (Geopotential Model & Terrain)	5.5-4	2.76	5.81	-1.87	-4.21	2.03	4.00
Residual (Observed - Rapp & Terrain)	5.5-5	1.70	3.15	-0.57	-0.35	1.60	3.13

The mean represents the very long wavelength portion of each set of deflections, while the standard deviation is associated with the short wavelength amplitude. The rms supplies a measure of typical magnitudes for the primary sets of deflections and an indication of goodness of fit in the case of deflection residuals.

The success in predicting the observed data is reflected in the statistical results. For instance, the mean of the deflection residuals is nearly zero because the predictions account for most of the observed deflections of the vertical. The small rms of the residual deflections indicates a high goodness of fit between observed and modeled deflections. Additional support for the success of the model is shown by the similarities between the statistical values of the observed and predicted deflections.

The statistical analysis also provides a rough indication of the frequency of the terrain-height and geopotential model components of the predicted deflections. The near-zero mean of the terrain-predicted deflections show that their contribution is primarily short wavelength. The low standard deviation indicates a long wavelength contribution.

The coefficient of correlation, (r), is computed via:

$$r = \frac{\sum_{i=1}^n (t_i - \bar{t}) (p_i - \bar{p})}{\left[\left\{ \sum_{i=1}^n (t_i - \bar{t})^2 \right\} \left\{ \sum_{i=1}^n (p_i - \bar{p})^2 \right\} \right]^{\frac{1}{2}}} \quad (C.5-3)$$

to quantify the quality of the linear fit between the observed and predicted deflections. For the east component, $r = 0.91$; for the north component, $r = 0.80$. These high positive values

clearly show how well the predicted deflections approximate the observed deflection values. Interestingly, most of the high correlation is due to the terrain-predicted values because the coefficient of correlation between the observed deflections and deflections predicted from terrain only is virtually identical to the coefficient values listed above.

A more detailed view of the correlation between observed and modeled deflections is provided by the scatter diagrams shown in Figs. C.5-6 and C.5-7. The fact that the least-squares regression line for the east vertical deflections has a slope greater than one displays the systematic under-estimation of the east component of the observed deflections by the modeled deflections, as shown in Fig. C.5-5. If isostatic compensation were added, the underestimation might become even more pronounced. Therefore, the result points to systematic lateral density variations.

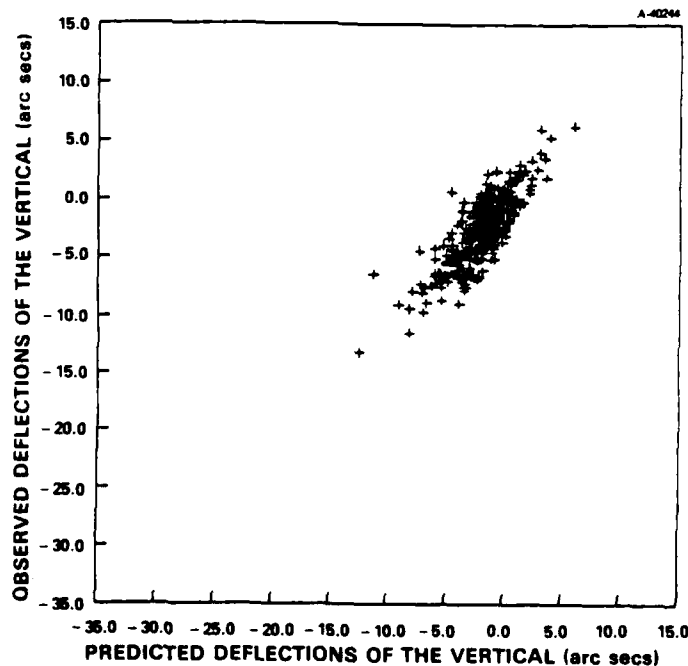


Figure C.5-6 Scatter Diagram of North Vertical Deflection Component

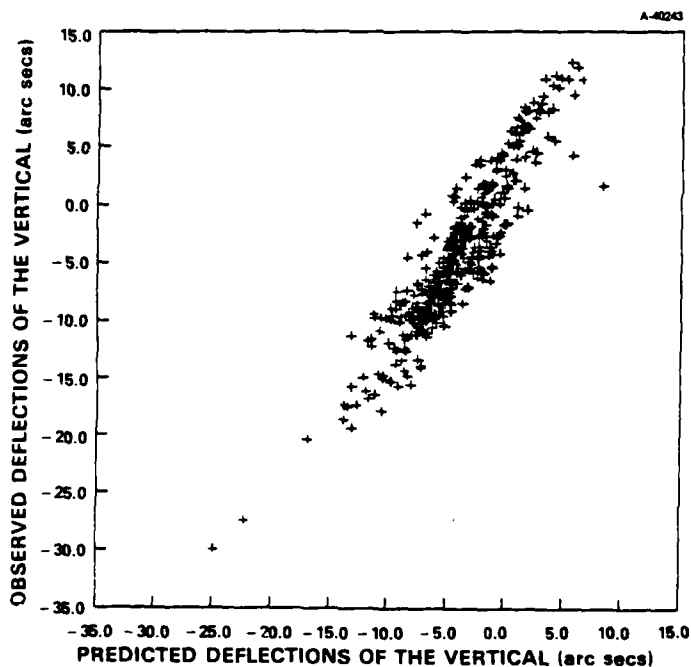


Figure C.5-7 Scatter Diagram of East Vertical Deflection Component

In conclusion, it may be stated that observed deflections of the vertical can be approximated reasonably well using deflections predicted from local terrain and a global geopotential model. Of course, with gravimetric deflection predictions, far more accuracy is attainable, as shown in the IAG Study Group reports (Refs. 20 and 21). The work reported here is complementary to the study group research in providing a more thorough examination of the terrain contribution and the novel examination of correlation and scatter diagrams.

REFERENCES

1. Heiskanen, W.A., and Moritz, H., Physical Geodesy, W.H. Freeman and Company, 1967.
2. Moritz, H., Advanced Physical Geodesy, Herbert Wichmann Verlag, 1980.
3. Molodenskii, M.S., Eremeev, V.F., and Yurkina, M.I., Methods for Study of the External Gravitational Field and Figure of the Earth, translated by the Israel Program for Scientific Translations, 1962 (University Microfilms International).
4. Pellinen, L.P., "Expedient Formulae for Computation of Earth's Gravitational Field Characteristics from Gravity Anomalies," Bulletin Géodésique, pp. 327-333, 1952.
5. Rice, D.A., "Deflections of the Vertical from Gravity Anomalies," Bulletin Géodésique, pp. 285-308, 1952.
6. Kearsley, A.H.W., The Computation of Deflection of the Vertical from Gravity Anomalies, Report UNISERV S-15, School of Surveying, University of New South Wales, 1976.
7. Van Gysen, H., Precise Deflections of the Vertical in the Canberra Area, University of New South Wales, 1980.
8. Rapp, R.H., and Rummel, R., Methods for the Computation of Detailed Geoids, and Their Accuracy, Report No. 233, Department of Geodetic Science, The Ohio State University, 1975.
9. Jekeli, C., "Modifying Stokes' Function to Reduce the Error of Geoid Undulation Computations," Journal of Geophysical Research, Volume 86, No. B8, pp. 6985-6990, August 1981.
10. Jekeli, C., "Optimizing Kernels of Truncated Integral Formulas in Physical Geodesy," Journal of the Geodetic Society of Japan, pp. 514-528, 1982.

REFERENCES (Continued)

11. Krarup, T.A., "A Contribution to the Mathematical Foundation of Physical Geodesy," Publ. 44, Danish Geodetic Institute, Copenhagen, 1969.
12. Moritz, H., "Least-Squares Estimation in Physical Geodesy," Report No. 130, Department of Geodetic Science, The Ohio State University, Columbus, 1970.
13. Moritz, H., "Advanced Least-Squares Methods," Report No. 175, Department of Geodetic Science, The Ohio State University, Columbus, 1972.
14. Gentry, D.E., and Nash, R.A., "A Statistical Algorithm for Computing Vertical Deflections Gravimetrically," Journal of Geophysical Research, Vol. 77, No. 26, pp. 4912-4919, September 1972.
15. Tscherning, C.C., "A Fortran IV Program for the Determination of the Anomalous Potential Using Stepwise Least-Squares Collocation," Report No. 212, Department of Geodetic Science, The Ohio State University, Columbus, 1974.
16. Tait, K.S., "A Fast Estimation Algorithm for Two-Dimensional Gravity Data (GEOFAST)," The Analytic Sciences Corporation, Report No. TR-868-1-1, November 1979.
17. Moritz, H., "Least-Squares Collocation," Reviews of Geophysics and Space Physics, Vol. 16, No. 3, pp. 421-430, August 1978.
18. Forsberg, R., and Tscherning, C.C., "The Use of Height Data in Gravity Field Approximation by Collocation," Journal of Geophysical Research, Vol. 86, No. B9, pp. 7843-7854, September 1981.
19. Forsberg, R., and Madsen, F., "Geoid Prediction in Northern Greenland Using Collocation and Digital Terrain Models," Ann. Geophys., Vol. 37, pp. 31-36, 1981.
20. Schwarz, K.P. (Ed.), "Techniques to Predict Gravity Anomalies and Deflections of the Vertical in Mountainous Areas," Report No. 30004, Division of Surveying Engineering, University of Calgary, Alberta, April 1983.

REFERENCES (Continued)

21. Kearsley, A.H.W., Sideris, M.G., Krynski, J., Forsberg, R., and Schwarz, K.P., "White Sands Revisited: A Comparison of Techniques to Predict Deflections of the Vertical," Report No. 30007, Division of Surveying Engineering, University of Calgary, Alberta, May 1985.
22. Dahlquist, G., and Björck, A., Numerical Methods, translated by Anderson, N., Prentice-Hall, Englewood Cliffs, NJ, 1974.
23. Tscherning, C.C., and Rapp, R.H., "Closed Covariance Expressions for Gravity Anomalies, Geoid Undulations, and Deflections of the Vertical Implied by Anomaly Degree Variance Models," Report No. 208, Department of Geodetic Science, The Ohio State University, Columbus, 1974.
24. Heller, W.G., and Jordan, S.K., "Attenuated White Noise Statistical Gravity Model," Journal of Geophysical Research, Vol. 84, No. B9, pp. 4680-4688, August 1979.
25. Reilly, W.I., "Mapping the Local Geometry of the Earth's Gravity Field," Report No. 143, Department of Scientific and Industrial Research, Geophysics Division, New Zealand, 1979.
26. Hein, G.W., and Landau, H., "Application of Local Collocation and Investigations on the Influence of the Topography on Geoid Heights, Deflections of the Vertical and Gravity Anomalies," in Schwarz, K.P. (Ed), "Techniques to Predict Gravity Anomalies and Deflections of the Vertical in Mountainous Areas," Report No. 30004, Division of Surveying Engineering, University of Calgary, Alberta, April 1983.
27. Nash, J.C., Compact Numerical Methods for Computers: Linear Algebra and Function Minimization, John Wiley and Sons, New York, 1979.
28. Kaiser, J.F., "Nonrecursive Digital Filter Design Using the I_0 -SINH Window Function," Proc. 1974 IEEE Int. Symp. on Circuits and Syst., pp. 20-23, April 1974.

REFERENCES (Continued)

29. Forsythe, G.E., and Moler, C.B., Computer Solution of Linear Algebraic Systems, Prentice-Hall, Englewood Cliffs, NJ, 1967.
30. Isaacson, E., and Keller, H.B., Analysis of Numerical Methods, John Wiley and Sons, New York, 1966.
31. Jordan, S.K., "Fourier Physical Geodesy," Report No. AFGL-TR-78-0056, Air Force Geophysics Laboratory, March 1978.
32. Bracewell, R.N., The Fourier Transform and Its Applications, McGraw-Hill, New York, 1978.
33. Sideris, M.G., "A Fast Fourier Transform Method for Computing Terrain Corrections," Manuscripta Geodaetica, Vol. 10, pp. 66-73, 1985.
34. Forsberg, R., "A Study of Terrain Reductions, Density Anomalies and Geophysical Inversion Methods in Gravity Field Modeling," Report No. 355, Department of Geodetic Science and Surveying, The Ohio State University, Columbus, 1984.
35. Comer, R.P., "Terrain Correction via FFT: A New Derivation (abstract)," EOS, Transactions, American Geophysical Union, Vol. 67, No. 16, p. 260, April 1986.
36. Lerch, F.J., Putney, B.H., Wagner, C.A., and Klosko, S.M., "Goddard Earth Models for Oceanographic Applications (GEM10B and 10C)," Marine Geodesy, Vol. 5, No. 2, pp. 145-187, 1981.
37. Rapp, R.H., "A Global 1°x1° Anomaly Field Combining Satellite Geos-3 Altimeter and Terrestrial Anomaly Data," Report No. 278, Department of Geodetic Science, The Ohio State University, Columbus, 1978.
38. Rapp, R.H., "The Earth's Gravity Field to Degree and Order 180 Using Seasat Altimeter Data, Terrestrial Gravity Data, and Other Data," Report No. 322, Department of Geodetic Science, The Ohio State University, Columbus, 1981.

REFERENCES (Continued)

39. White, J.V., "A Statistical Gravity Model for Northern Texas," The Analytic Sciences Corporation, Report No. AFGL-TR-85-0037, November 1984.
40. Pratt, W.K., "Generalized Wiener Filter Computation Techniques," IEEE Transaction on Computers, Vol. C-21, pp. 636-641, July 1972.
41. Thomas, S.W., and Heller, W.G., "Efficient Estimation Techniques for Integrated Gravity Data Processing," The Analytic Sciences Corporation, Report No. AFGL-TR-76-0232, September 1976.
42. Koch, S.E., DesJardins, M., and Kocin, P.J., "An Interactive Barnes Objective Map Analysis Scheme for Use with Satellite and Conventional Data," Journal of Climate and Applied Meteorology, Vol. 22, No. 9, pp. 1487-1503, September 1983.
43. Robertson, E.C., The Nature of the Solid Earth, International Series in the Earth and Planetary Sciences, McGraw-Hill, 1972.
44. White, J.V., "Stochastic State-Space Models from Empirical Data," Proceedings ICASSP 83, Vol. 1, IEEE International Conference Acoustics, Speech and Signal Processing, Paper No. 6.3, pp. 243-246, April 1983.
45. Nichols, M.K., Baumgartner, S.L., Goldstein, J.G., and Sailor, R.V., "Computation and Display of Global Gravity Disturbances at Altitude," AIAA Guidance And Control Conference, August 20, 1985.
46. "Geodetic Algorithm Research: Progress Report For The Quarter Ending 31 March 1985," The Analytic Sciences Corporation, SP-5186-1-1, April 3, 1985.
47. Rummel, R., and Rapp, R.H., "The Influence of the Atmosphere on Geoid and Potential Coefficient Determination from Gravity Data," Journal of Geophysical Research, Vol. 81, pp. 5639-5642, 1976.
48. Rapp, R.H., "Ellipsoidal Corrections for Geoid Undulation Computations Using Gravity Anomalies in a Cap," Journal of Geophysical Research, Vol. 86, pp. 10843-10843, 1981.

REFERENCES (Continued)

49. Heller, W.G., LeSchack, A.R., and Cushman, S.F., "Assessment of Means for Determining Deflection of the Vertical," The Analytic Sciences Corporation, Report No. ETL-0303, August 1982.

LIMED
8